

CONFIDENTIAL

Copy 336
RM L57I16

NACA RM L57I16



RESEARCH MEMORANDUM

THEORETICAL AND EXPERIMENTAL INVESTIGATION OF
ARBITRARY ASPECT RATIO, SUPERCAVITATING
HYDROFOILS OPERATING NEAR THE
FREE WATER SURFACE

By Virgil E. Johnson, Jr.

Langley Aeronautical Laboratory
Langley Field, Va.

CLASSIFIED DOCUMENT

This material contains information affecting the National Defense of the United States within the meaning of the espionage laws, Title 18, U.S.C., Secs. 793 and 794, the transmission or revelation of which in any manner to an unauthorized person is prohibited by law.

CLASSIFICATION CHANGED TO UNCLASSIFIED

AUTHORITY: NACA RESEARCH ABSTRACT NO. 127

EFFECTIVE DATE: MAY 16, 1958

WHL

**NATIONAL ADVISORY COMMITTEE
FOR AERONAUTICS**

WASHINGTON

December 12, 1957

CONFIDENTIAL

NATIONAL ADVISORY COMMITTEE FOR AERONAUTICS

RESEARCH MEMORANDUM

THEORETICAL AND EXPERIMENTAL INVESTIGATION OF
ARBITRARY ASPECT RATIO, SUPERCAVITATING
HYDROFOILS OPERATING NEAR THE
FREE WATER SURFACE

By Virgil E. Johnson, Jr.

SUMMARY

Theoretical expressions for the lift, drag, and center of pressure of supercavitating hydrofoils of arbitrary section, aspect ratio, and depth of submersion are developed for the zero-cavitation-number case.

In order to verify and supplement the theoretical investigation, an experimental investigation was made in Langley tank no. 2 of two aspect-ratio-1 hydrofoils, one with a flat and one with a cambered lower surface. Zero cavitation number was obtained in the tank by operating the hydrofoils near the water surface so that their upper surfaces were completely ventilated. Data were also obtained at cavitation numbers greater than zero for flows with vapor-filled cavities and with air artificially introduced to simulate the same flows at lower speeds. The tests covered a range of water speeds up to 80 feet per second, angles of attack up to 20° , and depths of submersion from 0- to 85-percent chord.

The theoretical force and moment coefficients agreed with the data obtained in the zero-cavitation-number tests within an accuracy of about 3 percent. The ventilated force and moment coefficients of both models were independent of speed. As predicted by the linear theory of Tulin and Burkart, the cambered hydrofoil lift-drag ratio was superior to that for the flat plate at the same lift coefficient. Similar to the influence of camber on a fully wetted airfoil, the influence of camber in ventilated flow was to effectively increase the angle of attack without appreciably changing the lift-curve slope. Comparison of the present results with the results of other investigations revealed that a sharp leading edge is necessary for good efficiency in supercavitating flow.

The nonzero-cavitation-number tests confirmed the finding of others that the lift of a hydrofoil operating in a finite cavity depends only on the cavitation number and is independent of whether the gas in the cavity is air or vapor.

INTRODUCTION

The desirability of using auxiliary lifting surfaces such as hydrofoils or hydroskis for reducing seaplane-hull loads and improving rough-water performance is well established. Although the higher aspect-ratio submerged hydrofoils with their accompanying high efficiencies could be the most desirable lifting surfaces to be used, only the low-aspect-ratio planing hydroski has so far been successfully applied as landing gear to modern high-speed aircraft. The reason for this is that the conventional hydrofoil presents problems not experienced by a hydroski.

As a hydrofoil nears the free water surface (during a take-off run) the low pressure side of the hydrofoil becomes ventilated from the atmosphere. This phenomenon results in a severe and usually abrupt loss in lift and reduction in the lift-drag ratio. For conventional airfoil sections, the loss in lift may exceed 75 percent. The speed at the inception of ventilation depends on the angle of attack and depth of submersion; but, except for very small angles of attack and relatively low take-off speeds, the speed at inception is usually well below the take-off speed of the aircraft.

Even if the ventilation problem is overcome by using small angles of attack and incorporating fences or other devices for suppressing ventilation, the onset of cavitation presents a second deterrent to the use of conventional hydrofoils at high speeds. The loss in lift accompanying cavitation of conventional airfoil sections is not abrupt, but the ultimate reduction in lift and lift-drag ratio is comparable to that of ventilated flow. Even thin-airfoil sections of small design-lift coefficient enter this cavitating regime of poor lift-drag ratios at speeds in excess of about 80 knots.

Since the take-off speed of modern supersonic aircraft is in the range of 150 to 200 knots, lifting surfaces with cavitating or ventilating characteristics superior to those of conventional airfoil sections are desirable. Fortunately, theoretical work by Tulin and Burkart (ref. 1) has shown that superior configurations do exist and they have selected a cambered configuration for operation in cavitating or ventilated flow which, in an inviscid fluid, has two-dimensional lift-drag ratios at its design angle of attack and zero cavitation number, about six times that of a flat plate. If such a cambered hydrofoil can be

induced to ventilate at very low speeds, while the aircraft hull still supports most of the load, a stable and efficient take-off run may be possible.

The present report is concerned with an experimental and theoretical investigation of one of the Tulin-Burkart cambered configurations and a comparison of its characteristics with those of a flat plate. The purpose of the investigation was (1) to find out if the superiority of the cambered configurations obtained from two-dimensional, infinite-depth theory would be maintained at finite depth and aspect ratio, and (2) to develop expressions for the prediction of the force and moment characteristics of a ventilated hydrofoil of arbitrary section profile which would include these three-dimensional effects.

SYMBOLS

A	aspect ratio
A_n, A_0	coefficients of sine-series expansion of vorticity distribution on equivalent airfoil section at infinite depth, that is,
	$\Omega(x) = 2V \left(A_0 \cot \frac{\theta}{2} + A_1 \sin \theta + A_2 \sin 2\theta \dots A_n \sin n\theta \right)$
	where
	$A_n = \frac{2}{\pi} \int_0^{\pi} \frac{d\bar{y}}{dx} \cos n\theta d\theta$
	$A_0 = -\frac{1}{\pi} \int_0^{\pi} \frac{d\bar{y}}{dx} d\theta + \alpha = \alpha + A_0'$
$A_{n,h}, A_{0,h}$	coefficients of sine-series expansion of vorticity distribution on hydrofoil section
a	distance from equivalent airfoil leading edge to center of pressure in chords
B_n, B_0	coefficients of cosine series defining location of image vortex in airfoil plane
b	parameter defining location of spray at infinity in t plane (see ref. 2)

C_D	total-drag coefficient, $\frac{D}{qS}$
$C_{D,1}$	profile-drag coefficient (total drag less crossflow and skin friction), $\frac{D_1}{qS}$
$C_{D,c}$	crossflow-drag coefficient (normal to the section), $\frac{D_c}{qS}$
C_f	skin-friction drag coefficient, $\frac{D_f}{qS}$
C_L	total-lift coefficient, $\frac{L}{qS}$
\bar{C}_L	total-lift coefficient of equivalent airfoil section, $\frac{\bar{L}}{\bar{q}\bar{S}}$
$C_{L,1}$	lift coefficient exclusive of crossflow, $\frac{L_1}{qS}$
$C_{L,c}$	crossflow lift coefficient, $\frac{L_c}{qS}$
C_m	pitching-moment coefficient (about the leading edge), $\frac{M}{qSc}$
\bar{C}_m	pitching-moment coefficient of equivalent airfoil section (about the leading edge), $\frac{\bar{M}}{\bar{q}\bar{S}\bar{c}}$
$\bar{C}_{m,3}$	third-moment coefficient of equivalent airfoil section (see ref. 1), $\frac{\bar{M}_3}{\bar{q}\bar{S}\bar{c}^4}$
C_N	resultant-force coefficient on arbitrary section, $\frac{F}{qS}$
$C_{N,f}$	resultant-force coefficient of flat plate, $\frac{F}{qS}$
C_n, C_0	coefficients of sine-series expansion of vorticity distribution on equivalent airfoil section at arbitrary depth
c	chord
D	total drag force
D_1	drag force excluding crossflow drag and skin friction

D_c	drag force due to crossflow (normal to section)
D_f	drag force due to skin friction
d	leading-edge depth of submersion
E	Jones' edge correction, ratio of semiperimeter to span (see ref. 14)
F	resultant force
g	acceleration due to gravity
L	total lift force
L_c	lift force due to crossflow
L_1	lift force exclusive of crossflow, $L - L_c$
l	distance from hydrofoil leading edge to stagnation point in chords
M	moment about leading edge
\bar{M}_3	third moment about leading edge, $2 \int_0^{\bar{c}} p(\bar{x}) \bar{x}^3 d\bar{x}$
$m = C_L/a$	
p	pressure, lb/sq ft
p_c	pressure within cavity, lb/sq ft
p_o	pressure at mean depth of hydrofoil, lb/sq ft
p_v	fluid vapor pressure, lb/sq ft
q	free-stream dynamic pressure, $\frac{1}{2}\rho V^2$
r	distance from image vortex to point on equivalent airfoil in chords
S	area, sq ft
s	span, ft
u	perturbation velocity in X-direction

V	speed of advance, fps
v	perturbation velocity in Y-direction
X, Y	coordinate axes
x	distance from leading edge along X-axis
$x_{c.p.}$	distance from leading edge to center of pressure
y_1	distance from the X-axis to hydrofoil lower surface
y_u	distance from the X-axis to hydrofoil upper surface
α	geometric angle of attack, radians unless otherwise specified
α_c	angle-of-attack increase due to camber, $(C_0' + C_1 - C_2/2)$ or at infinite depth $\alpha_{c,\infty} = (A_1 - A_2/2)$, radians unless otherwise specified
α_i	induced angle of attack, radians unless otherwise specified
α_o	angle between hydrofoil chord line and reference line, posi- tive when chord line is below reference line, radians unless otherwise specified
α'	angle of attack measured from hydrofoil chord line, $\alpha' = \alpha + \alpha_o$, radians unless otherwise specified
Γ	circulation, strength of single vortex
γ	central angle subtending chord of circular-arc hydrofoil
δ	spray thickness at infinite distance downstream
ϵ	deviation of resultant-force vector from normal to hydrofoil reference line
θ	parameter defining distance along airfoil chord, $\bar{x} = \frac{\bar{c}}{2}(1 - \cos \theta)$
ρ	mass density, $\frac{\text{lb-sec}^2}{\text{ft}^4}$
σ	cavitation number, $\frac{p_o - p_c}{q}$
σ_i	cavitation number at inception

τ correction factor for variation from elliptical plan form

ϕ angle between spray and horizontal

ψ angle between \bar{x} -axis and line joining image vortex with a point on equivalent airfoil

Ω vorticity

{ } indicates "function of" for example, $C_N\{\alpha\} = C_{N,f}\{\alpha + \alpha_C\}$

$Z = X + iY$

$$\beta = \tan^{-1} \frac{C_D}{C_L} = \alpha + \epsilon$$

Subscripts:

e effective

0 zero depth of submersion

t total

∞ infinite depth of submersion

c.p. center of pressure

Barred symbols refer to equivalent airfoil section and unbarred symbols refer to the supercavitating hydrofoil section.

DESCRIPTION OF SUPERCAVITATING FLOW

The parameter defining cavity flow is $\sigma = \frac{p_0 - p_c}{q}$ where p_0 is the pressure at the mean depth, p_c the pressure within the cavity, and q , the dynamic pressure. The magnitude of σ for the condition at which cavitation is incipient is defined by the particular value σ_i . If σ is reduced below σ_i , cavitation becomes more severe; that is, the cavitation zone extends over a larger area. When a hydrofoil operates at sufficiently low values of σ , the cavity formed may completely enclose the upper or suction surface and extend several chords downstream as shown in figure 1(a). Theoretically if the cavitation parameter is reduced to zero, the cavity formed will extend to infinity. The flow regime where the cavity length exceeds the chord is defined as supercavitating flow.

Supercavitating flow, may be obtained by either increasing velocity or cavity pressure or both. At a constant depth and water temperature, σ and therefore, the length of the cavity is dependent only on the velocity since $p_o - p_c$ is then $p_o - p_v$ and is constant. If part or all of the boundary layer of a configuration is separated, the eddying fluid in the separated region can be replaced by a continuous flow of lighter fluid such as air. (See refs. 3 and 4.) Regulation of the amount of air supplied will control the cavity pressure and thus the length of the cavity formed. If the quantity of air supplied is very large, the cavity pressure will approach the ambient pressure p_o and a very long cavity will result even at low-stream velocities.

The ventilation of surface piercing hydrofoils is therefore a supercavitating flow due to large quantities of air supplied from the atmosphere to separated flow on the suction surface of the hydrofoil. Súpcavitating flow as a result of ventilation also occurs when a nonsurface-piercing hydrofoil of moderate aspect ratio operates near the free surface (see fig. 1(b)). As pointed out in reference 5, air is entrained in the trailing vortices and drawn to the suction side of the hydrofoil causing a long trailing cavity to enclose completely the upper surface of the hydrofoil and extend far downstream. The ventilated type cavity described in reference 5 differs in shape from those formed in deeply submerged flow because of the proximity of the free water surface. It is similar to planing, with the spray forming the upper surface of the cavity. Since the cavity pressure is approximately the same as the ambient pressure (at small depths of submersion), the cavitation number for this type flow is nearly zero.

The experimental portion of the present investigation utilized both of the methods of obtaining low values of σ discussed in the foregoing paragraphs; that is, varying velocity and cavity pressure. However, the case of zero cavitation number was of particular interest since it represents the condition of minimum lift and also because a major portion of the existing cavity flow theory assumes this condition. Therefore, most of this report treats the ventilated type supercavitating flow.

ZERO-CAVITATION-NUMBER THEORY

TWO-DIMENSIONAL THEORY

Flat Plate

The characteristics of a two-dimensional inclined flat plate in an infinite fluid, operating at zero cavitation number, have been obtained

by Kirchoff and Rayleigh (ref. 6). The resultant force on the plate is given by the well-known equation

$$C_{N,f} = \frac{2\pi \sin \alpha}{4 + \pi \sin \alpha} \quad (1)$$

The distance from the leading edge to the center of pressure is

$$\left(\frac{x}{c}\right)_{c.p.} = \frac{1}{4} \left(2 - \frac{3 \cos \alpha}{4 + \pi \sin \alpha} \right) \quad (2)$$

Similar work was performed by Green (refs. 2 and 7) to include the effect of the free water surface (but neglecting gravity). The solution is necessarily obtained in terms of the spray thickness δ rather than the more useful depth of submersion and is given as two parametric equations in terms of the parameter b .

$$C_L = C_{N,f} \cos \alpha = \frac{2(b - \sqrt{b^2 - 1}) \sin \alpha \cos \alpha}{D} = m \alpha \quad (3a)$$

$$\frac{\delta}{c} = \frac{b - \cos \alpha}{D} \quad (3b)$$

where

$$D = \left(b - \sqrt{b^2 - 1} \right) \sin \alpha + \frac{1}{\pi} \left[2 \cos \alpha + (b \cos \alpha - 1) \log_e \frac{b - 1}{b + 1} \right]$$

This result is plotted as the variation of m with δ/c for various angles of attack in figure 2.

Since gravity is neglected in Green's solution, it is important to understand the effect of the absence of this force on the result obtained. If the Froude number based on chord V^2/gc is large, then near the plate, where the streamline radii of curvature are small, the inertia forces are indeed large compared to the force of gravity. Thus, under these conditions, equations (3) for the force on the plate should be applicable, for a given δ/c , in spite of the neglect of gravity in its derivation. However, the variable δ/c is not usually known. It is desired to know the force on the plate for a given depth of submersion; therefore, the relationship between the leading-edge depth of submersion and the spray thickness is needed. The effect of gravity becomes very important in determining this relationship. Because of the neglect of gravity in the analysis of Green, the plate is always located infinitely above the still water surface - a physical impossibility in a real fluid. Gravity cannot be neglected in determining the location of the free water surface. The reason for this is that several chords away from the plate the streamline

radii of curvature become very large and thus the inertia forces become of the same or lower order of magnitude than the force of gravity. When gravity is present the distance of the plate above the water surface at infinity is at least limited to the dynamic pressure head. The effect of finite aspect ratio is also to place the plate finitely near the free water surface as will be discussed in a subsequent section.

In summary, if the Froude number is large, the forces on an inclined flat plate near a free water surface can be obtained in terms of the spray thickness δ/c from equations (3). The relationship between the spray thickness and the actual leading-edge depth of submersion cannot be determined from Green's analysis, but the relationship is known to be influenced by the presence of gravity and the aspect ratio of the plate. The method by which the lines of constant depth (shown in fig. 2) were obtained is discussed in a subsequent section.

The angle ϕ that the spray makes with the direction of motion is also obtained from reference 2 as

$$\phi = \cos^{-1} \left(\frac{b \cos \alpha - 1}{b - \cos \alpha} \right) - \alpha \quad (4)$$

The variation of ϕ (eq. (4)) with δ/c (eq. (3b)) is shown in figure 3.

Cambered Sections

Cambered surfaces can theoretically be analyzed in two dimensions by the method of Levi-Civita (ref. 7). However, like many conformal mapping problems the method is very difficult to apply to a particular configuration and only a few specific solutions have been obtained. Among these is the work of Rosenhead (ref. 8) and Wu (ref. 9). Although the solution of Wu is applicable in principle to arbitrary sections, the solution was presented only for the circular arc. A particular advantage of Wu's solution is that it includes the effects of nonzero cavitation number.

The most useful treatment of cambered surfaces is the linearized theory of Tulin and Burkart (ref. 1) which is readily applicable to any surface configuration (with positive lower surface pressures) as long as the angle of attack and camber are small. The principal results of this linearized theory are summarized below.

The supercavitating hydrofoil problem in the Z -plane is transformed into an airfoil problem in the \bar{Z} -plane by the relationship $\bar{Z} = -\sqrt{Z}$. By

denoting properties of the equivalent airfoil with barred symbols and those of the hydrofoil with unbarred symbols, the following relationships are derived:

$$\frac{d\bar{y}}{d\bar{x}}(\bar{x}) = \frac{dy}{dx}(\bar{x}^2) \quad (5)$$

$$\bar{u}(\bar{x}) = u(\bar{x}^2) \quad (6)$$

$$C_L = \bar{C}_m = \frac{\pi}{2} \left(A_0 + A_1 - \frac{A_2}{2} \right) \quad (7)$$

$$C_D = \frac{1}{8\pi} (\bar{C}_L)^2 = \frac{\pi}{2} \left(A_0 + \frac{A_1}{2} \right)^2 \quad (8)$$

$$C_m = \bar{C}_m, 3 = \frac{\pi}{32} \left(5A_0 + 7A_1 - 7A_2 + 3A_3 - \frac{A_4}{2} \right) \quad (9)$$

The coefficients A_n are the thin-airfoil coefficients in the sine-series expansion of the airfoil-vorticity distribution

$$\Omega(\bar{x}) = 2V \left(A_0 \cot \frac{\theta}{2} + \sum_{n=1}^{\infty} A_n \sin n\theta \right) \quad (10)$$

where

$$\bar{x} = \frac{\bar{c}}{2}(1 - \cos \theta), \quad (0 \leq \theta \leq \pi)$$

and can be found for a given configuration from the following equations

$$A_0 = - \frac{1}{\pi} \int_0^{\pi} \frac{d\bar{y}}{d\bar{x}} d\theta + \alpha = \alpha + A_0' \quad (11a)$$

$$A_n = \frac{2}{\pi} \int_0^{\pi} \frac{d\bar{y}}{d\bar{x}} \cos n\theta d\theta \quad (11b)$$

By using equations (7) and (8), the condition that A_0 in equation (10) is zero, that $\Omega(\bar{x})$ does not contain harmonics greater than two, and that $\Omega(\bar{x})$ is everywhere positive over the chord (that is, positive lower surface pressures on the hydrofoil), Tulin and Burkart (ref. 1) obtained a low-drag family of hydrofoils. This particular family of hydrofoils is given by the equation

$$\frac{y}{c} = \frac{A_1}{2} \left[\frac{x}{c} + \frac{8}{3} \left(\frac{x}{c} \right)^{3/2} - 4 \left(\frac{x}{c} \right)^2 \right] \quad (12)$$

The lift-drag ratio of this foil at its design incidence (that is, $\alpha = 0$) is from equations (7) and (8)

$$\frac{L}{D} = \frac{25}{4} \left(\frac{\pi}{2C_L} \right) \quad (13)$$

This 6.25-fold improvement over the L/D of a flat plate is most encouraging and was the impetus for this investigation.

The restrictions imposed by the assumptions of the Tulin-Burkart theory prevents its use in the calculation of the characteristics of hydrofoils suitable for use as aircraft landing gear. Here, because of the high hydrofoil loads on necessarily thin hydrofoils the aspect ratio may be as low as 1 or 2. Also the hydrofoil must operate near the free water surface and in some instances at large angles of attack. Thus, the effects of these variables on the characteristics of supercavitating hydrofoils (particularly of cambered sections) is needed. Much of this information can be obtained by certain modifications to the existing two-dimensional theory discussed in preceding paragraphs.

MODIFICATIONS OF TWO-DIMENSIONAL THEORY

Nonlinear Equation for Lift at Infinite Depth

For any configuration the reference line of the section from which the angle of attack is measured can be chosen such that $A_0' = 0$. It is

convenient in this report to assume that $\alpha = 0$ refers to the reference line which makes $A_0' = 0$. With this assumption, equation (7) may be written as

$$C_L = \frac{\pi}{2} \left(\alpha + A_1 - \frac{A_2}{2} \right) = \frac{\pi}{2} (\alpha + \alpha_c) \quad (14)$$

where α_c is the effective increase in angle of attack due to camber $(A_1 - \frac{A_2}{2})$. Thus, the solution for cambered hydrofoils is merely the flat plate linearized solution $\frac{\pi}{2}\alpha$ with α replaced by $\alpha + \alpha_c$. This is exactly analogous to the influence of camber on airfoils in an infinite fluid where there is an effective increase in angle of attack due to the camber. By carrying this procedure further, and by applying it to the resultant force rather than the lift, the nonlinear solution of Rayleigh becomes applicable to arbitrary configurations simply by replacing α by $\alpha + \alpha_c$; that is,

$$C_N \cong \frac{2\pi \sin(\alpha + \alpha_c)}{4 + \pi \sin(\alpha + \alpha_c)} \quad (15)$$

The lift will then be

$$C_L \cong \frac{2\pi \sin(\alpha + \alpha_c)}{4 + \pi \sin(\alpha + \alpha_c)} \cos \beta \quad (16)$$

Here, $\beta = \alpha + \epsilon$, where ϵ denotes the deviation of the resultant-force vector from the normal to the hydrofoil reference line. For large values of α , ϵ is small compared with α and $\cos \beta \cong \cos \alpha$. When α is very small, about 0° , ϵ is a maximum and can be shown by use of equations (7) and (8) to be $\frac{A_1^2}{4(A_1 - \frac{A_2}{2})}$ if $A_0' = 0$ as assumed. For any

practical low-drag hydrofoil, this value will almost always be less than 3° for which the cosine is very nearly 1 or cosine $(\alpha + \epsilon) \cong \cos \alpha \cong 1$. Therefore, $\cos \beta$ in equation (16) may be replaced by $\cos \alpha$ with little loss in accuracy and great gain in simplicity. Equation (16) then becomes

$$C_L \cong \frac{2\pi \sin(\alpha + \alpha_c)}{4 + \pi \sin(\alpha + \alpha_c)} \cos \alpha \quad (17)$$

For a circular-arc hydrofoil of central angle γ , it is shown in appendix A that $\alpha_c = (9/16)\gamma$ and that the reference line must be chosen at an angle $\gamma/8$ to the chord line so that $A_0' = 0$. The result obtained by substituting this value into equation (17) is compared in figure 4 with the linear solution of Tulin and Burkart (eq. (7)) and the nonlinear solution of Wu (ref. 9) for two circular-arc profiles. The agreement of equation (17) with the more exact solution of Wu is good over the entire range of angle of attack from 0° to 90° . Similar agreement is expected for any configuration of small camber.

Nonlinear Equation For Lift at Finite Depth

The successful modification of the Rayleigh equation to include cambered configurations leads at once to a similar modification of the solution of Green. However, in this case the argument for replacing α by $(\alpha + \alpha_c)$ is very weak unless the section coefficients which determine α_c are known as a function of the depth of submersion.

An examination of the linearized expressions for the lift coefficient of arbitrary foils at infinite depth and at zero depth reveals that both the lift-curve slope and the increase in angle of attack due to camber do change with depth of submersion. At infinite depth the linearized expression for lift coefficient is given by equation (7). At zero depth the lift coefficient must be one half of the fully wetted value obtained from thin-airfoil theory as pointed out in reference 10; that is,

$$C_{L,0} = \pi \left(A_{0,h} + \frac{A_{1,h}}{2} \right) \quad (18)$$

where $A_{0,h}$ and $A_{1,h}$ are the thin-airfoil coefficients of the section in the hydrofoil plane and are given by the expressions

$$A_{0,h} = -\frac{1}{\pi} \int_0^{\pi} \frac{dy}{dx} d\theta \quad (19a)$$

$$A_{1,h} = \frac{2}{\pi} \int_0^{\pi} \frac{dy}{dx} \cos \theta d\theta \quad (19b)$$

For the Tulin-Burkart section at zero angle of attack these values may be determined as

$$A_{0,h} = 0.227A_1 \quad (20a)$$

$$A_{1,h} = 1.151A_1 \quad (20b)$$

Thus, from equations (7) and (18) it is seen that, for a flat plate at small angles, the lift coefficient goes from $\frac{\pi}{2}\alpha$ at infinite depth to $\pi\alpha$ at zero depth (as given by Green) whereas, for the Tulin-Burkart section at zero angle of attack these values are $\frac{\pi}{2}(1.25A_1)$ at infinite depth and $\pi(0.802A_1)$ at zero depth. Although the flat-plate lift coefficient doubles in going from infinite to zero depth, the ratio is only 1.28 for the cambered section. The important point to note is that the value of α_c for the Tulin-Burkart section changes from $1.25A_1$ to $0.802A_1$.

It is now desirable to determine α_c for finite depths of submersion. This can be accomplished by modifying the linearized theory of reference 1 to include the effects of the free water surface.

The effect of the free water surface may be obtained by finding the transformation which will map the free water surface, the hydrofoil, and the cavity into the \bar{X} -axis of the \bar{Z} -plane. The required transformation is of the form $Z = \bar{Z} + K_1 \log_e \bar{Z} + K_2$. By using this transformation it is possible, in principle, to determine the forces on the hydrofoil by following the procedure used in reference 1. However, the solution by this method became very cumbersome and was abandoned when an approximate method was discovered. The approximate method continues with the transformation $\bar{Z} = -\sqrt{Z}$ used in reference 1.

In figure 5 it may be seen that $\bar{Z} = -\sqrt{Z}$ transforms the free water surface in the hydrofoil plane, where $u = 0$ (see fig. 5(a)), into a hyperbola in the third quadrant of the airfoil plane (fig. 5(b)). The boundary condition that must be satisfied on this hyperbola is that the perturbation velocity \bar{u} be zero because in complex velocity problems of the type considered here, it is the lines of constant velocity which are being transformed and not lines of constant velocity potential or stream function.

For the particular case of zero depth the hydrofoil problem is transformed by $\bar{Z} = -\sqrt{Z}$ into the fourth quadrant of the airfoil plane. Thus, it may be seen in figure 5(b) that the free water surface adds the condition that $\bar{u} = 0$ along the negative \bar{Y} -axis. This additional boundary condition can be satisfied (along with the other infinite-depth boundary conditions) by locating an image of the airfoil-vorticity distribution along the negative \bar{X} -axis. The direction of this vorticity must be

opposite to that of the airfoil in order to make $\bar{u} = 0$ at all points along the negative \bar{Y} -axis. A simpler and often used approximation is to replace the distributed image vorticity by a single vortex, equal in strength to the airfoil circulation, at a location equal to the distance from the leading edge to the airfoil center of pressure as shown in figure 5(b).

For finite depth of submersion, the condition that $\bar{u} = 0$ must be satisfied at all points on the hyperbola and on the negative \bar{X} -axis. It is not possible to satisfy these conditions with a single vortex as was done for the case of zero depth. However, the influence on the airfoil of the infinite array of vortices needed to satisfy the boundary conditions shown in figure 6 may be approximated by a single vortex of strength Γ in the location shown. The adequacy of the approximation can be determined by calculating the effect of this image vortex on the lift of a flat plate as the depth of submersion is varied and then, comparing the result with the exact solution of Green. This depth effect may be determined by concentrating the airfoil circulation at its center of pressure and the image circulation at a point $\frac{\bar{c}}{4} + \bar{c}\sqrt{\frac{d}{c}}$ forward of the leading edge and $\frac{\bar{c}}{2}\sqrt{\frac{d}{c}}$ below the leading edge (see fig. 6) and computing the total downwash on the flat plate at its $\frac{3\bar{c}}{4}$ point (see ref. 11). The method assumes that the center of pressure of the airfoil remains constant at $\bar{c}/4$ as the depth changes. The resulting downwash angle α at the $\frac{3\bar{c}}{4}$ point is calculated to be

$$\alpha = \frac{\Gamma}{\pi \bar{c} V} \left[1 - \frac{1}{2} \left(\frac{1 + \sqrt{d/c}}{1 + 2\sqrt{d/c} + (5/4)(d/c)} \right) \right] \quad (21)$$

Since $\Gamma_\infty = \pi \bar{c} \alpha V$, the ratio of hydrofoil lift at finite depth C_L to the lift at infinite depth is

$$\frac{C_L}{C_{L,\infty}} = \frac{\bar{C}_m}{\bar{C}_{m,\infty}} = \frac{\frac{1}{4} \bar{C}_L}{\frac{1}{4} \bar{C}_{L,\infty}} = \frac{\bar{C}_L}{\bar{C}_{L,\infty}} = \frac{\Gamma}{\Gamma_\infty} \quad (22)$$

therefore

$$\frac{C_L}{C_{L,\infty}} = \frac{\Gamma}{\Gamma_\infty} = \frac{1}{1 - \frac{1}{2} \left(\frac{1 + \sqrt{d/c}}{1 + 2\sqrt{d/c} + (5/4)(d/c)} \right)} \quad (23)$$

Equation (23) is compared in figure 7 with the exact solution of Green (see fig. 2, $\alpha = 0$), and the agreement is excellent.

The adequacy of the method used in determining the influence of free water surface proximity on the lift of a flat plate justifies its use on cambered foils. However, for cambered foils the problem is more difficult because a control point such as $\frac{3\bar{c}}{4}$ for a flat plate is not sufficient to determine the section coefficients defining the vorticity distribution. This final vorticity distribution $\Omega(\bar{x})$ resulting from the camber and the image vortex must be determined, particularly if a knowledge of the pressure distribution and thus the drag and center of pressure is desired.

In figure 8, it may be assumed that the final vorticity distribution on the equivalent airfoil is given by the equation

$$\Omega(\bar{x}) = 2V \left(C_0 \cot \frac{\theta}{2} + \sum_{n=1}^{\infty} C_n \sin n\theta \right) \quad (24)$$

Then the induced velocity at \bar{x}' due to $\Omega(\bar{x})$ is, from thin-airfoil theory (see ref. 12),

$$\bar{v} = V \left(-C_0 + \sum_{n=1}^{\infty} C_n \cos n\theta \right) \quad (25)$$

The resulting total circulation due to the vorticity given by equation (24) is, from thin-airfoil theory,

$$\Gamma = \pi \bar{c} V \left(C_0 + \frac{C_1}{2} \right) \quad (26)$$

Since the image vortex has a strength equal and opposite to Γ , the velocity induced by Γ_i at a point \bar{x}' on the airfoil is

$$\bar{v}_i = \frac{\Gamma}{2\pi r \bar{c}} \cos \psi \quad (27)$$

where

$$r = \sqrt{\left(a + \sqrt{\frac{d}{c}} + \frac{\bar{x}'}{c}\right)^2 + \frac{1}{4}\left(\frac{d}{c}\right)}$$

$$\cos \psi = \frac{a + \sqrt{\frac{d}{c}} + \frac{\bar{x}'}{c}}{r}$$

or

$$\frac{\cos \psi}{r} = \frac{a + \sqrt{\frac{d}{c}} + \frac{\bar{x}'}{c}}{\left(a + \sqrt{\frac{d}{c}} + \frac{\bar{x}'}{c}\right)^2 + \frac{1}{4}\frac{d}{c}} \quad (28)$$

where

$$a = \frac{\bar{C}_m}{\bar{C}_L}$$

or

$$a = \frac{1}{4} \frac{c_0 + c_1 - \frac{c_2}{2}}{c_0 + \frac{c_1}{2}} \quad (29)$$

Replacing \bar{x}' by $\frac{\bar{c}}{2}(1 - \cos \theta)$, equation (28) can be expanded in a Fourier series as

$$\frac{\cos \psi}{r} = f(\theta) = B_0 + \sum_{n=1}^{\infty} B_n \cos n\theta \quad (30)$$

where

$$B_0 = \frac{1}{\pi} \int_0^\pi f(\theta) d\theta$$

and

$$B_n = \frac{2}{\pi} \int_0^{\pi} f(\theta) \cos n\theta \, d\theta$$

By substituting equations (26) and (30) into equation (27) gives

$$\bar{v}_1 = \frac{v(c_0 + \frac{c_1}{2})}{2} \left(B_0 + \sum_{n=1}^{\infty} B_n \cos n\theta \right) \quad (31)$$

The equivalent airfoil slope $\frac{dy}{dx}$ when expanded in a cosine series is

$$\frac{dy}{dx} = -A_0 + \sum_{n=1}^{\infty} A_n \cos n\theta \quad (32)$$

Equating the resulting streamline slope to the equivalent airfoil slope gives

$$\frac{\bar{v}_t}{V} = \frac{\bar{v} + \bar{v}_1}{V} = \frac{dy}{dx} \quad (33)$$

The substitution of equations (25), (31), and (32) into equation (33) gives

$$-C_0 + \sum_{n=1}^{\infty} C_n \cos n\theta + \left(\frac{c_0 + \frac{c_1}{2}}{2} \right) \left(B_0 + \sum_{n=1}^{\infty} B_n \cos n\theta \right) = -A_0 + \sum_{n=1}^{\infty} A_n \cos n\theta \quad (34)$$

By equating coefficients of like terms, the C coefficients are determined as

$$C_0 = \frac{A_0(4 + B_1) + A_1 B_0}{4 + B_1 - 2B_0} \quad (35a)$$

$$C_1 = \frac{2A_1(2 - B_0) - 2A_0B_1}{4 + B_1 - 2B_0} \quad (35b)$$

$$C_n = A_n - \frac{(2A_0 + A_1)B_n}{4 + B_1 - 2B_0} \quad (35c)$$

If $A_0 = \alpha$ and $A_n = 0$ where $n \geq 1$, the effect of depth of submersion on the lift coefficient of a flat plate can be computed from the coefficients obtained from equations (35). The values of $\frac{C_L}{C_{L,\infty}}$ computed by this method have been found to be in excellent agreement with the solution of Green for $\alpha = 0$.

For the particular condition of $A_0 = 0$ (the case of hydrofoils such as the Tulin-Burkart section at zero angle of attack) equations (35) become

$$C_0 = \frac{B_0A_1}{4 + B_1 - 2B_0} \quad (36a)$$

$$C_1 = \frac{2A_1(2 - B_0)}{4 + B_1 - 2B_0} \quad (36b)$$

$$C_n = A_n - \frac{B_nA_1}{4 + B_1 - 2B_0} \quad (36c)$$

The coefficients B_0 and B_n as obtained from equation (30) are plotted in figure 9 against the distance to the center of pressure a for several depths of submersion. For the special condition of zero depth the B coefficients for the Tulin-Burkart section are found to be 1.296, 0.772, and 0.22 for B_0 , B_1 , and B_2 , respectively. In making this computation, the final center-of-pressure location a is used; therefore, a is first given an assumed value, the B and C coefficients determined, then from the resulting C coefficients, a is calculated from equation (29) and the procedure repeated if necessary. For the Tulin-Burkart section a is found to be 0.42 for $d/c = 0$. By using the final B coefficients the C coefficients are determined from equations (36) as $0.595A_1$, $0.646A_1$, and $-0.61A_1$ for C_0 , C_1 , and C_2 , respectively.

From equation (7) the ratio of the Tulin-Burkart section lift at zero depth to the lift at infinite depth is

$$\frac{C_{L,0}}{C_{L,\infty}} = \frac{(0.595 + 0.646 + 0.305)A_1}{5A_1/4} = 1.24 \quad (37)$$

The value 1.24 compares favorably with the more exact value of 1.28 given in the paragraph following equations (20). The results of calculating $\frac{C_L}{C_{L,\infty}}$ for finite depths of submersion for the Tulin-Burkart section are plotted in figure 10. Similar calculations have been made for a circular arc, and the configurations given in reference 13. The results of these calculations are also shown in figure 10.

The true linearized lift-curve slope m for finite depths of submersion in the equation $C_L = m(\alpha + \alpha_c)$ is that shown in figure 2 for $\alpha = 0$. Therefore, the effective angle of attack due to camber α_c is obtained from the following relationship:

$$\frac{\frac{m(\alpha=0)\alpha_c}{\frac{\pi}{2}\alpha_{c,\infty}}}{\frac{C_L}{C_{L,\infty}}} = \frac{C_L}{C_{L,\infty}}$$

Therefore

$$\frac{\alpha_c}{\alpha_{c,\infty}} = \frac{\pi}{2m(\alpha=0)} \frac{C_L}{C_{L,\infty}} \quad (38)$$

Values of $\frac{\alpha_c}{\alpha_{c,\infty}}$ are plotted against d/c in figure 11 for the Tulin-Burkart, the circular arc, and the sections given in reference 13.

Equation (38) is obviously limited by the linearizing assumptions made in its derivation. An important limitation is due to the assumption that the free surface is always horizontal and thus $\delta/c = d/c$. At small depth-chord ratios and particularly for large magnitudes of camber the free water surface is not horizontal and $\delta/c \neq d/c$. Thus, for small values of d/c and large magnitudes of camber the values of $\alpha_c/\alpha_{c,\infty}$ given in figure 11 are probably too low.

With a knowledge of the angle of attack due to camber α_c at finite depths of submersion, Green's solution is now modified to include camber

by treating the effective angle of attack as $(\alpha + \alpha_c)$, where α_c is obtained from figure 11. This is exactly the method used in modifying the Rayleigh equation to obtain the nonlinear approximation for the lift coefficient at infinite depth. With this assumption, the resultant-force coefficient for a cambered hydrofoil at any positive depth of submersion is obtained in terms of the spray thickness δ/c from equations (3) as

$$C_N\{\alpha\} \approx C_{N,f}\{\alpha + \alpha_c\} \quad (39)$$

Equation (39) states that the resultant force on a cambered section is approximated by replacing α in Green's solution for a flat plate by the effective angle of attack $(\alpha + \alpha_c)$. It will be shown that the resultant force will deviate only slightly from the normal (as previously pointed out for the condition of infinite depth) and therefore

$$C_L\{\alpha\} \approx C_{N,f}\{\alpha + \alpha_c\} \cos \alpha \quad (40)$$

Actually, by itself, equation (40) is of little practical value because $C_{N,f}$ is given in equations (3) in terms of the usually unknown parameter δ/c instead of the more useful d/c . Thus, it is necessary to determine the relationship between δ/c and d/c or at least an empirical substitute.

Relation Between Depth of Submersion and Spray Thickness

Certain relationships between the leading-edge depth of submersion and the spray thickness of a flat plate can be stated and are given as follows:

(1) The trivial but useful case for $\alpha = 0$ where $d/c \equiv \delta/c$

(2) The case of $\alpha = 90^\circ$, $\delta/c = \infty$, where the stagnation streamline is parallel to the direction of motion and in order to satisfy the continuity equation $\delta/c = d/c + 0.5$ (see fig. 12(a))

(3) The case of $\alpha = 90^\circ$, $\delta/c = 0$ where again the stagnation line (this time the free water surface) is parallel to the direction of motion and $\delta/c = d/c + 1$ (see fig. 12(b))

Cases (2) and (3) suggest that the stagnation line for $\alpha = 90^\circ$ is also parallel to the direction of motion for finite δ/c (as shown by the solid line in fig. 12(c)). However, this is not consistent with the

results of Green's analysis where it can be shown from momentum considerations that the streamline is curved as shown by the broken line in figure 12(c). However, when the effects of gravity and even slight deviations from infinite aspect ratio are considered, the true location of the stagnation line must lie between these two lines. The tendency of gravity to cause this change has been discussed already. Possibly more important than gravity is the influence of finite aspect ratio.

If the supercavitating hydrofoil is replaced by a system of horseshoe vortices, it can be shown that (for finite angles of attack and infinite aspect ratio) the stagnation line infinitely forward of the hydrofoil is also infinitely below the stagnation point - as obtained by Green. However, for an aspect ratio of as much as 100, the stagnation line approaches a finite asymptote about 0.2 chord below the stagnation point when the lift coefficient is about 0.5. At a lift coefficient of 0.5, the asymptote becomes about 0.1 chord for moderate aspect ratios. This was observed in the experiments described in a subsequent section where it was noted for the angle-of-attack range investigated that the free water surface was practically undisturbed only slightly forward of the hydrofoil leading edge. Therefore for an angle of attack of 90° where the total circulation is zero, it is not unreasonable to expect the solid stagnation line in figure 12(c) to be more nearly correct than the dashed one when both finite aspect ratio and gravity are present. It should be noted that although the stagnation line may deviate from the theory as given by Green, that the pressure distribution and force on the plate are assumed to remain unaltered from the expressions given in equations (3). Therefore, if at 90° the stagnation line is assumed parallel to the direction of motion, it follows that for $\alpha = 90^\circ$

$$\delta/c = d/c + l/c \quad (41)$$

where l/c is the dimensionless distance from the leading edge to the stagnation line (see fig. 12(c)). This distance can be obtained from Green's work and is, for $\alpha = 90^\circ$

$$l/c = \frac{1 + \frac{\pi b}{2} + \log_e\left(\frac{b}{b-1}\right) - \sqrt{b^2 - 1}\left(\frac{\pi}{2} \sin^{-1} \frac{1}{b}\right)}{\pi\left(b - \sqrt{b^2 - 1}\right) + \log_e\left(\frac{b+1}{b-1}\right)} \quad (42)$$

where b has been previously defined in equations (3).

Case (1) and equations (41) and (42) give the end points (at $\alpha = 0^\circ$ and 90°) of the lines of constant d/c which are superimposed on figure 2. The trends of these curves at intermediate angles of attack were obtained from experiment and will be discussed in a subsequent section.

The preceding discussion in this report has been concerned with the effects of gravity and finite aspect ratio on the relationship between the spray thickness and the leading-edge depth of submersion. It is also of interest to examine at least qualitatively the effects of gravity and finite aspect ratio on the spray angle given by equation (4) and plotted in figure 3. In Green's analysis, it is shown that at $\alpha = 90^\circ$ the total force on the entire plate is $F = \rho\delta V^2(1 - \cos \phi)$; that is, the force is exactly equal to the change in momentum due only to the flow in the spray. This means that the stagnation line must be curved as pointed out in the preceding discussion. The straight stagnation line (which leads to equation (41)) implies that the change in momentum in the spray flow results only in the force on that portion of the plate above the stagnation point. Since the change in momentum of the spray flow now represents only a portion of the total force on the plate, and since δ/c is considered to be the same for both stagnation-line curvatures, the angle ϕ must decrease from the value given by Green in figure 3. That is, the angle ϕ will change so that only the force on the plate above the stagnation line is given by the expression $F = \rho\delta V^2(1 - \cos \phi)$.

THREE DIMENSIONAL THEORY AT FINITE DEPTH

Lift

The flow about a supercavitating hydrofoil may be constructed by a suitable combination of sources and vortices. The vortices contribute unsymmetrical velocity components and lift, the sources contribute symmetrical components which provide thickness for the cavity but no lift. For a finite span the vortices can not end at the tips of the foil and a system of horseshoe vortices must be combined with the sources to describe the flow. If it is assumed that the influence of finite span on the two dimensional lift coefficient is due to the effects of the trailing vorticity then the resulting effect of aspect ratio is exactly the same as for a fully wetted airfoil. Jones (ref. 14) gives the lift of a fully wetted elliptical flat plate as

$$\bar{C}_L = \frac{1}{E} 2\pi(\alpha - \alpha_1) \quad (43)$$

where E is the ratio of semiperimeter to the span and α_1 is the induced angle of attack caused by the trailing vorticity. Thus the effect of aspect ratio is to decrease the two dimensional lift curve slope by a

factor $1/E$ and to decrease the effective angle of attack by an increment α_1 . Therefore for the finite aspect ratio supercavitating hydrofoil at infinite depth, equation (14) is modified to give

$$C_{L,1} = \frac{1}{E} \frac{\pi}{2} (\alpha + \alpha_c - \alpha_1) \quad (44)$$

or more generally for finite depth, equation (40) becomes

$$C_{L,1} \approx \frac{1}{E} C_{Nf} (\alpha + \alpha_c - \alpha_1) \cos \alpha \quad (45)$$

where for rectangular plan form of aspect ratio A , $E = \frac{A+1}{A}$ and

$$\alpha_1 = \frac{C_{L,1}}{\pi A} (1 + \tau) \quad (46)$$

where τ is a correction for plan form (see ref. 12).

Another effect due to finite aspect ratio is the concept of additional lift due to crossflow (see refs. 15 and 16). This crossflow lift is assumed due to the drag on the hydrofoil contributed by the component of free-stream velocity normal to the hydrofoil. In the present case of zero cavitation number, the crossflow drag coefficient is the Rayleigh value, 0.88. Since this lift is caused only by the spanwise flow (flow around the ends of the plate) it is also modified to account for the aspect ratio by the Jones' edge correction, $1/E$. Since only the spanwise flow is considered, E is now the ratio of semiperimeter to chord. Because the flow being considered is normal to the plate, the induced angle for this flow is zero. Thus for a flat plate, the crossflow lift $C_{L,c}$ is

$$C_{L,c} = \frac{1}{A+1} 0.88 \sin^2 \alpha \cos \alpha \quad (47)$$

No experimental or theoretical information on the crossflow lift of cambered surfaces is available in the literature. In order to approximate this component the following assumptions are made:

- (1) The crossflow force acts normal to the hydrofoil chord line.
- (2) The effective direction of the free stream on the plate is altered by the increase in angle of attack due to camber α_c .

Thus, the crossflow lift on cambered sections is assumed to be

$$C_{L,c} \cong \frac{1}{A+1} 0.88 \sin^2(\alpha' + \alpha_c) \cos \alpha' \quad (48)$$

where $\alpha' = \alpha + \alpha_o$, and α_o is the inclination of the chord line to the reference line of the section (positive if the chord line is below the reference line) and α_c is obtained from figure 11 for the depth of interest.

The total lift on a finite aspect ratio hydrofoil operating near the free water surface is therefore obtained by adding equation (48) to equation (45) to give

$$C_L[\alpha] \cong \frac{A}{A+1} C_{n,f} \left\{ \alpha + \alpha_c - \alpha_i \right\} \cos \alpha + \frac{1}{A+1} 0.88 \sin^2(\alpha' + \alpha_c) \cos \alpha' \quad (49)$$

In view of the very approximate nature of equation (48) it is desirable to examine the effect of this crossflow term on the total-lift coefficient. For the Tulin-Burkart, aspect-ratio-1 section ($A_1 = 0.2$) used in this investigation, at $d/c = 0.071$ the ratio of the calculated crossflow lift, $C_{L,c}$ to the calculated total lift was 0.157 at $\alpha = 4^\circ$ and 0.283 at $\alpha = 20^\circ$. For the five-term section of reference 13, where A_1 is 0.075, the aspect ratio is 3, and d/c is 0.071, the ratio has been calculated as 0.014 at $\alpha = 4^\circ$ and 0.072 at $\alpha = 20^\circ$. Thus any inaccuracies in the crossflow lift as computed by equation (48) will appreciably affect the total-lift coefficient at large angles, small aspect ratios, and large cambers. On the other hand at higher aspect ratios and small cambers, errors in the crossflow component do not greatly influence the total lift.

Equation (49) may be written in terms of the slope m (given in fig. 2) as

$$C_L = \frac{A}{A+1} m (\alpha + \alpha_c - \alpha_i) \frac{\cos \alpha}{\cos(\alpha + \alpha_c - \alpha_i)} + \frac{1}{A+1} 0.88 \sin^2(\alpha' + \alpha_c) \cos \alpha' \quad (50)$$

where α_c is obtained from figure 11 for the depth-chord ratio of interest and α_i is obtained from equation (46). In equation (46), $C_{L,1}$ is the first term in equation (50). Equation (50) is solved by iteration and the convergence is quite rapid. A sample calculation of the lift coefficient of a cambered hydrofoil is given in appendix B.

Drag

The drag coefficient of a supercavitating hydrofoil of finite aspect ratio operating at zero cavitation number and finite depth of submersion is

$$C_D = C_{L,1} \tan(\alpha + \epsilon) + C_{L,c} \tan \alpha' + C_f \quad (51)$$

where $C_{L,1}$ is the first term in equation (50) and ϵ is the deviation of the resultant-force vector from the normal. For a flat plate $\epsilon = 0$, $\alpha' = \alpha$, and thus $C_D = C_L \tan \alpha + C_f$. For cambered surfaces similar to the circular-arc or Tulin-Burkart section, ϵ becomes very small at large angles of attack and may be neglected; however, at small angles of attack, the effect of ϵ on the drag coefficient cannot be neglected. An approximation to the value of ϵ can be made by determining its value from the two-dimensional linearized solution and then modifying the result for the case of finite angles of attack and aspect ratio.

The linearized drag coefficient as given in reference 1 is

$$C_D = - \int_0^{\sqrt{c}} \frac{4\bar{x}\bar{v}\bar{u}}{cV^2} d\bar{x} \quad (52)$$

replacing \bar{x} by $\frac{\sqrt{c}}{2}(1 - \cos \theta)$ and $d\bar{x}$ by $\frac{\sqrt{c}}{2} \sin \theta d\theta$ equation (52) becomes

$$C_D = - \int_0^{\pi} \frac{(1 - \cos \theta) \sin \theta \bar{u} \bar{v}}{V^2} d\theta \quad (53)$$

Now \bar{u} may be written in terms of the vorticity on the equivalent airfoil operating at finite depth as

$$\bar{u} = \frac{\Omega}{2} = V \left[C_0 \left(\frac{1 + \cos \theta}{\sin \theta} \right) + \sum_{n=1}^{\infty} C_n \sin n\theta \right] \quad (54)$$

and

$$\bar{v} = V \left(-A_0 + \sum_{n=1}^{\infty} A_n \cos n\theta \right) \quad (55)$$

Therefore

$$C_D = - \int_0^\pi (1 - \cos \theta) \sin \theta \left[C_0 \left(\frac{1 + \cos \theta}{\sin \theta} \right) + \sum C_n \sin n\theta \right] \left(-A_0 + \sum A_n \cos n\theta \right) d\theta \quad (56)$$

For the condition where $A_0 = \alpha$, C_D becomes after integrating

$$C_D = \frac{\pi\alpha}{2} \left(C_0 + C_1 - \frac{C_2}{2} \right) + \frac{\pi}{2} \left[\left(\frac{C_1}{4} - \frac{C_2}{2} \right) A_1 + \left(\frac{C_0 + C_1 + \frac{C_4}{2}}{2} \right) A_2 - \frac{A_4 C_2}{4} \right] \quad (57)$$

At infinite depth ($C_0 = A_0$, $C_n = A_n$) equation (57) reduces to the value given by Tulin-Burkart in reference 1.

$$C_{D,\infty} = \frac{\pi}{2} \left(A_0 + \frac{A_1}{2} \right)^2 = \frac{1}{8\pi} (\bar{c}_L)^2 \quad (58)$$

For $A_0 = \alpha$, that is $A_0' = 0$

$$\alpha + \epsilon = \frac{C_D}{\bar{c}_L} = \frac{\frac{\pi\alpha}{2} \left(C_0 + C_1 - \frac{C_2}{2} \right) + \frac{\pi}{2} \left[\left(\frac{C_1}{4} - \frac{C_2}{2} \right) A_1 + \left(\frac{C_0 + C_1 + \frac{C_4}{2}}{2} \right) A_2 - \frac{A_4 C_2}{4} \right]}{\frac{\pi}{2} \left(C_0 + C_1 - \frac{C_2}{2} \right)} \quad (59)$$

Therefore

$$\epsilon = \frac{(C_1 - 2C_2)A_1 + (2C_0 + 2C_1 + C_4)A_2 - A_4 C_2}{4 \left(C_0 + C_1 - \frac{C_2}{2} \right)} \quad (60)$$

The value of ϵ given by equation (60) is adequate only for the case of small angle of attack and camber and depth-chord ratios larger than

about 1. At small spray thickness to chord ratios it may be seen in figure 13 that the spray angle becomes quite large even for small angles of attack. When such a flow is transformed by $\bar{Z} = -\sqrt{Z}$ the cavity streamline and the free water surface are rotated as shown in figure 13. In figure 13(b) the boundary conditions are now different from the simple $\bar{u} = 0$ used in the small-angle theory. If a system of vortices could be located to satisfy the boundary conditions along these new lines, a solution for the resulting vorticity on the foil could be obtained. Such a method would involve taking a different spray angle (from fig. 3) for each depth and angle of attack in order to locate the image vortex or array of vortices. Also, for large angles of attack and spray angles the linearizing assumption of $\bar{v} \ll V$ is not adequate. In calculating the lift, these difficulties were avoided by using Green's solution which takes the effect of the spray angle into account. It can be seen in figure 2 that as the angle of attack increases, the ratio of $\frac{C_L}{C_{L,\infty}}$ diminishes, therefore, the image vortex must have less influence on the resulting hydrofoil vorticity for large angles of attack. An approximation to the correct hydrofoil-vorticity distribution for finite angles of attack operating near the free water surface can be obtained by using the model shown in figure 8, and increasing the value of d/c used so that the resulting $\frac{C_L}{C_{L,\infty}}$ corresponds to that given by Green. Thus, for large angles of attack, camber, and finite aspect ratio an effective depth of submersion, $(d/c)_e$ should be used in equation (60). The value of $(d/c)_e$ is the value of d/c on the $\alpha = 0$ line in figure 2 corresponding to the value of $m = m_e$, where

$$m_e = \frac{C_L}{C_{L,\infty}} \frac{\pi}{2} = \frac{m\{\alpha + \alpha_c - \alpha_i\}}{m\{\alpha + \alpha_c - \alpha_i\}_{\infty}} \frac{\pi}{2} \quad (61)$$

The value of the C coefficients are then determined for $(d/c)_e$ and $A_0 = \alpha - \alpha_i$.

A sample calculation of the drag coefficient is given in appendix B. It has been found after several calculations that the value of ϵ and thus the drag coefficient is not greatly affected by the depth of submersion. In fact, a rough approximation to ϵ may be obtained by assuming $C_0 = \alpha - \alpha_i$, and $C_n = A_n$ in equation (60).

Center of Pressure

The linearized expression for the center of pressure of a finite-aspect-ratio, supercavitating hydrofoil operating at zero cavitation number and finite depth of submersion is

$$x_{c.p.,l} = \frac{C_{m,1}}{C_{L,1}} = \frac{1}{16} \frac{5C_0 + 7C_1 - 7C_2 + 3C_3 - \frac{C_4}{2}}{C_0 + C_1 - \frac{C_2}{2}} \quad (62)$$

where the C coefficients are determined at the effective depth of submersion given by equation (61) and for $A_0 = \alpha - \alpha_i$. Superimposed on this flow is the crossflow component of lift which is assumed to be distributed uniformly over the chord and acting in a direction normal to the chord line. Thus, the distance from the leading edge to the center of pressure of the crossflow-lift component $x_{c.p.,c}$ is given by

$$x_{c.p.,c} = 0.5c \quad (63)$$

Admittedly, this assumption is crude and accurate only for a flat plate. For cambered surfaces the crossflow will not be uniformly distributed and for low drag cambered sections is probably concentrated on the rearward portion of the hydrofoil.

By combining equations (62) and (63) the center of pressure of the combined flows is, therefore,

$$x_{c.p.} = \left(\frac{C_{L,1}x_{c.p.,l} + 0.5C_{L,c}}{C_L} \right) c \quad (64)$$

A sample calculation of the center of pressure is given in appendix B. As in the case of ϵ , a few calculations reveal that a fair approximation for $x_{c.p.,l}$ is obtained by using $C_0 = \alpha - \alpha_i$ and $C_n = A_n$ in equation (62).

EXPERIMENTAL INVESTIGATION

MODELS

Two models of 7.071-inch chord were used in the experimental investigation. As shown in figure 14(a), the first had a lower surface

conforming to the Tulin-Burkart low-drag configuration given by equation (12). The two-dimensional design-lift coefficient was selected as 0.392 corresponding to a value of 0.2 for the coefficient A_1 . Since the hydrofoil is designed to operate in a cavity, the shape of the upper surface is arbitrary as long as it does not interfere with the formation of the cavity from the leading edge. Since the greatest advantage is to be obtained at small angles of attack and thus thin cavities, the thickness of the hydrofoil must be small. For the present cambered model the upper surface profile from leading edge to midchord was arbitrarily chosen to conform with the free streamline leaving the leading edge of a two-dimensional flat plate at 5° incidence. (See ref. 1.) The thickness of the portion rearward of the midchord was made in the image of the forward portion and resulted in a symmetrical thickness distribution with a maximum thickness-chord ratio of 3.3 percent. Since the center of pressure of the Tulin-Burkart hydrofoil is located near the midchord, this symmetrical section minimizes the torsional moment on the foil and results in less twist than would be experienced by a nonsymmetrical section.

The second model was of triangular cross section with a flat bottom as shown in figure 14(b). The maximum thickness was 5 percent of the chord.

Such thin sections lead to structural limitations in the aspect ratio when supported by a single strut at midspan. Since an aspect ratio of 1 is about the most desirable from the structural standpoint and it also represents the accepted dividing line between hydrofoils and hydroskis, both models were made with a square plan form.

The strut, which can also be seen in figure 14, had an NACA 66₁-012 airfoil section. The strut was mounted perpendicular to the flat plate and perpendicular to the X-axis of the cambered surface. The intersection of the strut and upper surface was without fillets. Both the hydrofoil and the strut were made of stainless steel and were polished to a smooth finish.

APPARATUS AND PROCEDURE

Tests were made by using the carriage and existing strain-gage balances in the Langley tank no. 2 which independently measure the lift, drag, and pitching moment. Figure 15 shows a view of the test setup with the cambered hydrofoil and the balance attached to the carriage. The moment was measured about an arbitrary point above the model and the data thus obtained were used to calculate the moments about the leading edge. The positive directions of forces, angles, and moments used in presenting the force data are shown in figure 16.

The force and moment measurements were made at constant speeds for fixed angles of attack and depths of submersion. The depth of submersion is defined as the distance from the undisturbed water surface to the leading edge of the model.

Ventilated or zero-cavitation-number tests were made on both models at a depth of submersion of 0.5 inch throughout a range of angle of attack from 6° to 20° for the flat plate, and 8° to 20° for the cambered hydrofoil. Three methods of obtaining ventilated flow at this 0.5-inch depth were used: (1) Normal ventilation through the trailing vortices as described in reference 4, (2) injection of air through the port on the strut leading edge (see fig. 14) (this air was supplied at a rate of 0.012 pounds per second and cut off after ventilation was established), and (3) a 1/32-inch-diameter wire was soldered on the leading edge of the cambered model to cause local separation and thus ventilation. Both models were also investigated at a depth of submersion of 0 inch at $\alpha = 4^\circ$ for the flat plate, and $\alpha = 6^\circ, 8^\circ$, and 10° for the cambered surface. At angles of attack of 16° and 20° for the flat surface, forces were also measured over a range of depth of submersion for which ventilation could be obtained ($d = 0$ to 2 inches).

The thickness and direction of the jet or spray leaving the leading edge of the flat plate were also measured at 16° and 20° for a range of d from 0 to 2 inches. A schematic drawing of the instrument used for measuring the spray thickness and direction is shown in figure 17. The stagnation tube was lowered through the spray during a test and the pressure and location of the tube center line recorded on an oscillograph. Almost instantaneous response of the stagnation-tube-pressure-cell combination was obtained by completely filling the tube and connecting line with water. The point of entering and leaving the spray was obtained by comparing the location of the tube with the rise and fall of pressure as the tube passed through the spray. The vertical location of the tube was obtained from the output of the slide-wire circuit also shown in figure 8. During a test the tube was passed through the spray several times and an average of the results was taken.

Tests of the nonzero-cavitation-number case were made at a depth of submersion of 6 inches where vortex ventilation did not occur. Measurements of lift, drag, and moment were obtained for a range of velocities from 20 to 80 feet per second at angles from 16° to 20° for which long trailing air or vapor cavities could be obtained. Data for air-filled cavities were obtained by introducing air from an external metered supply to the upper surface through the ports on the strut leading edge shown in figure 14. During these tests the pressure in the cavity formed was measured by a pressure cell connected to a 1/16-inch-diameter orifice located near the bottom of the strut so as to be within the cavity. (See fig. 14.) This measured pressure was used in computing the cavitation

number for the cavity formed. The airflow rate was measured by an orifice-type flow meter. Airflow rates up to 0.012 pound per second were obtained with the test arrangement.

ACCURACY

The change in angle of attack due to structural deflection caused by the forces on the model was obtained during the calibration of the balances and test data were adjusted accordingly. The maximum correction necessary was only 0.1° . The estimated accuracy of the measurements is as follows:

Angle of attack, deg	± 0.1
Depth of submersion, in.	± 0.1
Speed, fps	± 0.2
Lift, lb	± 15
Drag, lb	± 7
Moment, ft-lb	± 6
Cavity pressure, lb/sq ft	± 10
Spray thickness, in.	± 0.05
Spray angle, deg	± 1.5

The forces and moments were converted to the usual aerodynamic coefficient form by using a measured value of the density of 1.93 slugs per cubic foot. The kinematic viscosity measured during the tests was 1.70×10^{-5} pounds-second per square foot. Thus, for the range of velocities investigated, the Reynolds number based on chord ranged from 0.7×10^6 to 2.8×10^6 .

RESULTS AND DISCUSSION

ZERO CAVITATION NUMBER

General

Ventilation inception.- The process of ventilation by air entrainment through the tip vortices of a hydrofoil near the free water surface is described in reference 4 and is shown for the present models operating at a depth of 0.5 inch, in figures 18 and 19. The speed at which complete ventilation occurred, when tested at this depth is shown in figure 20. Complete ventilation by entrainment through the vortices was not possible at angles less than 10° for the flat surface and 12° for the cambered

surface. Figure 18(a) shows the incomplete ventilation of the flat plate at 8° and figure 19(a) the similar action of the cambered surface at 10° . Figure 18(b) shows the complete ventilation of the flat surface at 10° and figures 19(b) and (c), the complete ventilation of the cambered surface at 12° and 16° , respectively. Leading-edge cavitation of both models may be noted in the photographs.

One of the requirements for establishing ventilated flow from the leading edge is that the hydrofoil upper surface lie beneath the upper cavity streamline for the condition of zero cavitation number. Thus, for a given hydrofoil thickness there is a minimum angle below which ventilation from the leading edge cannot exist. Figure 21 shows the theoretical infinite depth location of the upper cavity boundary for two-dimensional hydrofoils having the same cross section as the models tested. These streamlines, computed from equations given in references 1 and 13, reveal that ventilation of the two-dimensional flat plate should be possible at angles greater than 3.2° .

As pointed out in references 1 and 13, the slope of the cavity streamline is determined by the magnitude and distribution of the circulation on the equivalent airfoil section. The reduction of the two-dimensional (infinite depth) circulation by an amount equivalent to Jones' edge correction, $1/E = A/(A + 1)$, will cause the cavity streamline to be lowered over the entire span by an amount proportional to $1/E$. When the induced angle α_i is considered, the streamline is brought even closer to the hydrofoil upper surface, particularly near the tips.

By considering these two effects and by assuming that the influence of α_i is uniform over the span, the effect of finite aspect ratio on the cavity slope $\left(\frac{dy}{dx}\right)_c$ may be approximated by the following equation:

$$\frac{\left(\frac{dy}{dx}\right)_c}{\left[\left(\frac{dy}{dx}\right)_c\right]_{A=\infty}} \approx \frac{\frac{A}{A+1}(\alpha - \alpha_i)}{(\alpha)_{A=\infty}} \quad (65)$$

Thus, in order to establish a cavity at angle of attack α and aspect ratio A which is equivalent to the cavity formed at angle of attack α and $A = \infty$ the following equation must be satisfied:

$$\alpha \approx \frac{A+1}{A}(\alpha)_{A=\infty} + \alpha_i \quad (66)$$

By using equation (66) and the value of $(\alpha)_{A=\infty} = 3.2^\circ$, the geometric angle of attack of the aspect-ratio-1 plate would have to be about 8° in order to ventilate from the leading edge at infinite depth of submersion. The effect of the proximity of the free water surface is to rotate the cavity streamline away from the hydrofoil as seen in figure 3. Thus, it should be possible to establish a vented cavity on the flat section at angles at least as small as 8° when operating near the free water surface. Therefore, the absence of ventilation at angles less than 10° cannot be attributed to interference from the model upper surface. In fact the formation of leading-edge cavitation at 8° indicates that if the velocity could have been increased well above 80 feet per second (preferably to zero cavitation number) a vapor cavity completely inclosing the upper surface would result. The reason that ventilation did not occur at angles less than 10° could be that the region of boundary-layer separation in the midportion of the chord did not extend to the aerated vortices. This conjecture was proved to be the case by injecting air from the external supply down the strut to the upper surface of the model. Complete ventilation of the upper surface was then possible at angles as low as 6° . The air was supplied (at the maximum rate of 0.012 pound per second) during the acceleration of the model and shut off after ventilation was established. The process is shown in figure 18(c) for the flat plate at 8° angle of attack.

Figure 21 shows that ventilation of the two-dimensional cambered section should be possible at angles above about 4° . In reference 13 at large angles of attack, the cavity shape is almost independent of the camber, depending only on the angle of attack. Therefore, the finite-aspect-ratio corrections given by equations (65) and (66) are assumed applicable to cambered sections. When these corrections for finite aspect ratio are taken into account the minimum angle for ventilation of the cambered section becomes about 12° . Again the proximity of the free water surface will reduce this infinite-depth estimate. Thus, failure to establish complete ventilation of this hydrofoil at angles less than 12° (at $d = 0.5$ inch) may have been due to interference of the upper boundary of the model. In fact it was found that injecting air to the upper surface at angles less than 12° failed to establish ventilation or to influence the ventilation speed at 12° . Since the lift-drag ratio of cambered supercavitating hydrofoils increases with decrease in angle of attack, these observations suggest the use of higher geometric aspect ratios or the effective increase of aspect ratio by the use of end plates. End plates appear to be particularly applicable if low-aspect-ratio cambered hydrofoils are to be designed to ventilate from the leading edge at small angles of attack and large depths of submersion.

Since complete ventilation seemed to require extensive boundary-layer separation on the upper surface, a $1/32$ -inch diameter wire was soldered on the leading edge of the cambered model to cause a local boundary-layer separation. With this wire in place it was possible at

the 0.5-inch depth of submersion to obtain complete vortex ventilation of the upper surface at 10° incidence but not at 8° incidence even at the maximum available velocity of 80 feet per second. However, by introducing air through the ports on the strut it was possible to obtain complete ventilation at angles as low as 8° . Evidently air brought up by the tip vortices at 8° incidence could not reach the small separated region behind the wire; however, the forced air was capable of reaching this zone and establishing a cavity. The cavity formed extended downstream far enough to intercept the ventilated tip vortices and complete ventilation then occurred. Of course, the primary influence of the wire was to increase the cavity ordinates so that the hydrofoil upper surface did not interfere with establishing ventilation from the wire. Although the basic force data obtained with the wire were recorded and are presented, they are not used in the later correlation with theory because of the unknown influence of the wire on the forces.

Basic force and moment results.- The basic data from the tests of the ventilated hydrofoils at a depth of submersion of 0.5 inch are presented in figure 22 for the flat plate and figure 23 for the cambered surface as curves of lift, drag, and pitching moment about the leading edge against speed, for various angles of attack. Ventilated-flow data obtained at zero depth of submersion at 4° incidence for the flat plate and 6° , 8° , and 10° for the cambered surface are also included.

The basic ventilated flow data obtained for depths of 0, 1.0, 1.5, and 2.0 inches for incidences of 16° and 20° are presented in figure 24.

Comparison of Experimental Results With Theory

Spray thickness.- In the section on theory the need for determining the relationship between the leading-edge depth of submersion and the spray thickness for a flat plate was pointed out. These variables were measured for the flat plate at 16° and 20° over the range of depth of submersion from 0 to 2 inches. The data are shown in figure 25. The spray-thickness measurements presented were obtained approximately 20 percent of the chord rearward of the leading edge. On one test, measurement of the spray thickness was also obtained at about the midchord and the results were in agreement with those obtained at the 20-percent location. Therefore, for the range of depths investigated, the spray thickness measured can be considered as the theoretical value infinitely rearward of the foil. It may be noted in figure 25 that the spray thickness is greater than the leading-edge depth of submersion, the magnitude of the ratio increases with either increase in angle of attack or decrease in depth of submersion. Also shown in figure 25 are the theoretical relationships between δ/c and d/c for the two-dimensional 0° and 90° cases previously discussed. It may be noted that the trends of the experimental and theoretical curves are parallel.

In foregoing sections it has been pointed out that the relationship between leading-edge depth of submersion and spray thickness is influenced by the force of gravity and thus cannot be obtained from Green's analysis. Also the influence of aspect ratio has been shown to be important. The relationship for $\alpha = 0^\circ$ and 90° has been determined but the manner in which intermediate angles of attack affect the result was not understood. The data shown in figure 25 combined with the end-point results previously established for $\alpha = 0^\circ$ and 90° permit lines of constant d/c , at least for the aspect-ratio-1 condition, to be drawn on figure 2. The experimental data shown in figure 25 were plotted on figure 2 at their equivalent angle of attack $\alpha - \alpha_i$. This corresponds to equivalent angles of attack of approximately 12.3° for the 16° case and 15.9° for the 20° case for the range of d/c presented. For values of d/c greater than 0.285, only the theoretical end points were available and paralleling lines were faired in. Although these lines are accurate only for the aspect-ratio-1 condition, they are considered to be good approximations even for aspect ratios as high as 6. Such an approximation is reasonable because the asymptotic value of the stagnation line infinitely forward of a flat plate is only of the order of about 0.1 chord below the stagnation point for aspect ratios less than 6 and lift coefficients less than 0.5. It is obvious from figure 2 that for depths greater than 1 chord, the end points may be connected by any reasonable line (for example, a straight line) with very little loss in accuracy.

Spray angle.—Figure 26 shows the effect of depth of submersion on the spray angle ϕ for the flat plate at 16° and 20° . The theoretical spray-angle variation also shown in figure 26 was obtained from figure 3 by considering the two-dimensional angle of attack as $\alpha - \alpha_i$ and the two-dimensional d/c as the actual measured value. The tangent of the spray angles obtained from figure 3 for the angle $\alpha - \alpha_i$ were then reduced by the factor $1/E$. The justification for this $1/E$ modification is the same as that presented in the section on ventilation inception. That is, that the slope of the upper cavity streamline is proportional to the equivalent airfoil circulation and thus if the two-dimensional circulation is reduced by $1/E$, the two-dimensional spray-angle slope will also be reduced by this amount. When these three-dimensional corrections are made, the calculated angles are still high at small values of d/c and appear to coincide with the experimental data for values of d/c greater than about 0.25. Since the theorem that the slope of the cavity streamline is directly proportional to the circulation was obtained in reference 1 for very thin cavities at infinite depth; it cannot be expected to be applicable when the spray angles are very large. This deviation from assumed small angles may be the only explanation required for the discrepancy between theory and experiment at small values of d/c . However, it might also be attributed to the influence of gravity and finite aspect ratio on Green's solution. In the section entitled

"Relation Between Depth of Submersion and Spray Thickness," it was suggested that the spray angles given in figure 3 would be reduced because of these effects and at least this assumption has not been disproved by the experimental data.

Lift coefficient.- All ventilated force and moment data in coefficient form were found to be independent of speed in the range tested. (This independence was true in the present investigation because of the shallow depth of submersion and therefore $\sigma \cong 0$. At very large depths, σ will be greater than zero because p_o is greater than p_c even if the cavity is fully vented to the atmosphere. Therefore at large depths, changes in velocity will affect the lift coefficient because these changes affect σ .) The data shown in figures 22(a) and 23(a) are plotted in figure 27 as lift coefficient against angle of attack for each of the models tested. A comparison of the lift coefficients of the two models shows an effective increase in angle of attack of the cambered model as predicted by the Tulin-Burkart theory. Also shown in figure 27 are the theoretical lift-coefficient curves obtained from equation (50). The theory is about 3 percent lower than the measured values. Thus, the use of equation (50) in engineering calculations of the lift coefficient appears to be warranted.

The variation of lift coefficient with depth of submersion of the flat-plate model at angles of incidence of 16° and 20° is shown in figure 28. Note the slight increase in lift coefficient as the hydrofoil nears the surface. Also shown in figure 28 is the theoretical variation of the lift with depth of submersion obtained from equation (50). The theory is in excellent agreement with the data and accurately predicts the increase in lift with decreasing depth of submersion.

Further verification of equation (50) is shown in figure 29 where a comparison is made with the experimental data of Fuller (ref. 17). These data were obtained on sections with lower surface profiles similar to those of the present investigation but at an aspect ratio of 2. The calculated values are in good agreement with the measured values for both the flat and cambered models.

Drag coefficient.- In figure 30 the data of figures 22(b) and 23(b) in coefficient form are compared with theoretical values obtained from equation (51). The friction drag coefficient of one side of either of the models was calculated to be about 0.003. With the strut drag included, the total-skin-friction drag coefficient C_f was taken as 0.004. By using this value of C_f in equation (51), the agreement between theory and experiment is good for both models.

In figure 31 the experimental lift-drag ratios obtained from the data of figures 22 and 23 are compared with theory. Again, both experiment and theory include the skin-friction drag coefficient ($C_f = 0.004$).

The agreement between theory and experiment is good for both models. The superiority of the cambered hydrofoil is clearly revealed in this figure. At a lift coefficient of 0.25 the L/D of the cambered hydrofoil is more than twice that of the flat plate.

Also included in figure 31 are data taken from reference 4 on a ventilated modified flat plate of aspect ratio 1. This modified plate had an elliptical nose and a tapered trailing edge. The importance of providing a sharp leading edge on hydrofoils designed for use in cavity flow is shown by comparing the L/D of this modified flat plate with the L/D of the sharp-nosed flat plate of the present investigation. The rounded leading edge of the modified plate is subjected to a net positive pressure which is not balanced by similar pressures on the rearward portion of the plate. In addition, the lower surface of this plate presents an effective negative camber to the flow and thus does not develop as much lift as a truly flat surface. At small angles the drag of the rounded nose greatly influences the maximum L/D of the section. Several other investigations have noted the importance of a sharp leading edge on hydrofoils designed for operation in the supercavitating regime. (See refs. 18 and 19.)

Center of pressure. - The center of pressure of the flat and cambered models calculated from the data of figures 22 and 23 are compared with theory in figure 32. The theory from equation (64) is in good agreement with the experimental data for both models. Since the accuracy of the forces and moments on the flat plate is poor at small angles of attack (small total loads) the accuracy of the center of pressure from the data obtained on the flat plate at angles of incidence of 4° and 6° is doubtful.

NONZERO CAVITATION NUMBER

The nonzero-cavitation-number characteristics of the two models obtained at a 6-inch depth of submersion are shown in figure 33 for angles of attack of 16°, 18°, and 20°. The solid data points are the lift coefficients obtained for vapor cavitation. The cavitation number corresponding to the condition tested was computed by using the water vapor pressure at the test temperature for the pressure within the cavity (that is $\sigma = \frac{P_o - P_v}{q}$). For cavitation numbers less than about 0.7 the vapor pressure was the same as the measured cavity pressure. However, at cavitation numbers greater than 0.7, the measured pressure was usually higher than the vapor pressure. Since it could not be determined with certainty whether the cavity pressure orifice was within the cavity, the vapor pressure was used to compute all cavitation numbers denoted by the solid data points. Also denoted in figure 33 are the approximate values of σ at inception σ_i and the point at which the cavity length exceeded the chord.

These values are only estimates, since no effort was made to find the exact velocity at which these incidents occurred. Although the estimated values of σ_1 are the same for both models, there may actually be some difference in the true points.

The blank data points in figure 33 represent data obtained by introducing air to the upper surface of the model and establishing a cavity. The cavitation number for this condition was computed by using the measured value of the pressure within the cavity. In this case the cavity pressure orifice was always well within the cavity formed.

In figure 33 the curves are drawn through the computed value of C_L for $\sigma = 0$ as obtained from equation (50).

The agreement between the vapor- and air-cavity data confirms the use of the cavitation number as the significant parameter for correlating the characteristics of cavity flow. The similarity of the air and vapor cavities at nearly equal cavitation number is shown in figure 34. This dependence on the cavitation number is to be expected because the forces on the body are influenced only by the streamline curvatures and thus the pressure within the cavity; the type of gas present should have only a secondary influence.

It was not possible to establish satisfactory air cavities at angles less than about 16° . At low speeds where the air could reach the separated region near the leading edge the cavity upper surface was greatly disturbed by the force of the air jets. At higher velocities either the air could not reach far enough upstream to form a cavity or when a cavity was formed it did not cover the whole chord. If a greater quantity of air is supplied it is believed that satisfactory results can be obtained at angles less than 16° .

The use of a dynamic model of a high-speed aircraft will require simultaneous reproduction of both the full-scale cavitation and Froude numbers. Such an investigation is possible if an air-filled cavity with the proper cavitation number can be established on the model.

CONCLUSIONS

Conclusions based on the results obtained from the theoretical and experimental investigations of supercavitating flat and cambered hydrofoils may be summarized as follows:

1. The theoretical expressions derived for the lift, drag, and center of pressure of supercavitating hydrofoils of arbitrary section

operating at zero cavitation number, and finite aspect ratio and depth of submersion are in good enough agreement with the available experimental data to warrant their use in engineering calculations.

2. The experimental ventilated force and moment coefficients of both models investigated at shallow depths of submersion were independent of speed.

3. Similar to the influence of camber on a fully wetted airfoil, the influence of camber in ventilated flow was to effectively increase the angle of attack without appreciably changing the lift-curve slope.

4. The lift-drag ratio of the cambered model near the design lift coefficient was more than twice that of the flat plate.

5. Comparison of the sharp-nosed flat plate with a rounded-nose flat plate showed the sharp-nosed section to be considerably superior. Thus, hydrofoils designed for operation in the supercavitating regime of flow should have sharp leading edges for best efficiency.

6. The cavitation number defines the flow similarity and lift of a supercavitating hydrofoil regardless of the type of gas (air or water vapor) within the cavity. Thus vapor cavities, normally obtained at high speeds can be simulated at lower speeds by establishing a cavity with forced air whose cavitation number is the same as that of the high-speed flow.

Langley Aeronautical Laboratory,
National Advisory Committee for Aeronautics,
Langley Field, Va., August 27, 1957.

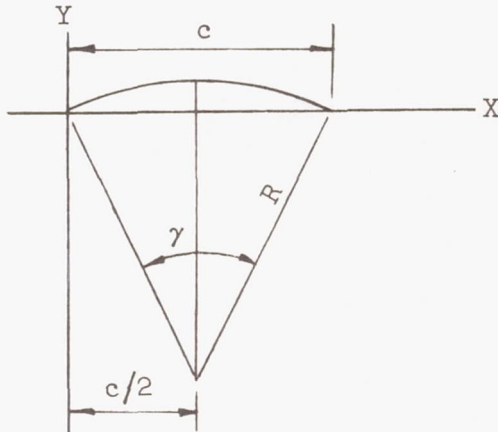
APPENDIX A

THE TULIN-BURKART LINEAR THEORY FOR ZERO-CAVITATION-NUMBER
 FLOW APPLIED TO A CIRCULAR-ARC HYDROFOIL

The problem is to find the effective increase in angle of attack due to the camber of a two-dimensional circular-arc hydrofoil operating at infinite depth and zero cavitation number by the method of reference 1, that is, to find the section coefficients A_0 , A_1 , and A_2 in the following equation if α , measured from the chord line, is zero:

$$C_L = \frac{\pi}{2} \left(A_0' + A_1 - \frac{A_2}{2} \right) = \frac{\pi}{2} (A_0' + \alpha_c)$$

By using the system of axes shown in the following sketch



and the notation of reference 1 (barred symbols for the equivalent airfoil and unbarred for the hydrofoil), the equation of the circular-arc hydrofoil is

$$(x - c/2)^2 + (y + R \cos \gamma/2)^2 = R^2 \quad (A1)$$

$$\frac{dy}{dx} = - \frac{x - c/2}{\sqrt{R^2 - (x - c/2)^2}} \quad (A2)$$

From reference 1 the slope of the equivalent airfoil is obtained from the equation

$$\frac{d\bar{y}}{d\bar{x}}(\bar{x}) = \frac{dy}{dx}(\bar{x}^2) \quad (A3)$$

By noting that $c = \bar{c}^2$, the slope of the equivalent airfoil section is, therefore,

$$\frac{d\bar{y}}{d\bar{x}} = - \frac{\bar{x}^2 - \bar{c}^2/2}{\sqrt{R^2 - (\bar{x}^2 - \bar{c}^2/2)^2}} \quad (A4)$$

If the conventional substitution of

$$\bar{x} = \frac{\bar{c}}{2}(1 - \cos \theta) \quad (A5)$$

is made, equation (4) after some manipulation may be written as

$$\frac{d\bar{y}}{d\bar{x}} = - \frac{\frac{1}{2}(1 - \cos \theta)^2 - 1}{\sqrt{\frac{R^2}{\bar{c}^4} - \left[\frac{1}{2}(1 - \cos \theta)^2 - 1 \right]^2}} \quad (A6)$$

but

$$\frac{\frac{R^2}{\bar{c}^4}}{\frac{1}{4}} = \frac{R^2}{\frac{c^2}{4}} = \left(\frac{R}{c/2} \right)^2 = \left(\frac{1}{\sin \frac{\gamma}{2}} \right)^2 \quad (A7)$$

Therefore,

$$\frac{d\bar{y}}{d\bar{x}} = - \frac{1}{2} \frac{\cos^2 \theta - 2 \cos \theta - 1}{\sqrt{\frac{1}{\sin^2 \frac{\gamma}{2}} - \left(\frac{\cos^2 \theta - 2 \cos \theta - 1}{2} \right)^2}} \quad (A8)$$

Since the linear theory is applicable only to small γ and, therefore,

$$\frac{1}{\sin^2 \gamma} \gg \left(\frac{\cos^2 \theta - 2 \cos \theta - 1}{2} \right)$$

equation (A8) may be approximated as

$$\frac{dy}{dx} \approx - \frac{\gamma}{4} (\cos^2 \theta - 2 \cos \theta - 1) \quad (A9)$$

The necessary coefficients are then readily obtainable as

$$A_0' = - \frac{1}{\pi} \int_0^\pi \frac{dy}{dx} d\theta = - \frac{\gamma}{8} \quad (A10)$$

$$A_1 = \frac{2}{\pi} \int_0^\pi \frac{dy}{dx} \cos \theta d\theta = \frac{\gamma}{2} \quad (A11)$$

$$A_2 = \frac{2}{\pi} \int_0^\pi \frac{dy}{dx} \cos 2\theta d\theta = - \frac{\gamma}{8} \quad (A12)$$

$$A_n = 0 \quad (n > 2) \quad (A13)$$

The required effective increase in angle of attack due to small circular-arc camber is, therefore,

$$\alpha_c = A_1 - \frac{A_2}{2} = \frac{\gamma}{2} - \frac{1}{2} \left(- \frac{\gamma}{8} \right) = \frac{9}{16} \gamma \quad (A14)$$

It should be noted that for the reference line used in the analysis, A_0' is not zero and positive lower surface pressures cannot possibly be realized near the leading edge unless the angle of attack is increased at

least to the point where $\alpha - \frac{\gamma}{8} = 0$. Since $A_n = 0$ (with $n > 2$) and $A_1 \sin \theta + A_2 \sin 2\theta$ is everywhere positive in the interval $0 \leq \theta \leq \pi$, the condition $\alpha - \frac{\gamma}{8} = 0$ is sufficient to specify positive pressures over the entire chord of the hydrofoil.

A convenient way of treating the circular-arc section to make it comparable to other low-drag sections is to reorient its reference line so that $\alpha_0 = \frac{\gamma}{8}$, that is, $A_0' = 0$. This orientation then corresponds to $\alpha = 0$. At this design angle of attack ($\alpha = 0$, $\alpha_0 = \frac{\gamma}{8}$) the hydrodynamic efficiency C_L/C_D of a two-dimensional circular-arc section as computed from linear theory is $\frac{81}{16} \frac{\pi}{2C_L}$, which is almost as good as the low-drag hydrofoil selected in reference 1, $\left(\frac{C_L}{C_D} = \frac{100}{16} \frac{\pi}{2C_L} \right)$.

APPENDIX B

SAMPLE CALCULATION OF LIFT, DRAG, AND CENTER OF PRESSURE
 OF A CAMBERED LIFTING SURFACE OPERATING AT FINITE
 DEPTH AND ZERO CAVITATION NUMBER

A sample calculation of the lift, drag, and center of pressure is presented for a Tulin-Burkart section with $A_1 = 0.2$ ($C_{L,d} = 0.392$), having an aspect ratio of 1 and operating at an angle of attack of 12° and depth of submersion of 0.071 chord.

LIFT COEFFICIENT

Step 1

For the Tulin-Burkart hydrofoil section $\left(A_2 = -\frac{A_1}{2}\right)$, from equation (7),

$$\alpha_{c,\infty} = A_1 - \frac{A_2}{2} = \frac{5A_1}{4} = 0.25$$

Step 2

From figure 11 at $d/c = 0.071$,

$$\frac{\alpha_c}{\alpha_{c,\infty}} = 0.718$$

Therefore,

$$\alpha_c = (0.718)(0.25) = 0.18$$

Step 3

By assuming that $C_{L,1} = 0.25$ and $\tau = 0.12$ and by using equation (46),

$$\alpha_1 = 1.12 \frac{0.25}{\pi} = 0.088$$

and

$$\alpha + \alpha_c - \alpha_1 = \frac{12}{57.3} + 0.18 - 0.088 = 0.301 \text{ radian} = 17.2^\circ$$

From figure 2 for $d/c = 0.071$ and $\alpha = 17.2^\circ$, it is found that $m = 1.63$; therefore, from reference 11, $\tau = 0.12$ as assumed. By using equation (50),

$$C_{L,1} = \frac{1}{2}(1.63)(0.301) \frac{\cos 12^\circ}{\cos 17.2^\circ} = 0.251$$

This should check with the original assumption - if not, repeat step 3 with better approximation for C_L and τ .

Step 4

For the Tulin-Burkart section given by equation (12) with $A_1 = 0.2$,

$$\frac{y(1)}{c} = - \frac{A_1}{6}$$

Therefore,

$$\alpha_o = \tan^{-1} 0.033 = 1.92^\circ$$

and

$$\alpha' = 12^\circ + 1.92^\circ = 13.92^\circ$$

$$\alpha_c = 0.18 \text{ radian} = 10.3^\circ$$

or

$$\alpha' + \alpha_c = 24.22^\circ$$

By using equation (48),

$$C_{L,c} = \frac{1}{2} 0.88 \sin^2(24.22) \cos 13.92^\circ = 0.072$$

Thus, the required lift coefficient is

$$C_L = C_{L,1} + C_{L,c} = 0.251 + 0.072 = 0.323$$

DRAG COEFFICIENT

Step 1

From step 3 in the lift-coefficient calculation,

$$\alpha + \alpha_c - \alpha_l = 17.2^\circ$$

For $d/c = 0.071$, $m = 1.63$; and for $d/c = \infty$, $m = 1.2$. Therefore, from equation (61)

$$m_e = \frac{1.63}{1.2} \frac{\pi}{2} = 2.13$$

From figure 2 by using the $\alpha = 0$ line with $m = 2.13$, it can be found that

$$(d/c)_e = 0.66$$

Step 2

If a (the distance to airfoil center of pressure) is assumed to be 0.37, then from figure 9 for $a = 0.37$ and $d/c = 0.66$, the following values are found:

$$B_0 = 0.56$$

$$B_1 = 0.15$$

$$B_2 \cong 0$$

From equation (35) for $A_0 = \alpha - \alpha_i = 0.121$, $A_1 = 0.2$ and $A_2 = -0.1$. The values of C_0 , C_1 , and C_2 may be determined as

$$C_0 = 0.212$$

$$C_1 = 0.181$$

$$C_2 = -0.1$$

and from equation (29), $a = 0.367$, which checks with the assumed value. If the resulting value of a differs enough from the assumed value to affect the values of the B coefficients, step 2 should be repeated.

Step 3

From equation (60) the value of ϵ is determined as

$$\epsilon = 0.0013 \text{ radian} = 0.065^\circ$$

Step 4

From equation (51),

$$C_{L,1} = 0.251 \quad C_{L,c} = 0.072 \quad C_f = 0.004$$

Therefore,

$$C_D = 0.251 \tan(12.065^\circ) + 0.072 \tan(13.92^\circ) + 0.004 = 0.075$$

CENTER OF PRESSURE

Step 1

From step 2 of the drag-coefficient calculation,

$$C_0 = 0.212 \quad C_1 = 0.181 \quad C_2 = -0.1$$

Thus, from equation (62),

$$x_{c.p.,1} = 0.43c$$

Step 2

From equation (64) and by using

$$C_{L,1} = 0.251$$

and

$$C_{L,c} = 0.072$$

it is found that

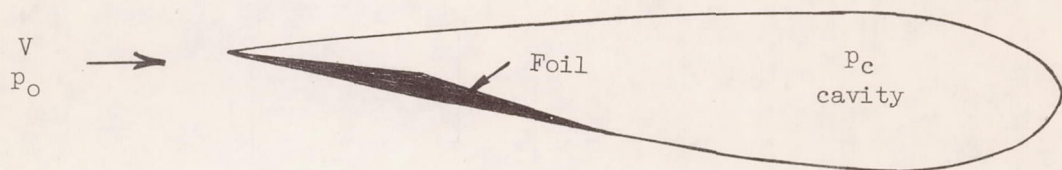
$$x_{c.p.} = 0.45c$$

REFERENCES

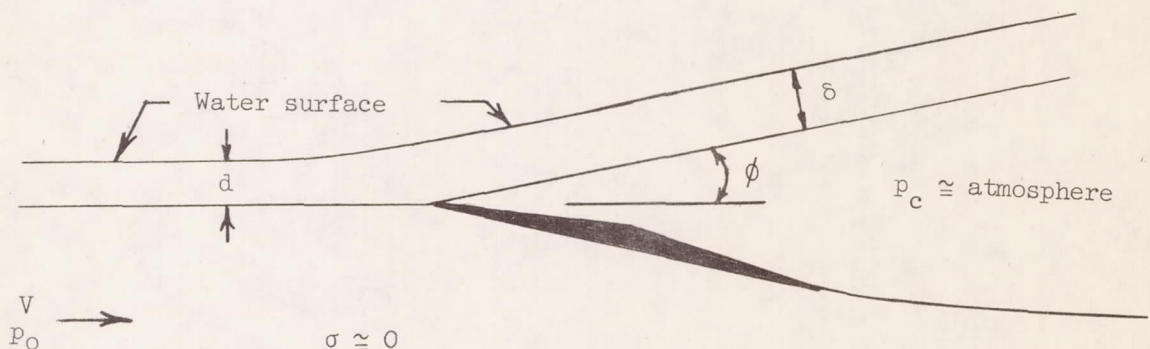
1. Tulin, M. P., and Burkart, M. P.: Linearized Theory for Flows About Lifting Foils at Zero Cavitation Number. Rep. C-638, David W. Taylor Model Basin, Navy Dept., Feb. 1955.
2. Green, A. E.: Note on the Gliding of a Plate on the Surface of a Stream. Proc. Cambridge Phil. Soc., vol. XXXII, pt. 2, May 1936, pp. 248-252.
3. Perry, Byrne: Experiments on Struts Piercing the Water Surface. Rep. No. E-55.1 (Contract N123s-91875), C.I.T., Hydrod. Lab., Dec. 1954. (Available from ASTIA as AD No. 56179.)
4. Eisenberg, Phillip: On the Mechanism and Prevention of Cavitation. Rep. 712, David W. Taylor Model Basin, Navy Dept., July 1950.
5. Wadlin, Kenneth L., Ramsen, John A., and Vaughan, Victor L., Jr.: The Hydrodynamic Characteristics of Modified Rectangular Flat Plates Having Aspect Ratios of 1.00, 0.25, and 0.125 and Operating Near a Free Water Surface. NACA Rep. 1246, 1955. (Supersedes NACA TN's 3079 by Wadlin, Ramsen, and Vaughan and 3249 by Ramsen and Vaughan.)
6. Lamb, Horace: Hydrodynamics. Reprint of sixth ed. (first American ed.) Dover Publications, 1945.
7. Milne-Thompson, L. M.: Theoretical Hydrodynamics. Second ed. MacMillan and Co., Ltd., 1949.
8. Rosenhead, L.: Resistance to a Barrier in the Shape of an Arc of Circle. Proc. Roy. Soc. (London), ser. A, vol. 117, no. 777, Jan. 2, 1928, pp. 417-433.
9. Wu, T. Yao-tsui: A Free Streamline Theory for Two-Dimensional Fully Cavitated Hydrofoils. Rep. No. 21-17 (Contract N6onr-24420), C.I.T., Hydrod. Lab., July 1955.
10. Wagner, Herbert: Planing of Watercraft. NACA TM 1139, 1948.
11. Weighardt, Karl: Chordwise Load Distribution of a Simple Rectangular Wing. NACA TM 963, 1940.
12. Glauert, H.: The Elements of Airfoil and Airscrew Theory. Second ed., Cambridge Univ. Press, 1947. (Reprinted 1948.)

13. Johnson, Virgil E., Jr.: Theoretical Determination of Low-Drag Supercavitating Hydrofoils and Their Two-Dimensional Characteristics at Zero Cavitation Number. NACA RM L57G11a, 1957.
14. Jones, Robert T.: Correction of Lifting-Line Theory for the Effect of the Chord. NACA TN 817, 1941.
15. Shuford, Charles L., Jr.: A Theoretical and Experimental Study of Planing Surfaces Including Effects of Cross Section and Plan Form. NACA TN 3939, 1957.
16. Flax, A. H., and Lawrence, H. R.: The Aerodynamics of Low-Aspect-Ratio Wings and Wing-Body Combinations. Rep. No. CAL-37, Cornell Aero. Lab., Inc., Sept. 1951.
17. Fuller, Roger D.: Model Experiments With Hydrofoils and Wedges for Rough Water Seaplane Design. Rep. No. ZH-102 (Contract NOa(s)-12143), CONVAIR, July 1955.
18. Parkin, Blaine R.: Experiments on Circular Arc and Flat Plate Hydrofoils in Noncavitating and Full Cavity Flow. Rep. No. 47-6 (Contract Nonv-220(12)), C.I.T., Hydrod. Lab., Feb. 1956.
19. Newman, J. N.: Super Cavitating Flow Past Bodies With Finite Leading Edge Thickness. Rep. 1081, David Taylor Model Basin, Navy Dept., Sept. 1956.

$$\sigma = \frac{p_o - p_c}{q} = \frac{p_o - p_v}{q} \text{ for vapor cavitation}$$



(a) Supercavitating flow at great depth of submersion.



(b) Supercavitating or ventilated flow near the free surface.

Figure 1.- Definition sketch.

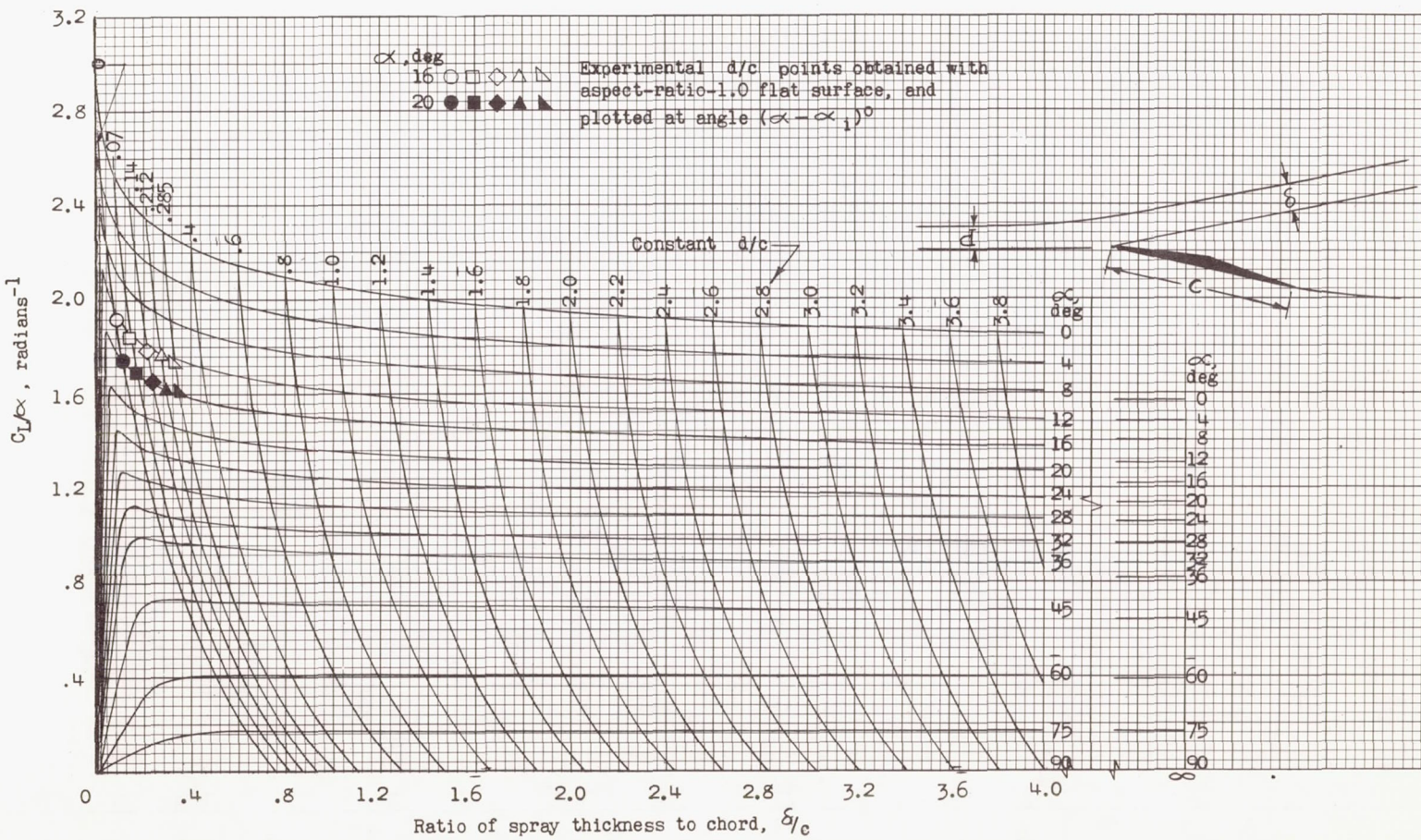


Figure 2.- Green's solution for lift-curve slope of a two-dimensional ventilated flat plate with approximate lines of constant ratio of depth of submersion to chord d/c .

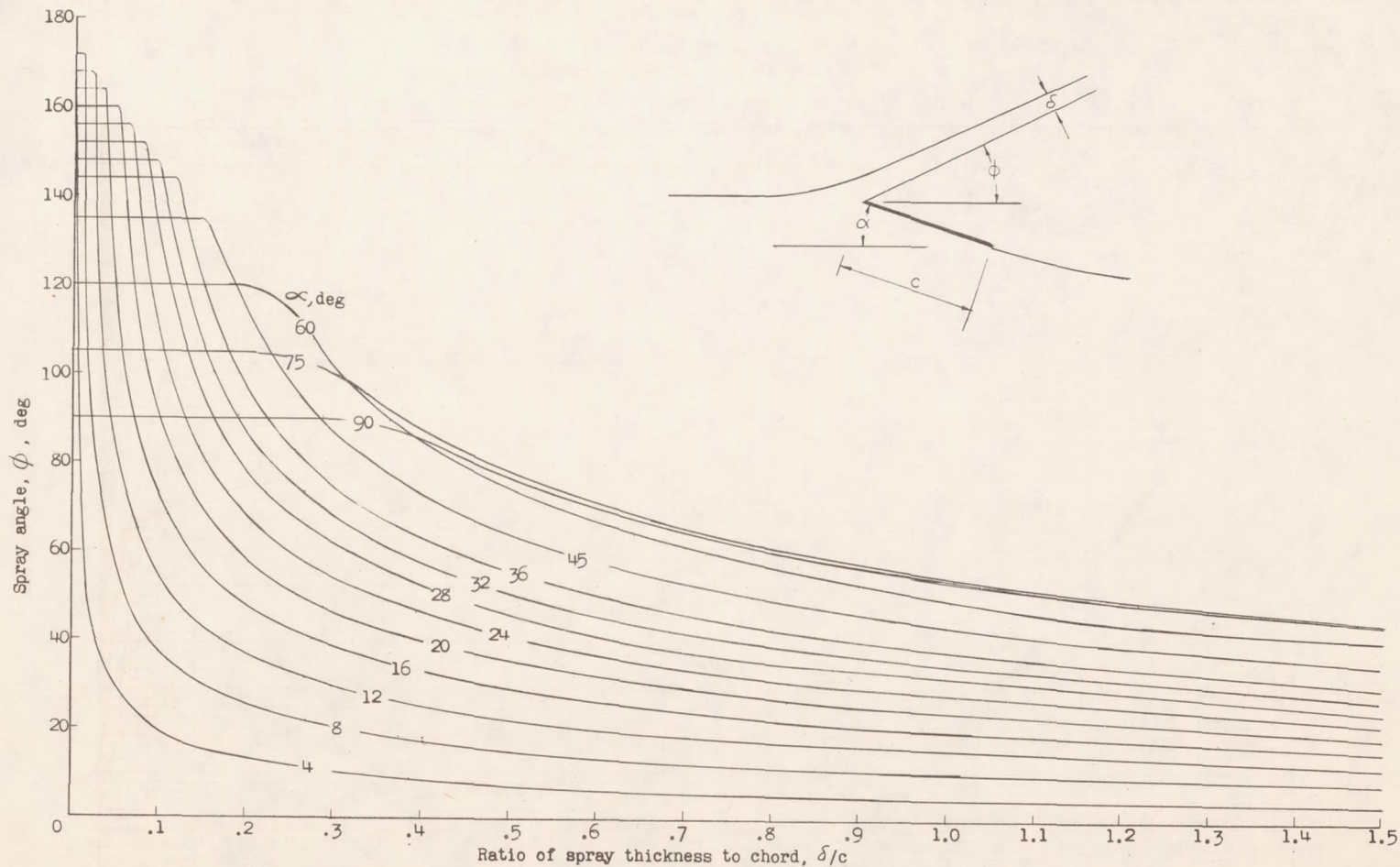


Figure 3.- Green's solution for effect of spray thickness on spray angle of two-dimensional flat plate.

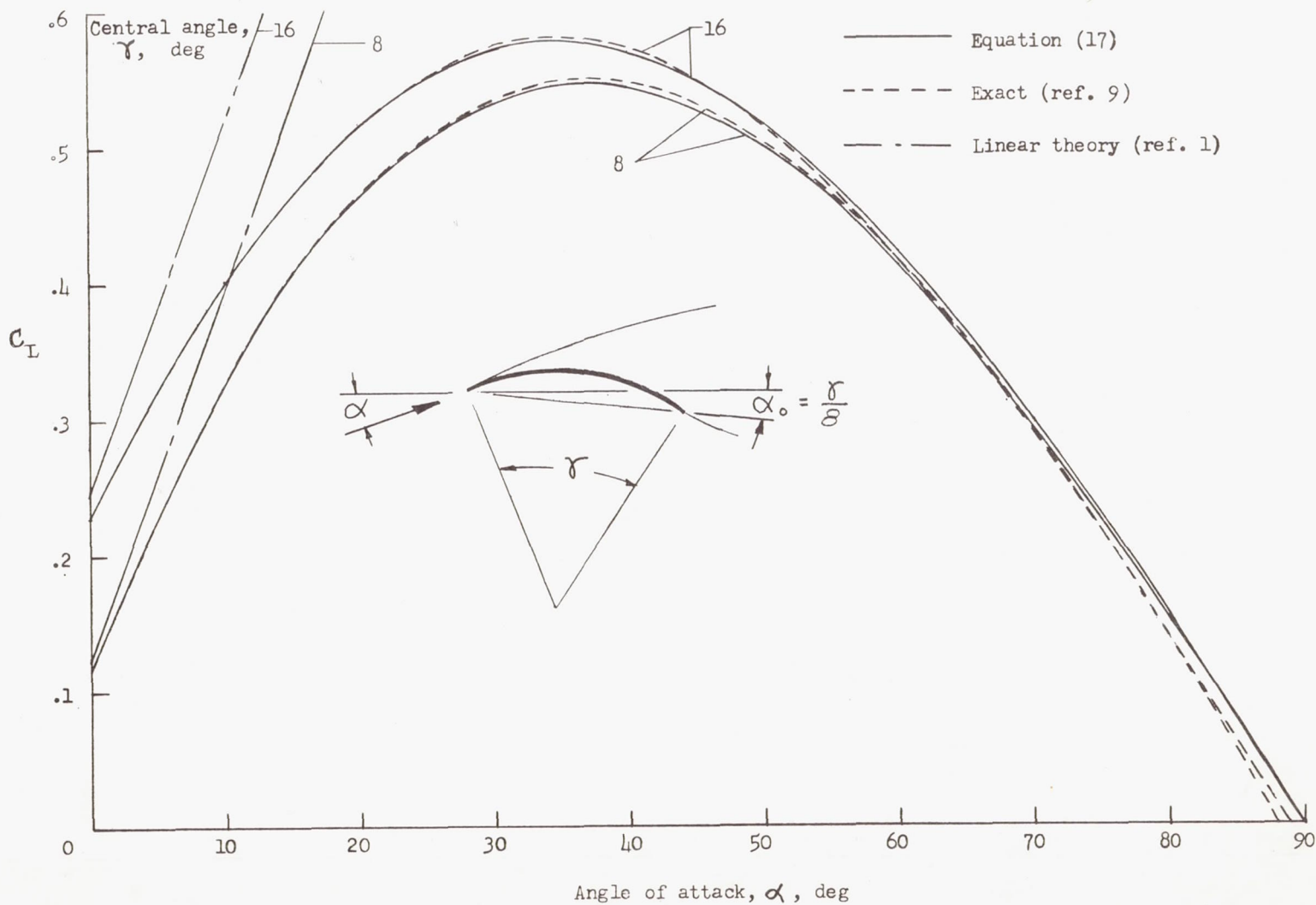
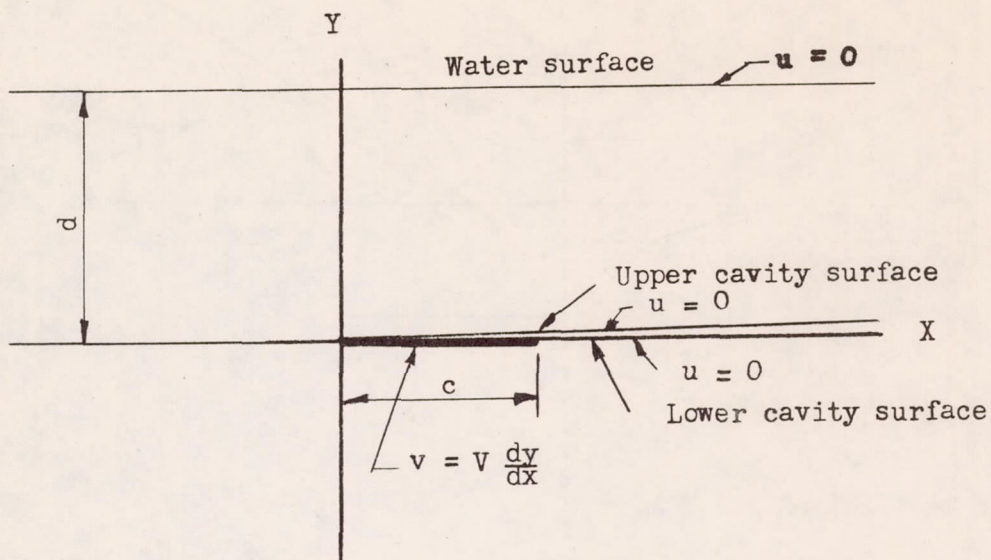
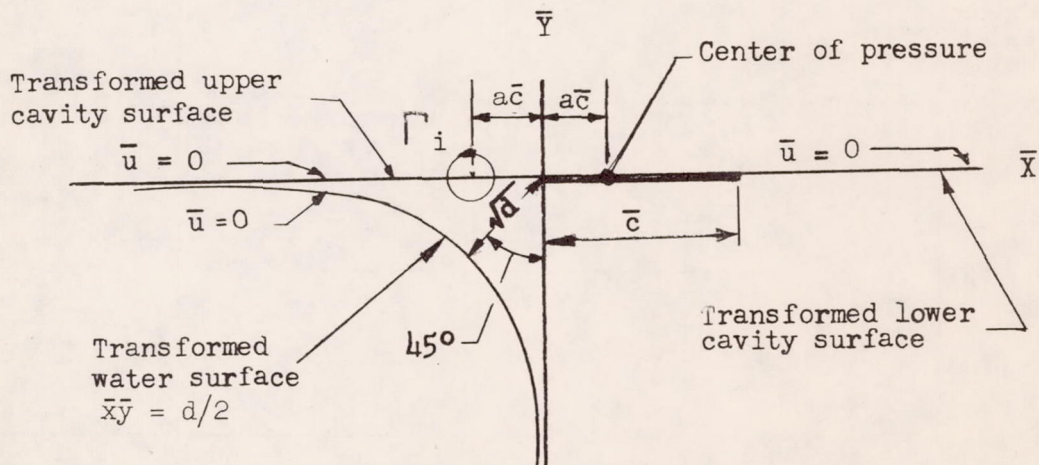


Figure 4.- Two-dimensional theories for lift coefficient of circular-arc hydrofoil at zero cavitation number and infinite depth of submersion.



(a) Hydrofoil, Z-plane.



(b) Equivalent airfoil, Z-bar-plane.

Figure 5.- Linearized boundary conditions in hydrofoil and equivalent airfoil planes.

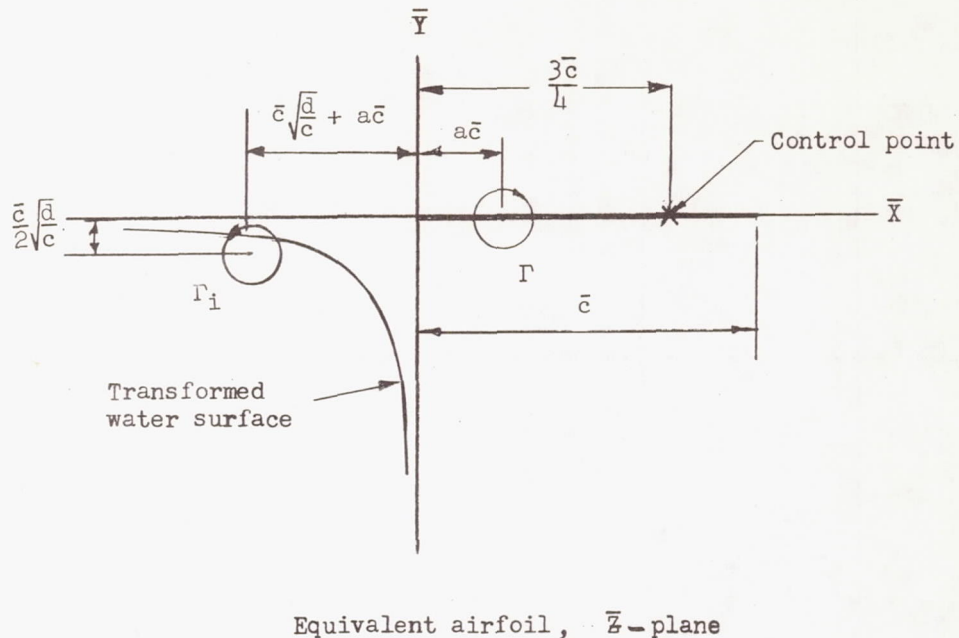


Figure 6.- Linearized model for calculating effect of depth of submersion on lift coefficient of flat plate ($\sigma = 0$).

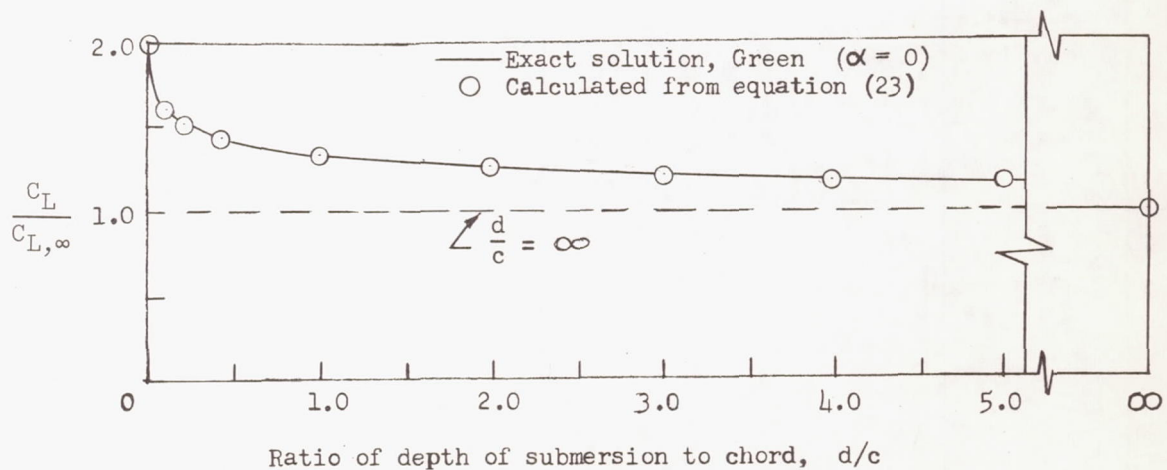


Figure 7.- Comparison of linearized solution with exact solution for effect of depth of submersion on lift coefficient of a flat plate ($\sigma = 0$).

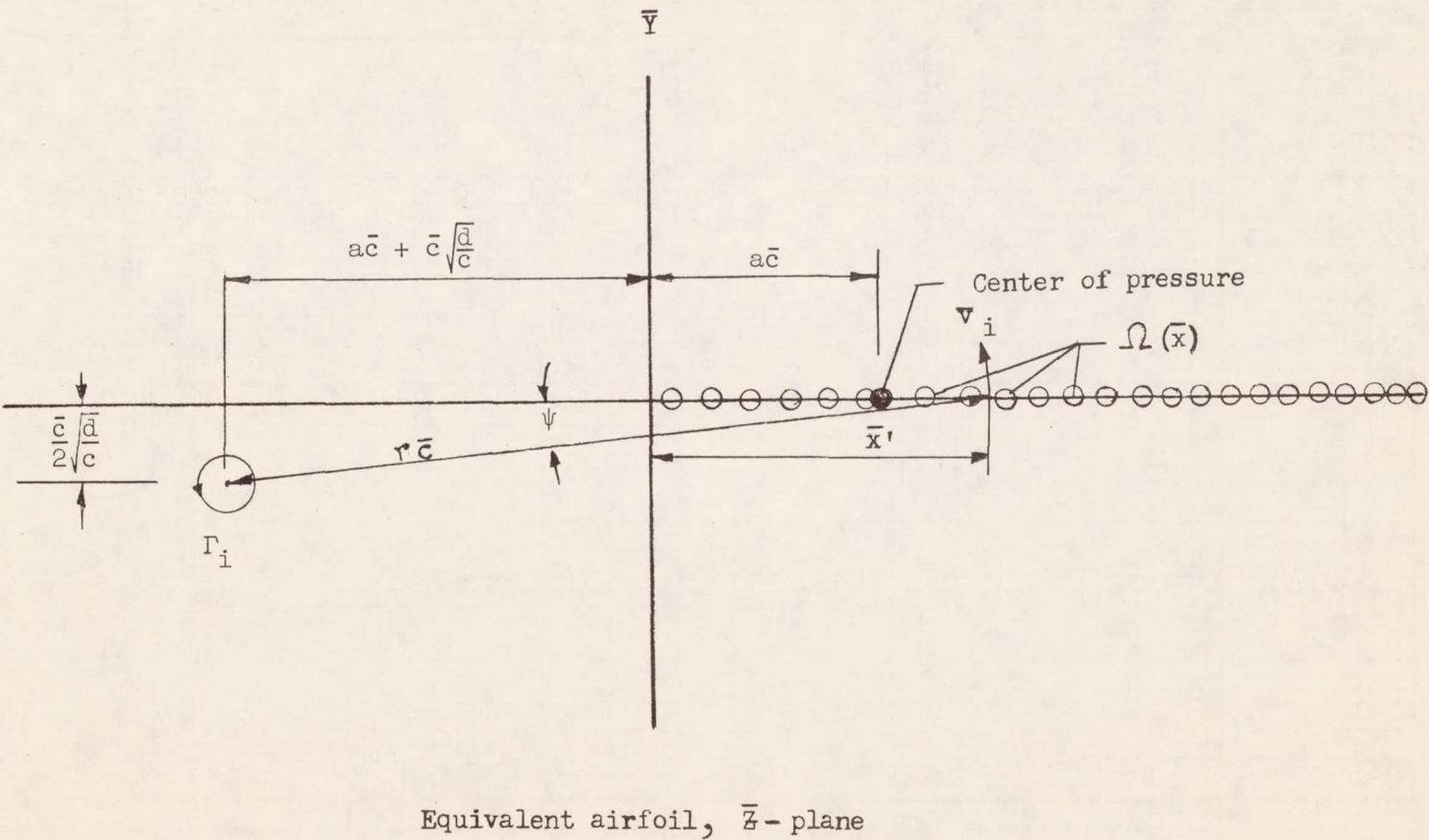


Figure 8.- Linearized model for calculating effect of depth of submersion on vorticity distribution of equivalent airfoil section.

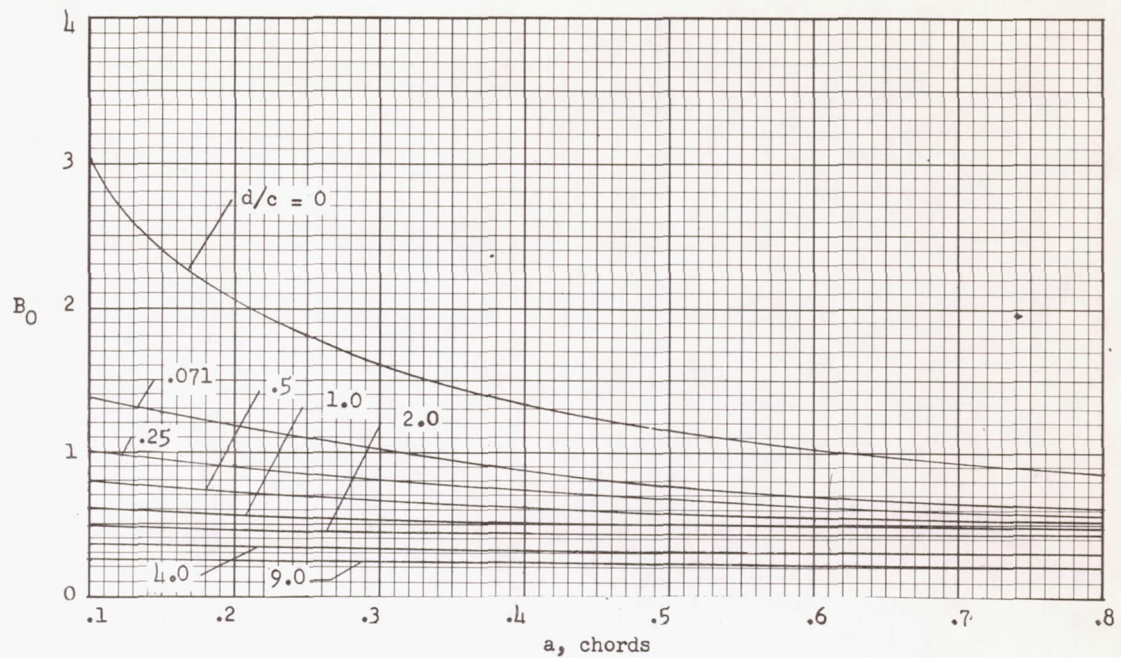
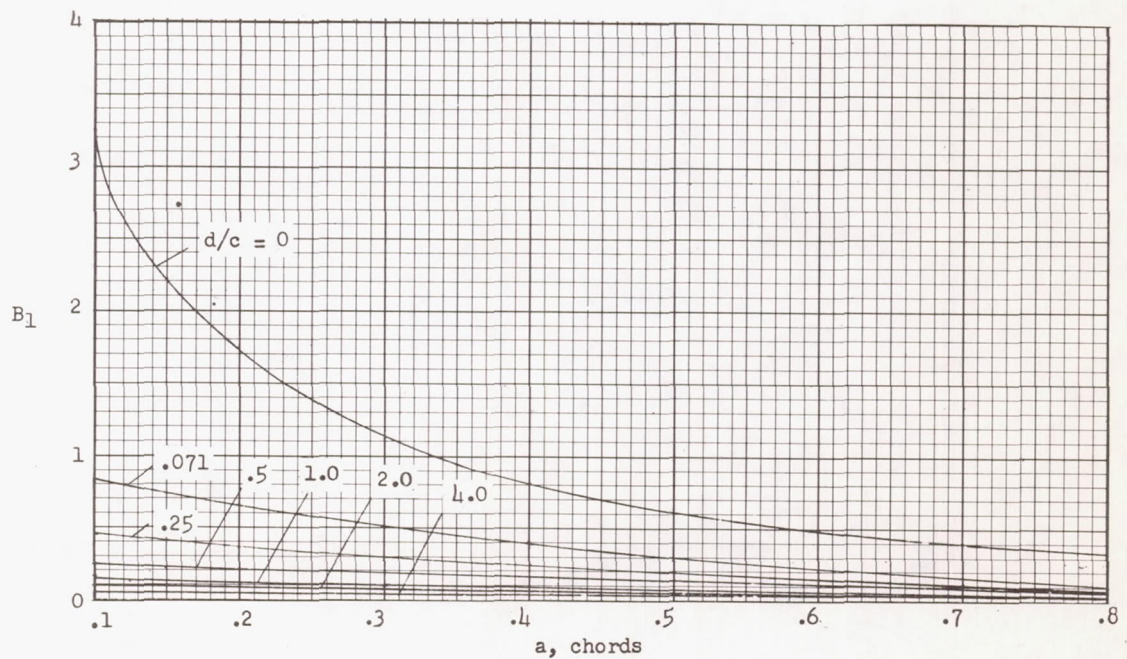
(a) B_0 .(b) B_1 .

Figure 9.- The B coefficients.

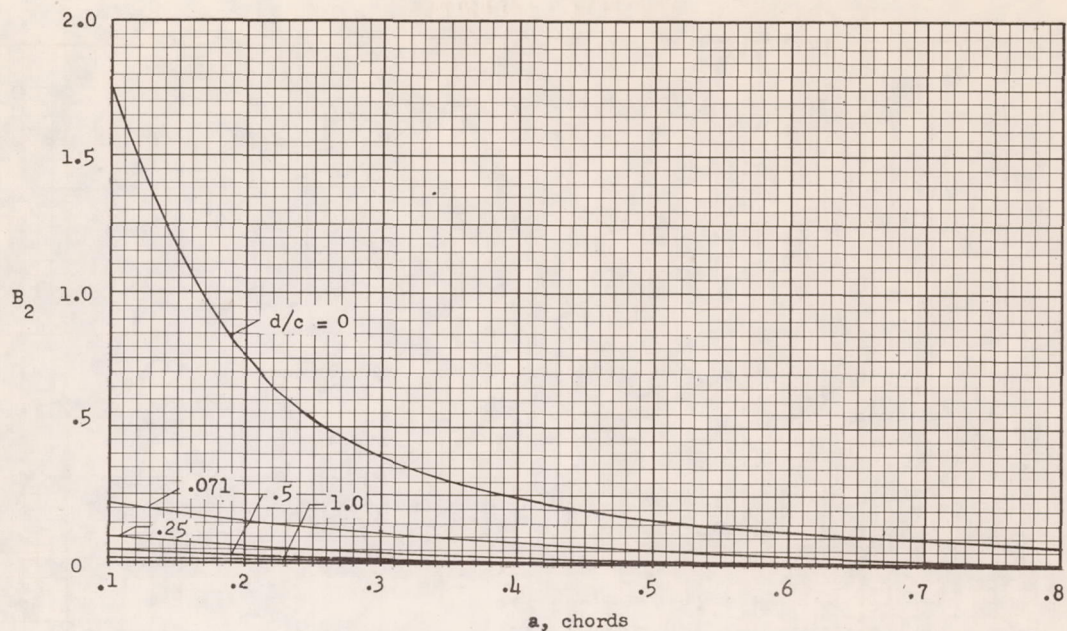
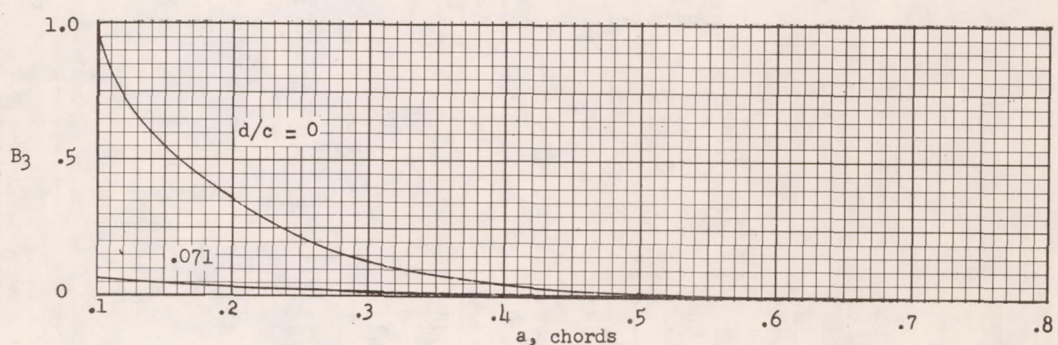
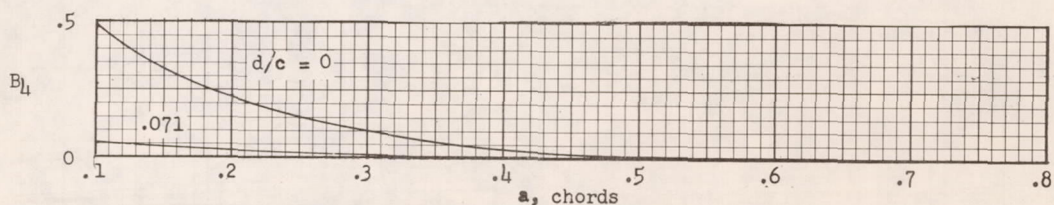
(c) B_2 .(d) B_3 .(e) B_4 .

Figure 9.- Concluded.

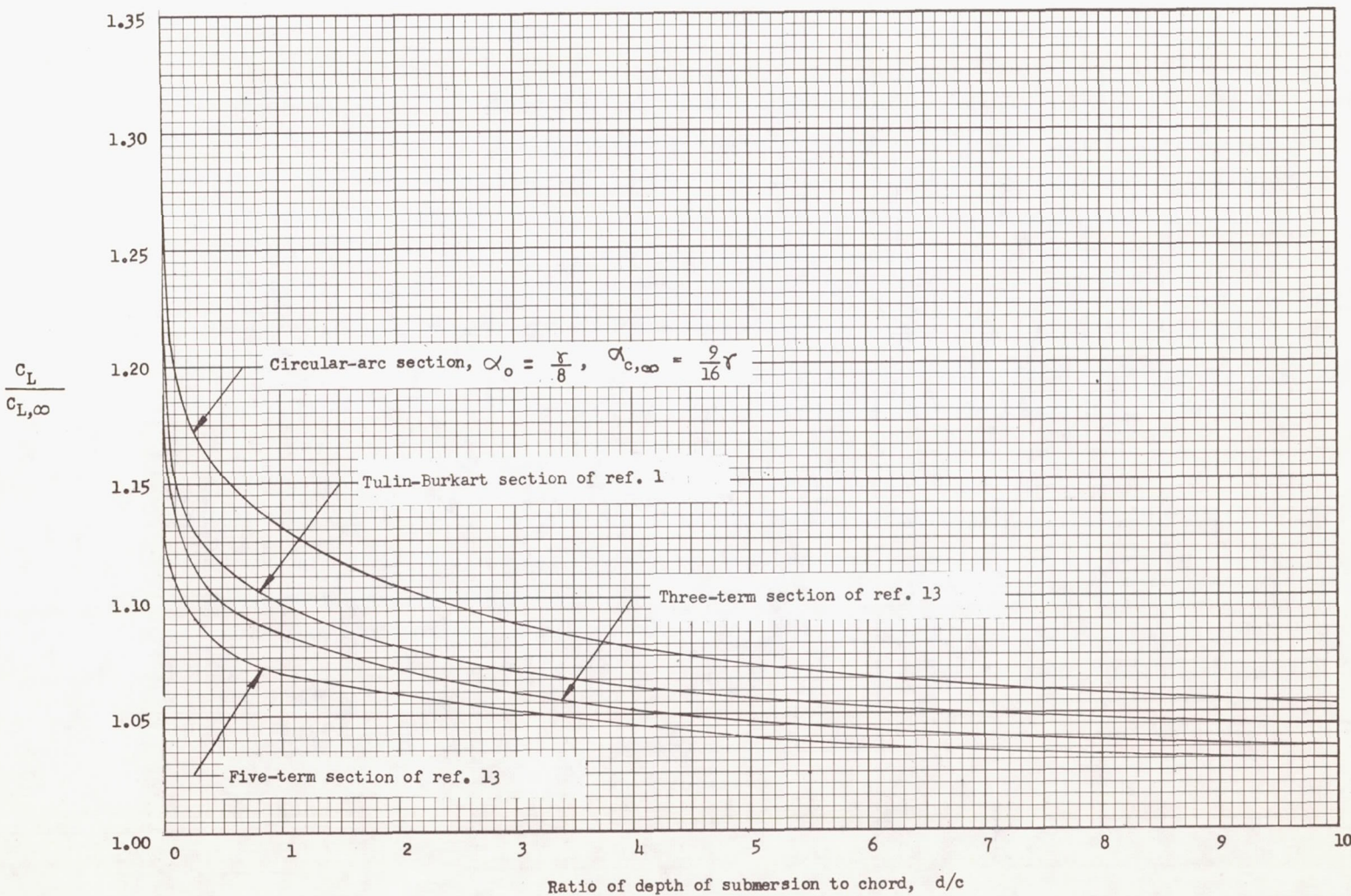


Figure 10.- Influence of depth of submersion on lift coefficient of various cambered sections operating at design angle of attack ($\alpha = 0$).

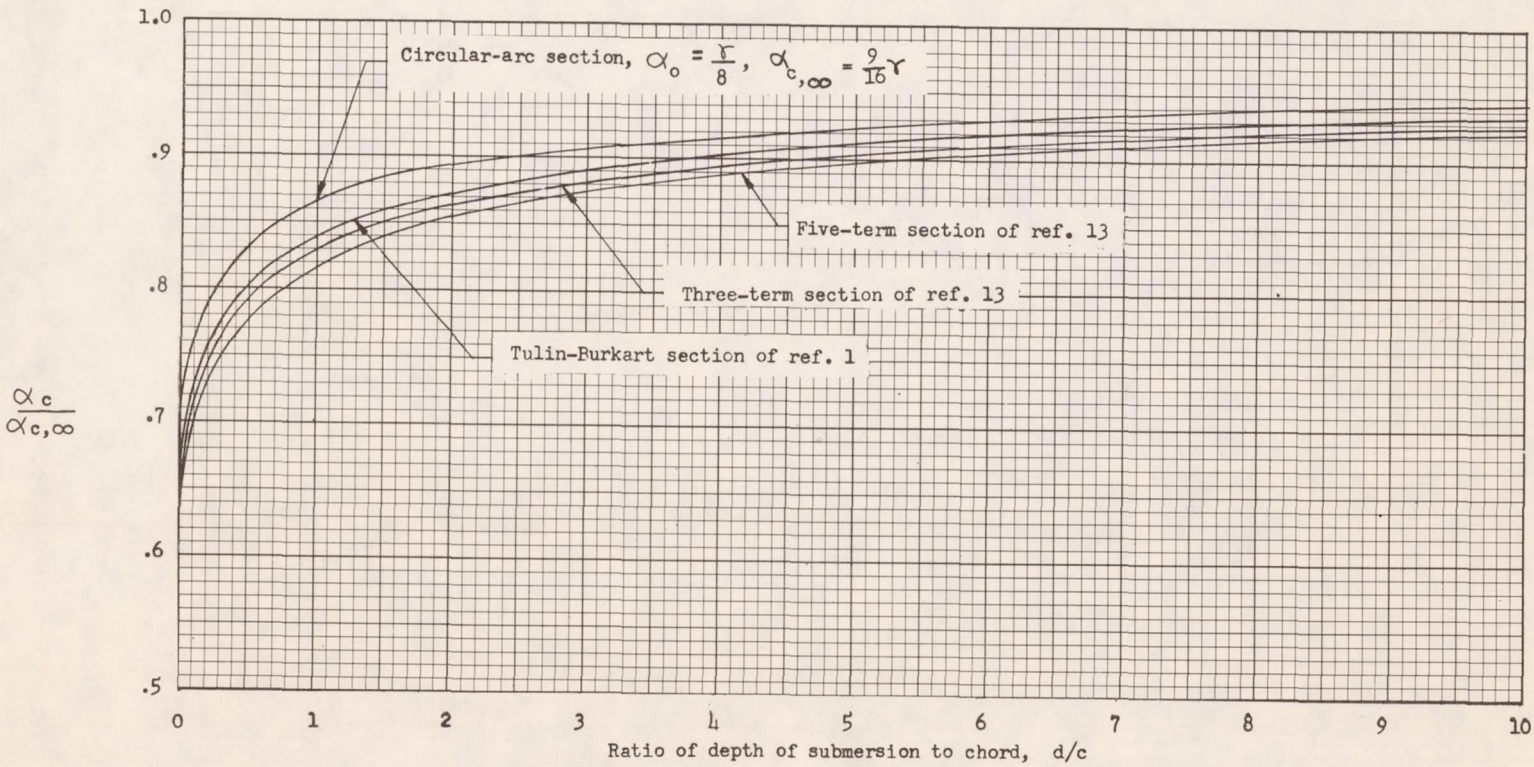


Figure 11.- Influence of depth of submersion on effective angle of attack due to camber α_c of various cambered sections operating at design angle of attack ($\alpha = 0$).

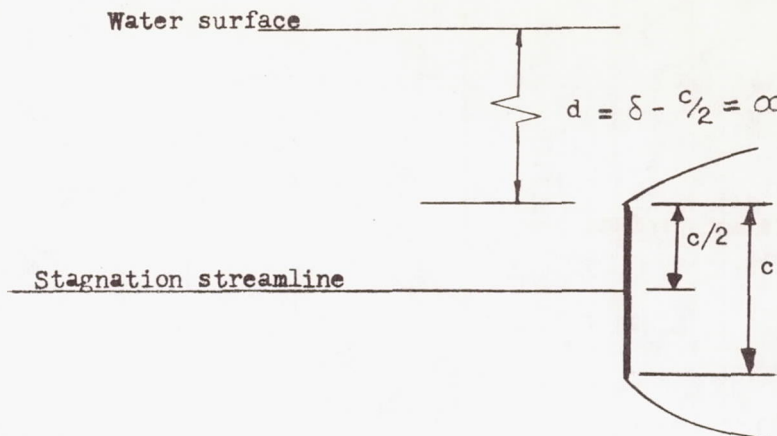
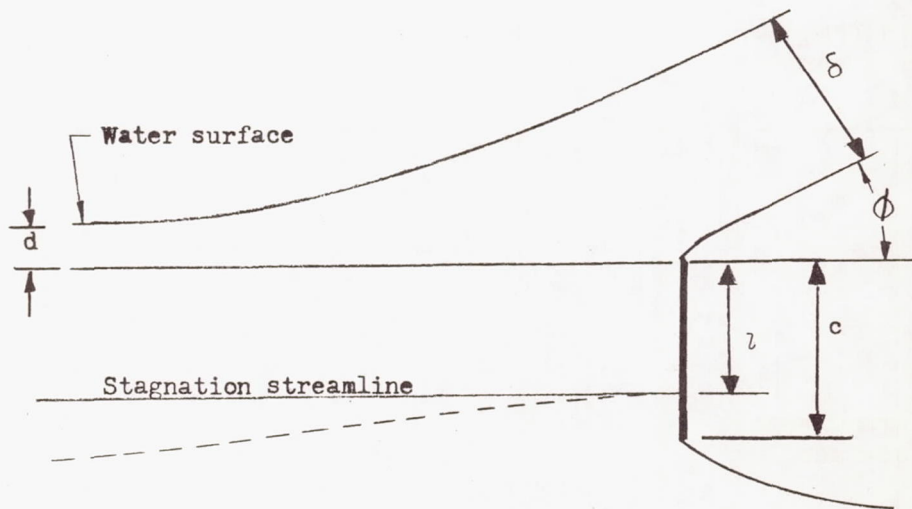
(a) $\delta/c = \infty$.(b) $\delta/c = 0$.(c) $0 < \delta/c < \infty$.

Figure 12.- Location and direction of stagnation line on flat plate normal to direction of motion.

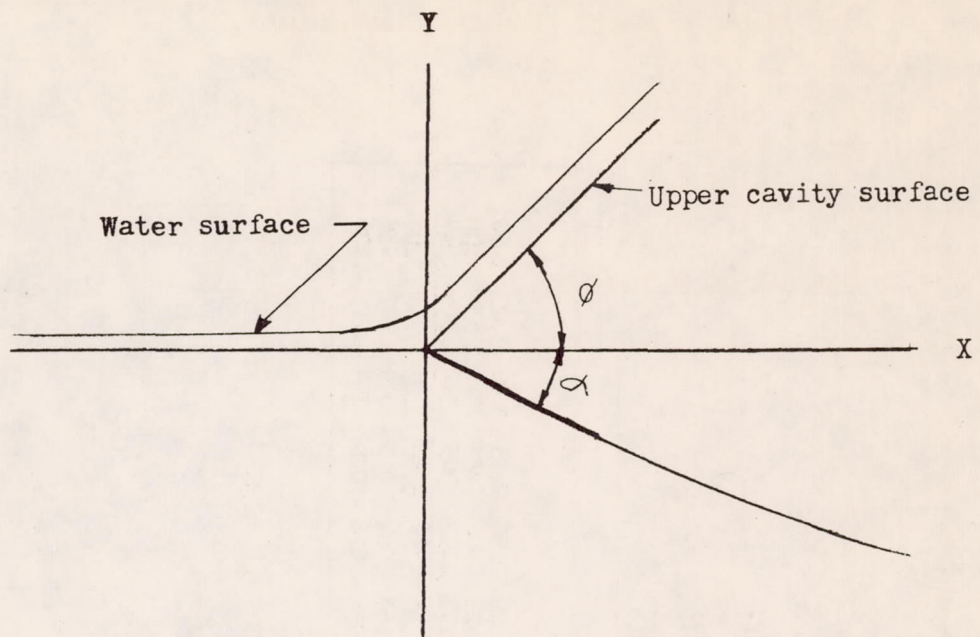
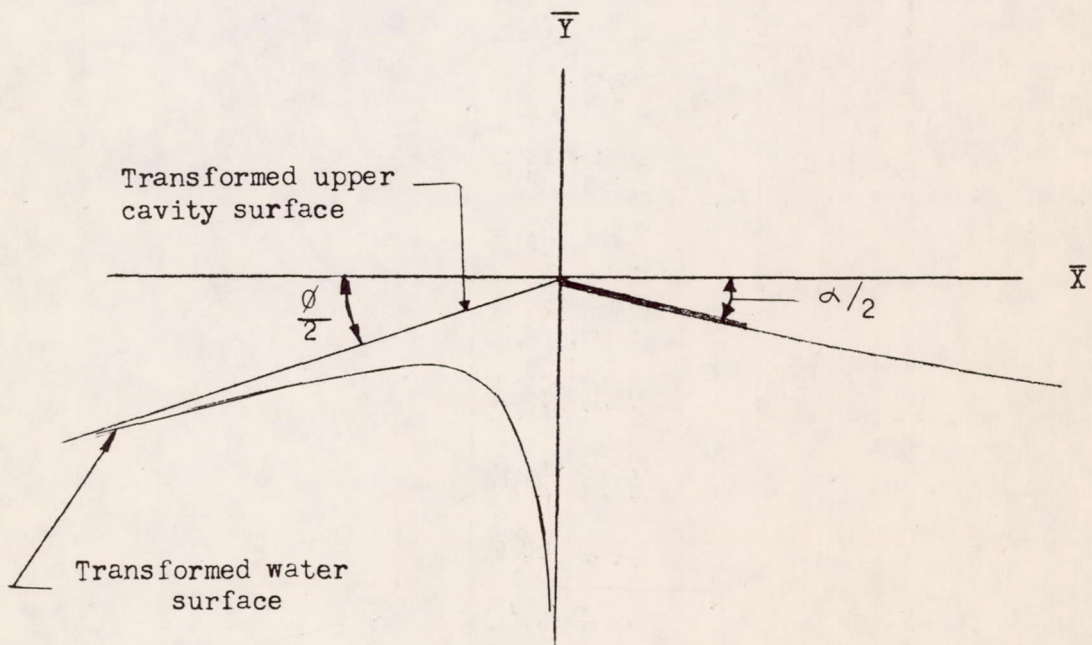
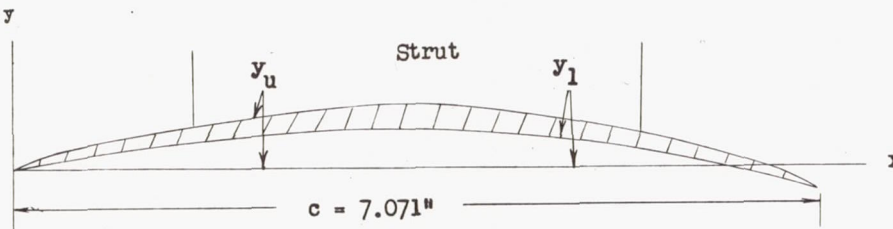
(a) Hydrofoil, Z -plane.(b) Airfoil, $Z = -\sqrt{Z}$ plane.

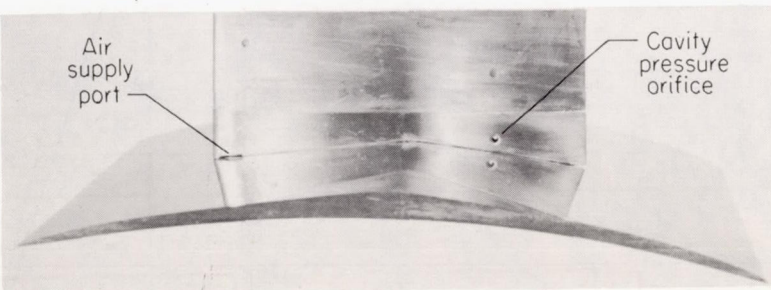
Figure 13.- Hydrofoil and equivalent airfoil at large angles of attack
and small depths of submersion.

$$\frac{y_1}{c} = \frac{A_1}{2} \left[\frac{x}{c} + \frac{8}{3} \left(\frac{x}{c} \right)^{3/2} - 4 \left(\frac{x}{c} \right)^2 \right]$$

$$A_1 = 0.2$$



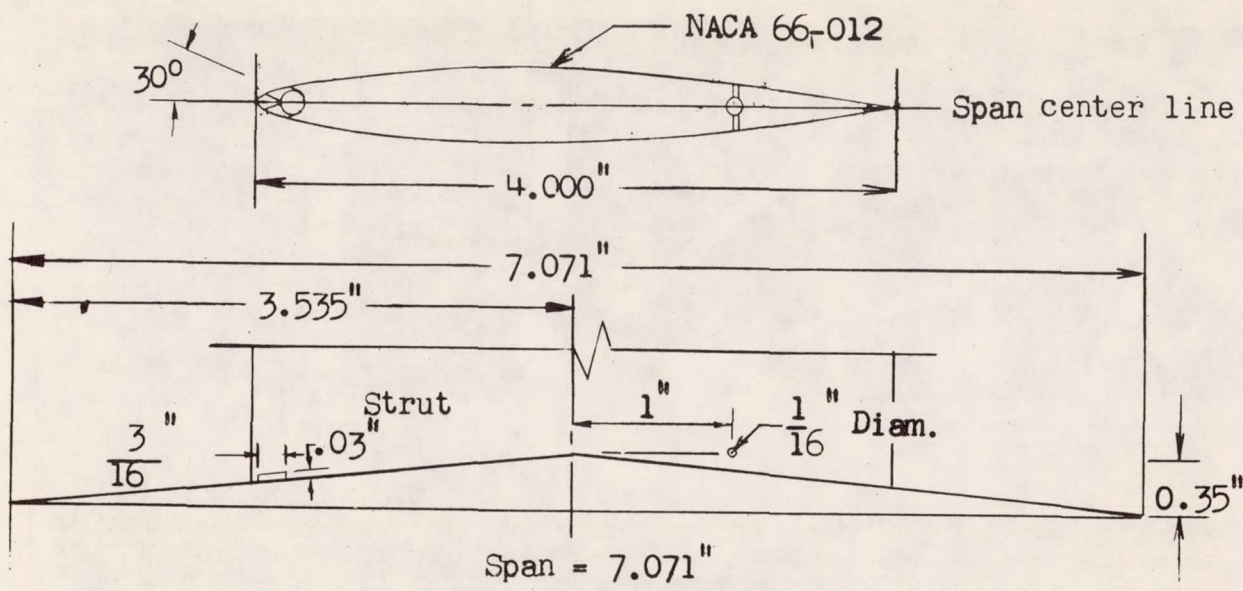
	Coordinates, in.														
x	0	0.25	0.50	0.75	1.00	1.25	1.50	1.75	2.00	2.25	2.50	2.75	3.00	3.25	3.50
y _u	0	.092	.155	.207	.253	.292	.327	.363	.396	.426	.456	.483	.511	.536	.550
y _e	0	.037	.071	.108	.144	.177	.207	.234	.257	.277	.293	.305	.312	.315	.314
x	3.75	4.00	4.25	4.50	4.75	5.00	5.25	5.50	5.75	6.00	6.25	6.50	6.75	7.00	7.071
y _u	.536	.502	.467	.430	.390	.349	.302	.254	.206	.150	.084	.010	-.079	-.189	-.236
y ₁	.308	.297	.282	.262	.237	.207	.172	.132	.088	.038	-.018	-.078	-.144	-.215	-.236



(a) Cambered model.

L-93625.1

Figure 14.- Model configurations.



(b) Flat-plate model.

L-93624.1

Figure 14.- Concluded.

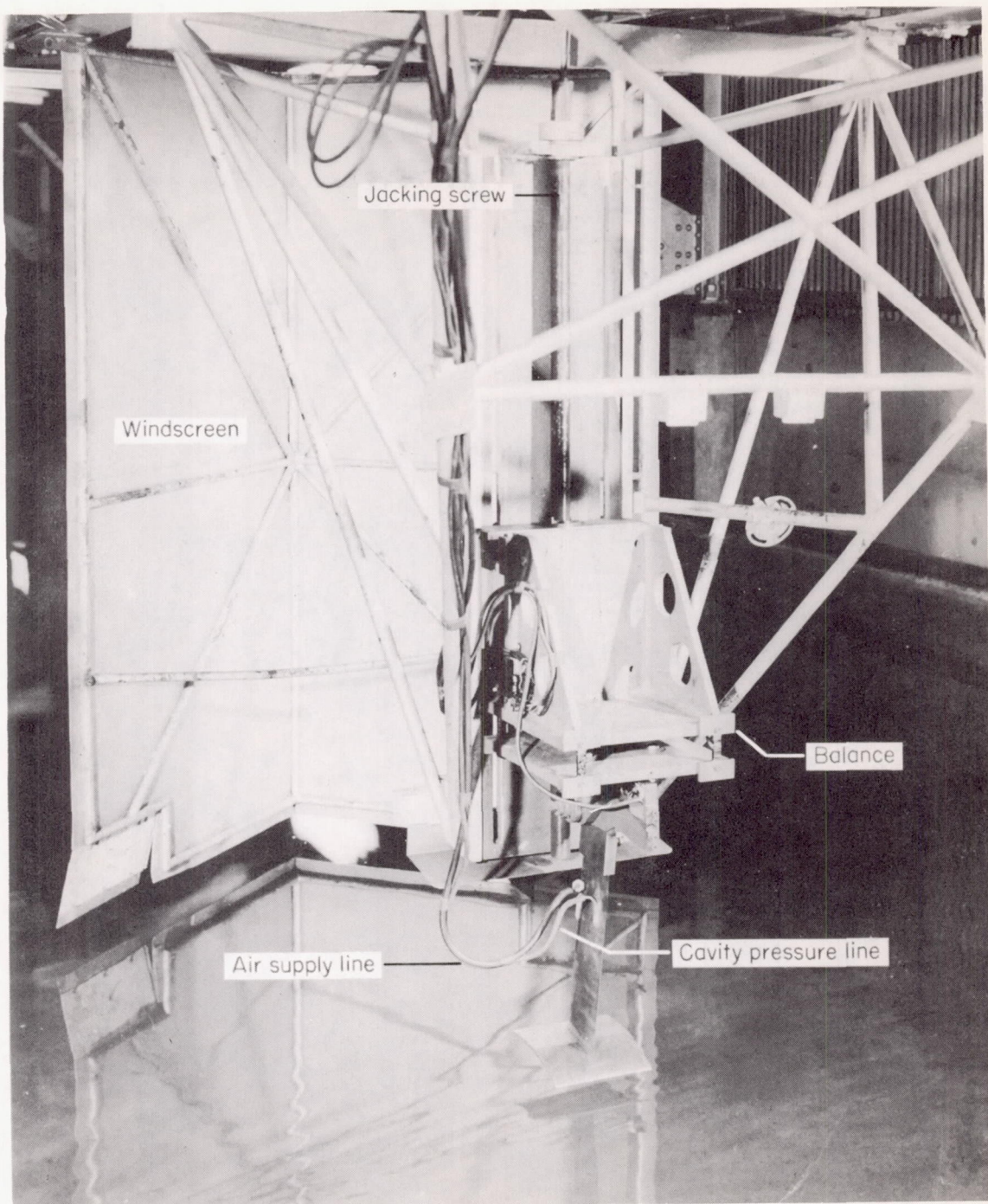


Figure 15.- Test set-up showing cambered hydrofoil with aspect ratio of 1 and balance attached to towing carriage.

L-57-2745

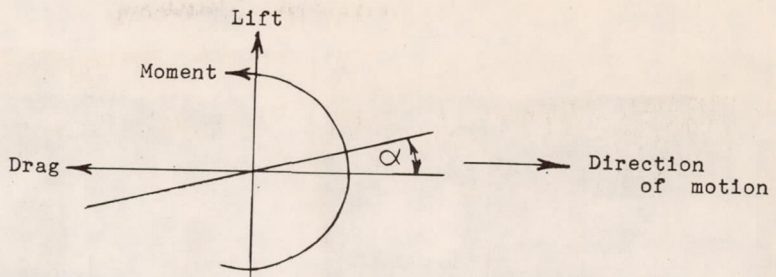
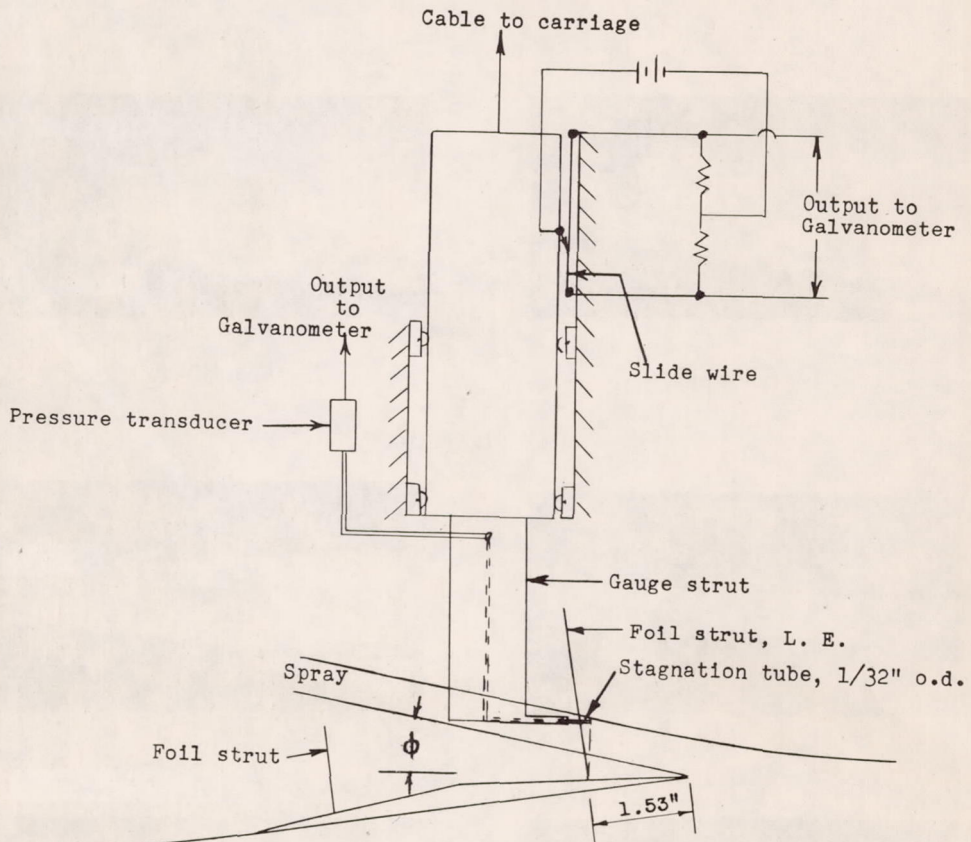
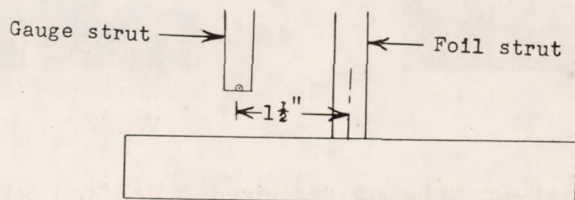


Figure 16.- System of axes.

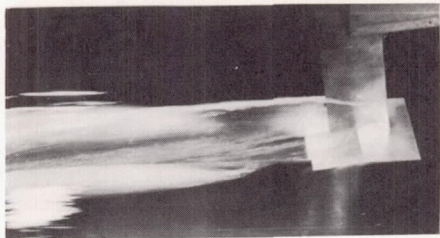
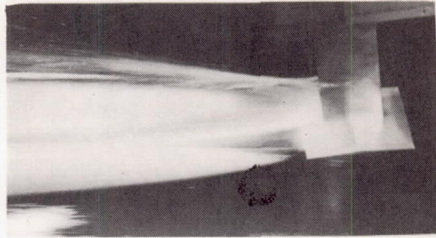
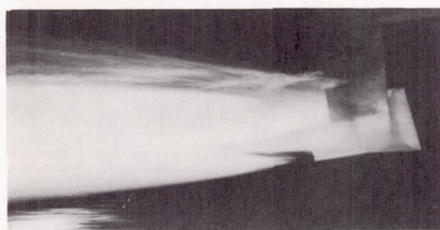
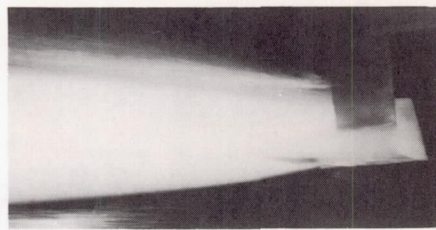
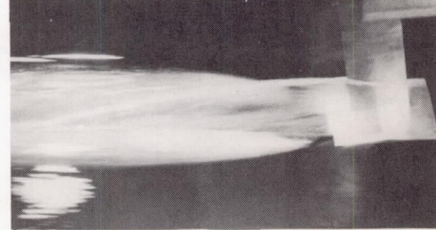
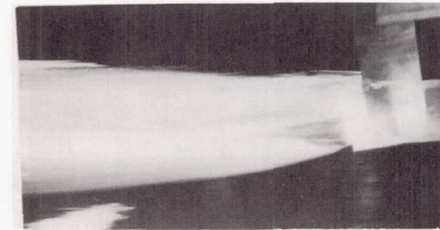
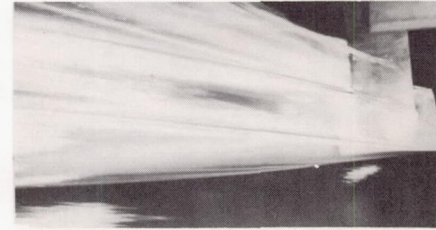


(a) Side elevation.



(b) Front elevation.

Figure 17.- Schematic drawing of spray-thickness gauge.

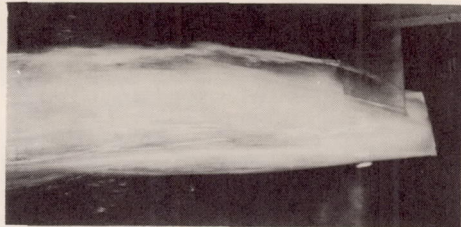
 $V = 20 \text{ fps}$  $V = 40 \text{ fps}$  $V = 60 \text{ fps}$  $V = 80 \text{ fps}$ (a) $\alpha = 80^\circ$. $V = 10 \text{ fps}$  $V = 20 \text{ fps}$  $V = 30 \text{ fps}$  $V = 40 \text{ fps}$ (b) $\alpha = 10^\circ$.

L-57-2740

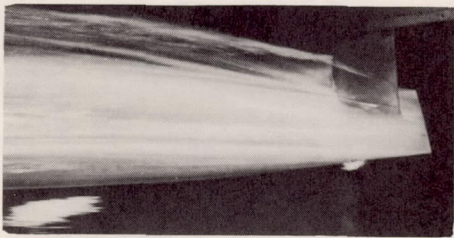
Figure 18.- Flow about the flat lifting surface, depth of submersion is 0.5 inch.



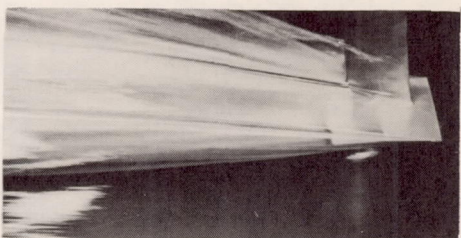
V = 10 fps



V = 20 fps



V = 30 fps



V = 40 fps

(c) $\alpha = 8^\circ$. Air supplied at 0.012 pound per second for $V = 10, 20, 30$ feet per second.

Figure 18.- Concluded.



V = 20 fps



V = 40 fps



V = 60 fps

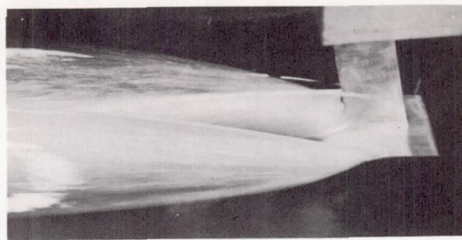


V = 80 fps

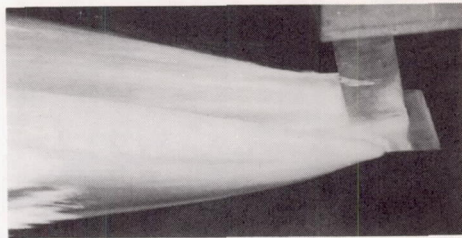
(a) $\alpha = 10^\circ$.

L-57-2741

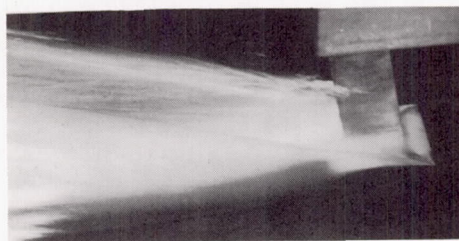
Figure 19.- Flow about cambered lifting surface, depth of submersion is 0.5 inch.



V = 20 fps



V = 40 fps

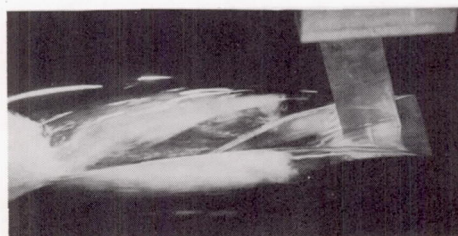


V = 59 fps

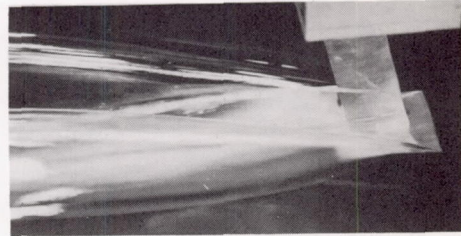


V = 80 fps

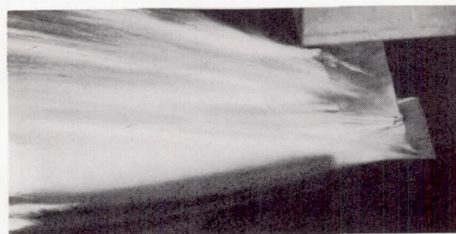
(b) $\alpha = 12^\circ$.



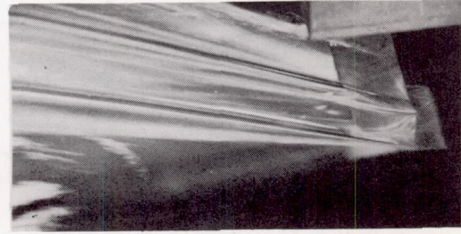
V = 10 fps



V = 20 fps



V = 30 fps



V = 40 fps

(c) $\alpha = 16^\circ$.

L-57-2742

Figure 19.- Concluded.

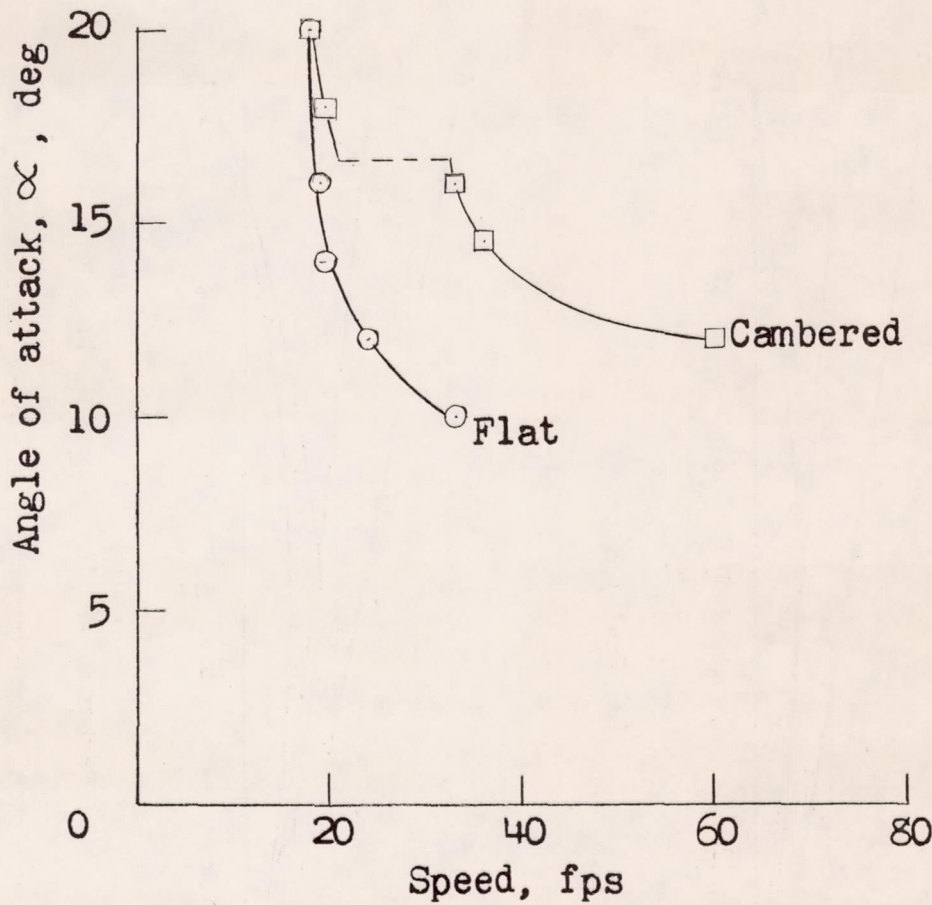
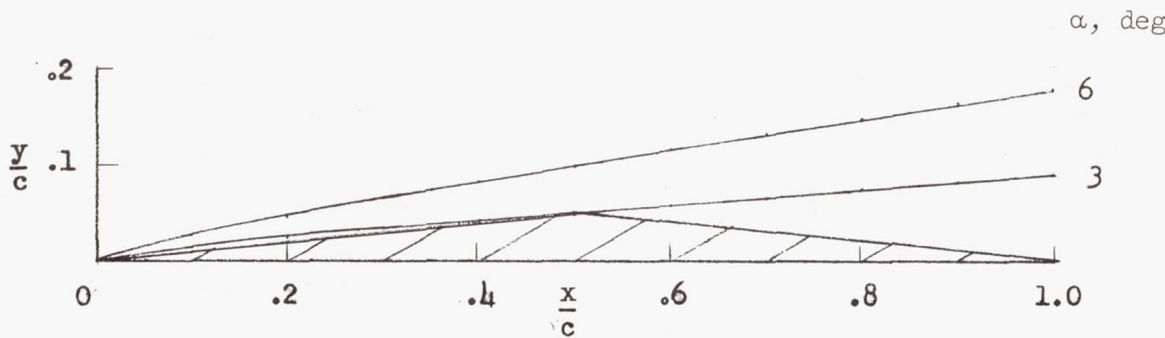


Figure 20.- Vortex ventilation speed for 0.5 inch depth of submersion.



(a) Flat plates.

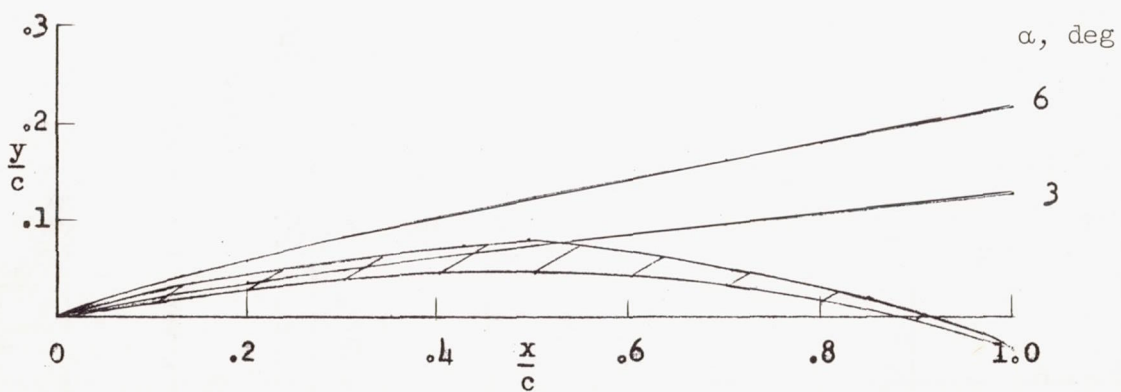
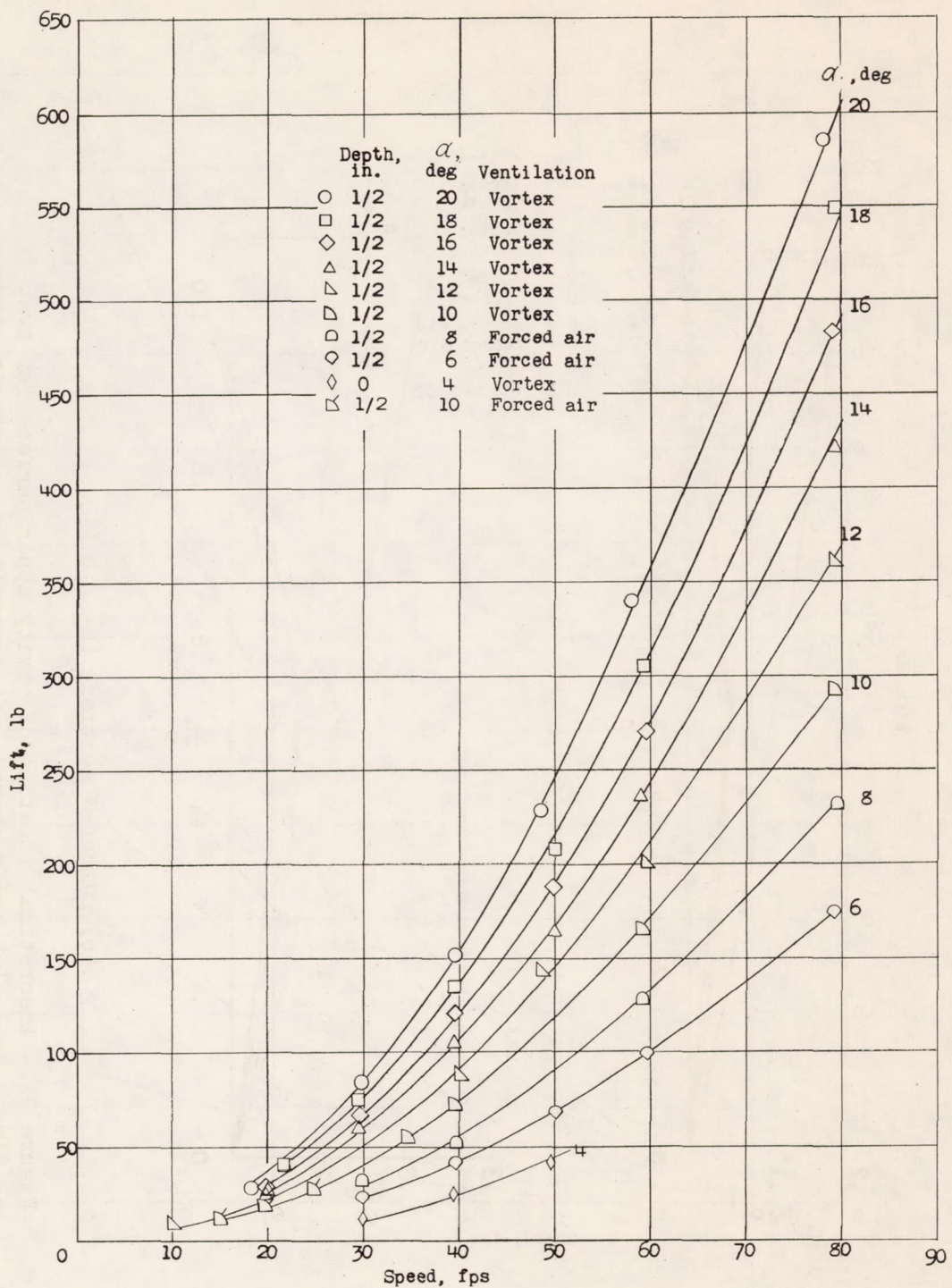
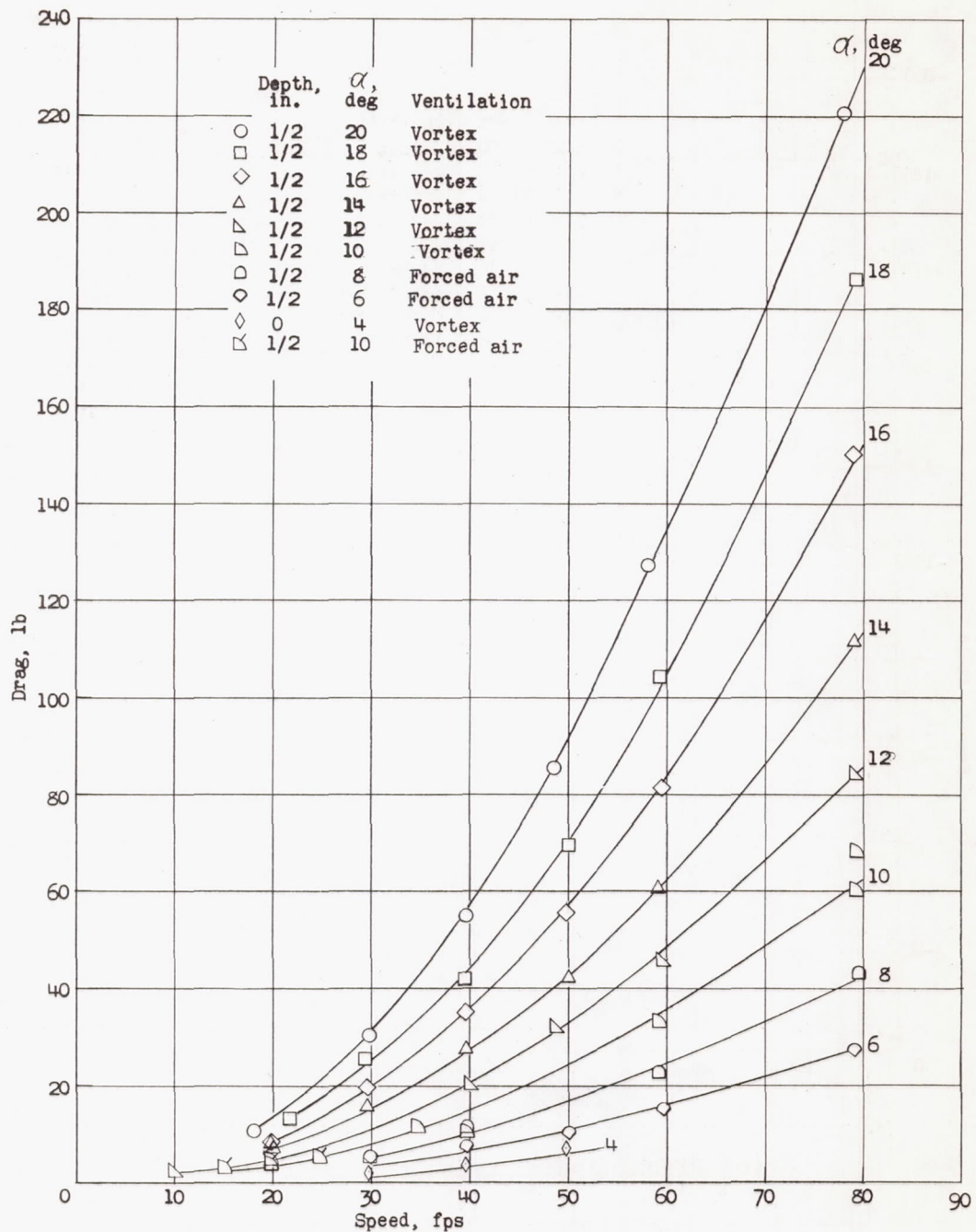
(b) Cambered section, ($A_1 = 0.2$).

Figure 21.- Theoretical location of cavity upper surface for two-dimensional flat and cambered lifting surfaces. (Infinite depth; $\sigma = 0.$)



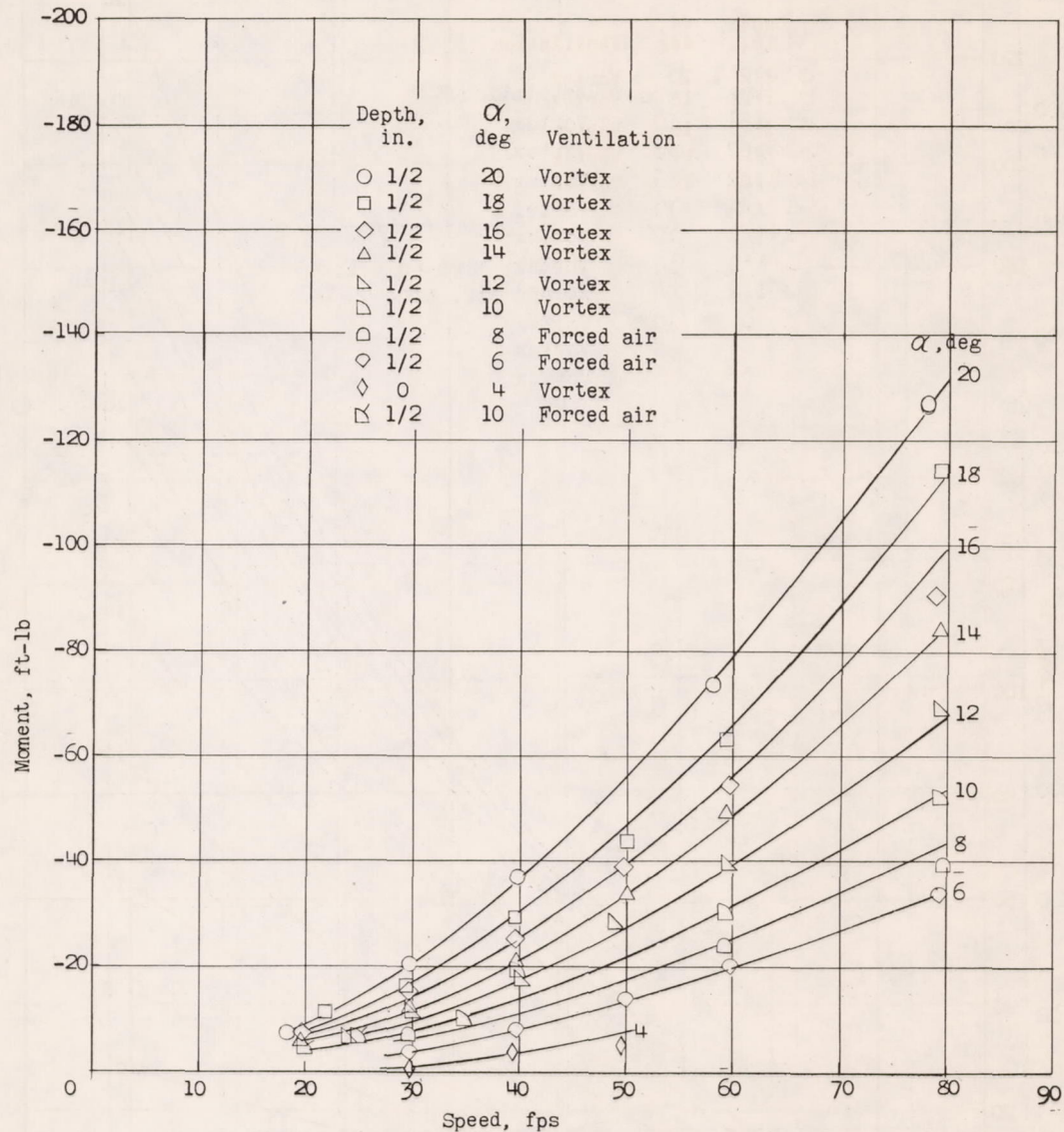
(a) Lift.

Figure 22.- Characteristics of ventilated flat lifting surface.



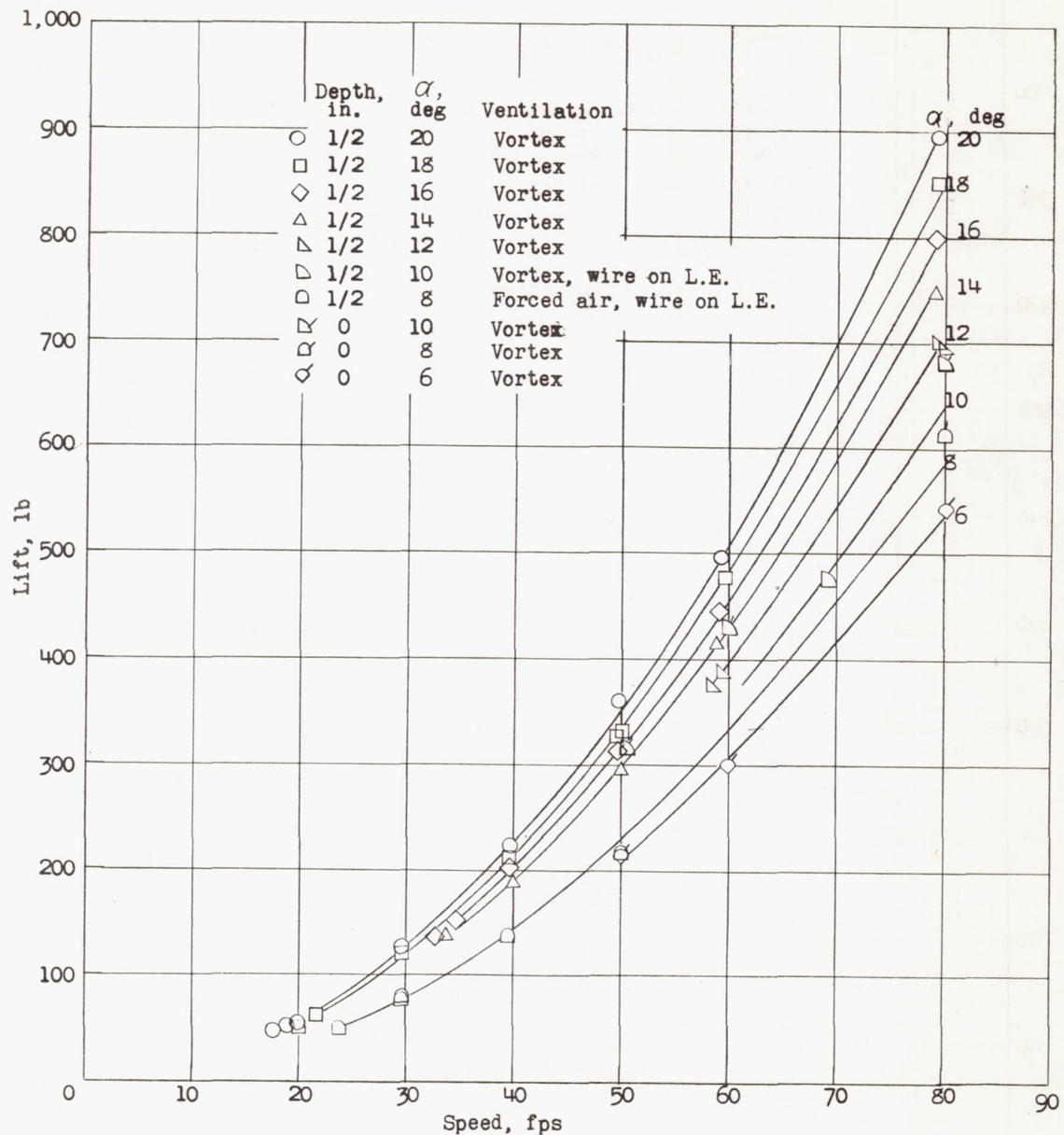
(b) Drag.

Figure 22.- Continued.



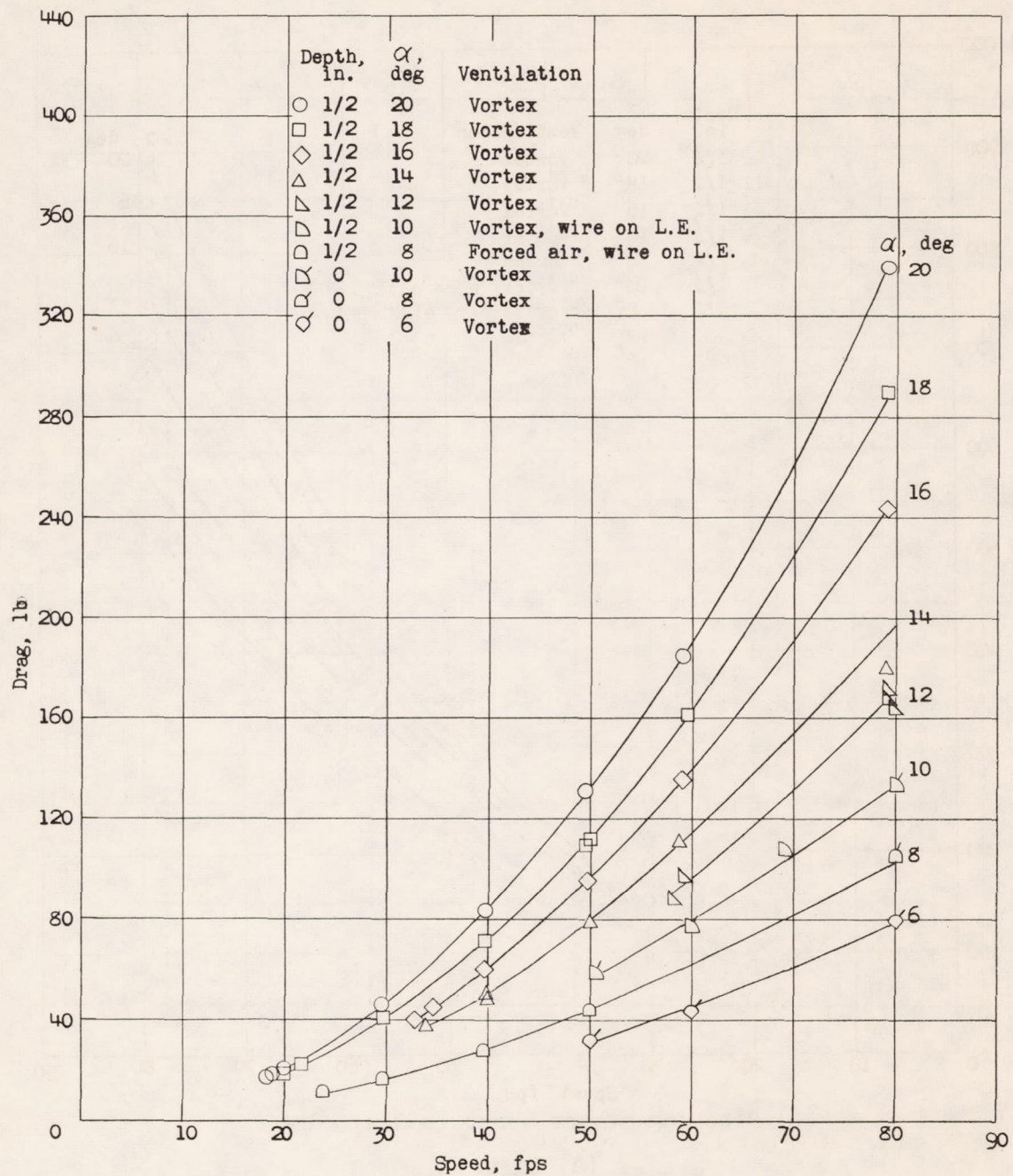
(c) Pitching moment about leading edge.

Figure 22.- Concluded.



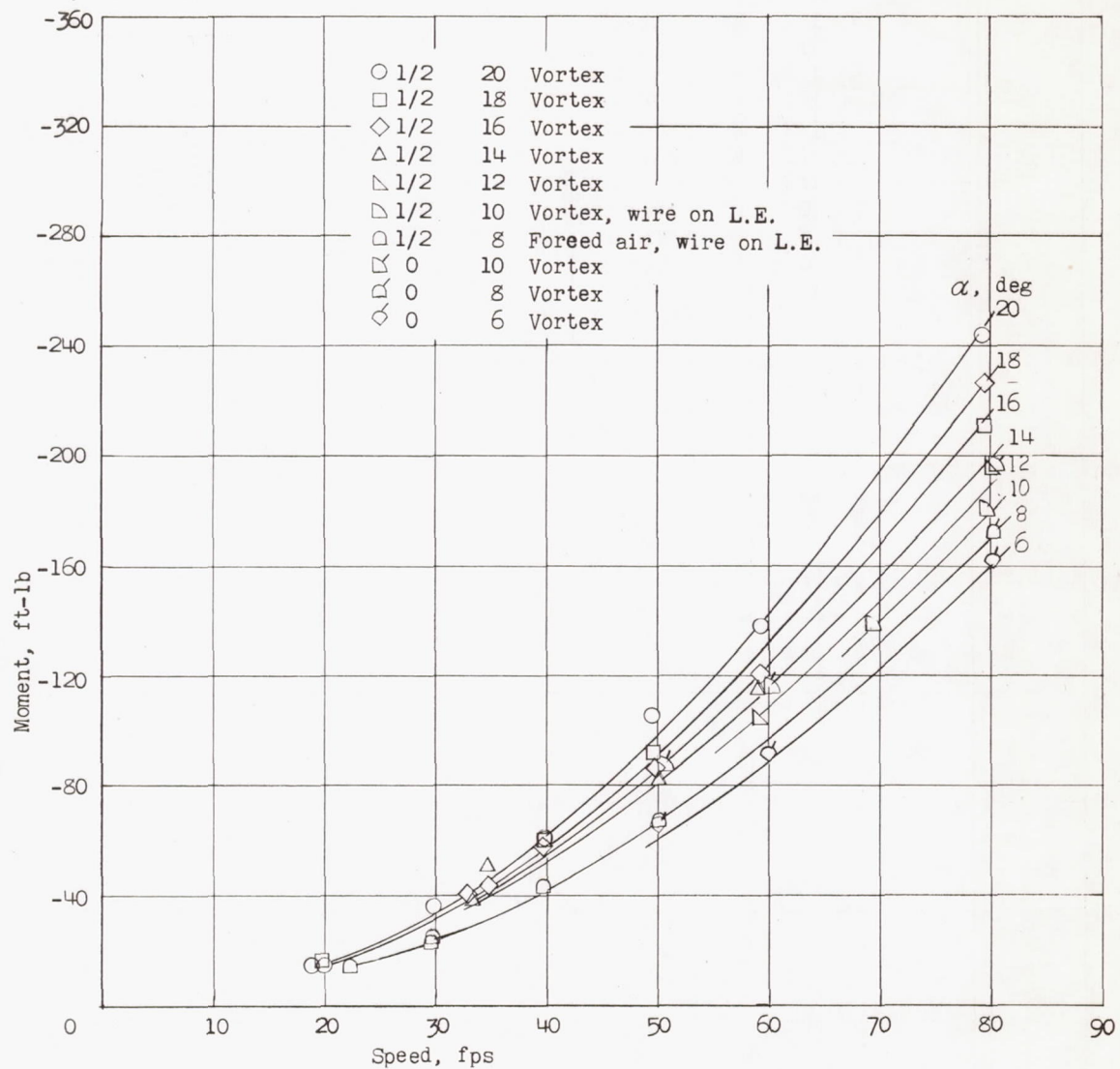
(a) Lift.

Figure 23.- Characteristics of ventilated cambered lifting surface.



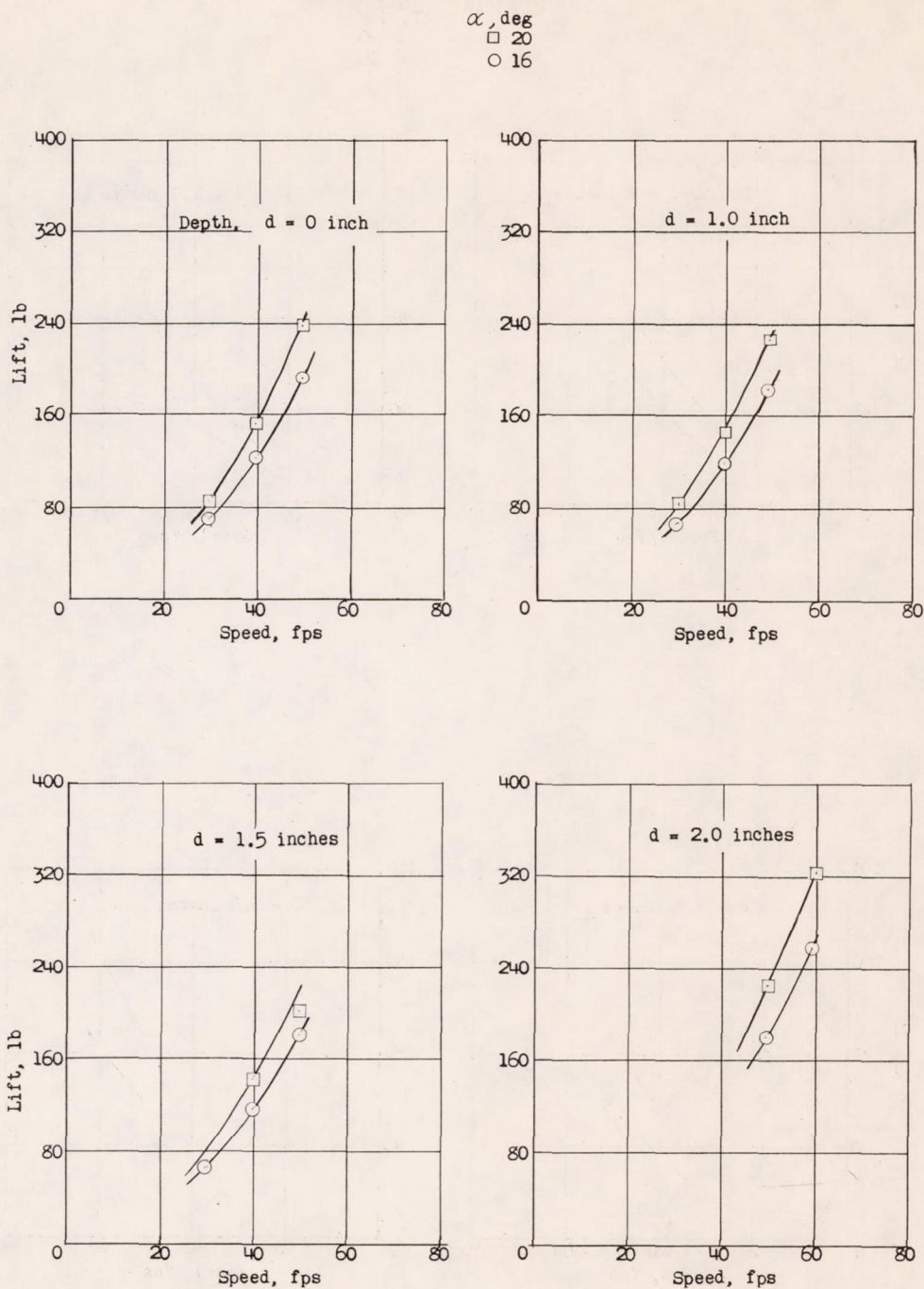
(b) Drag.

Figure 23.- Continued.



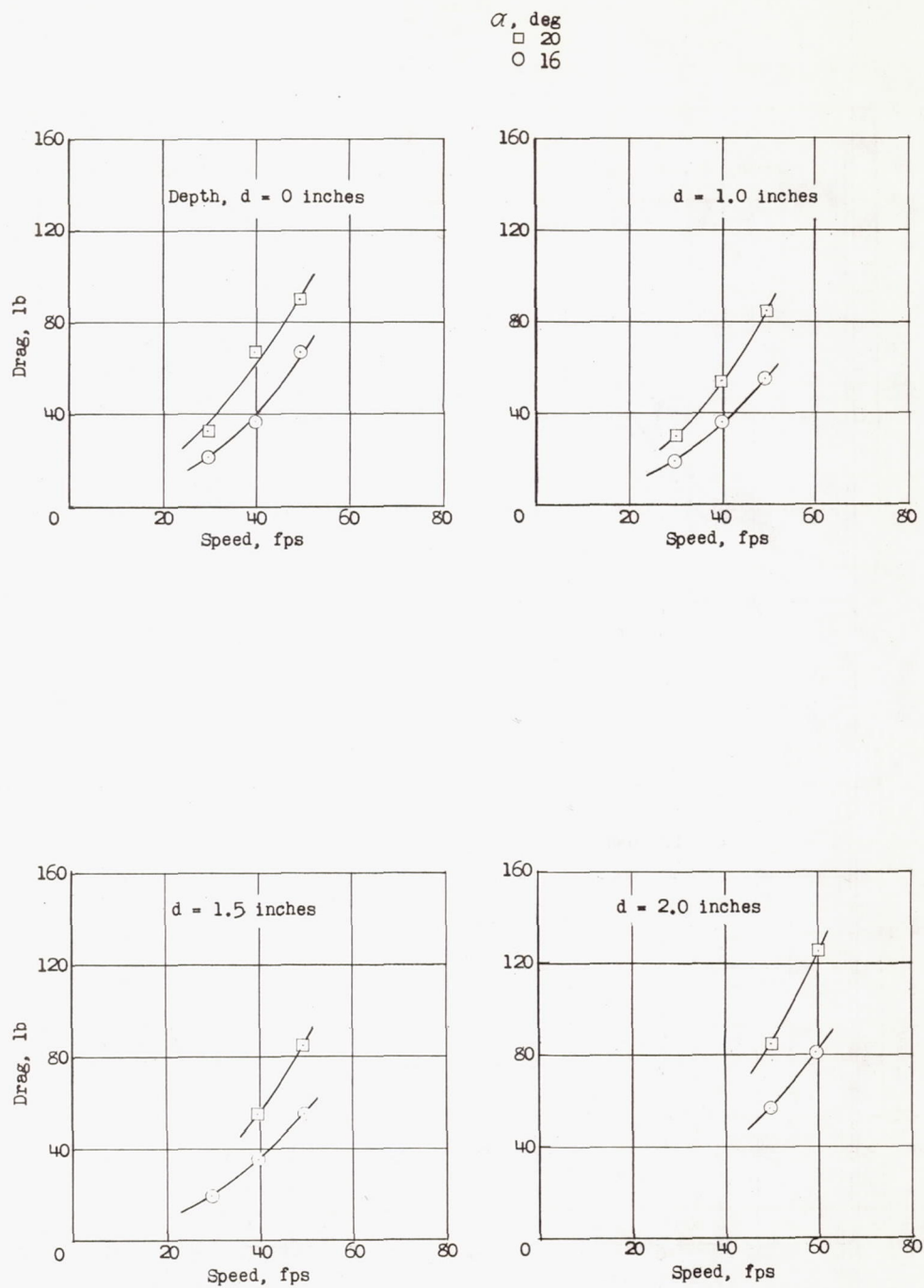
(c) Pitching moment about leading edge.

Figure 23.- Concluded.



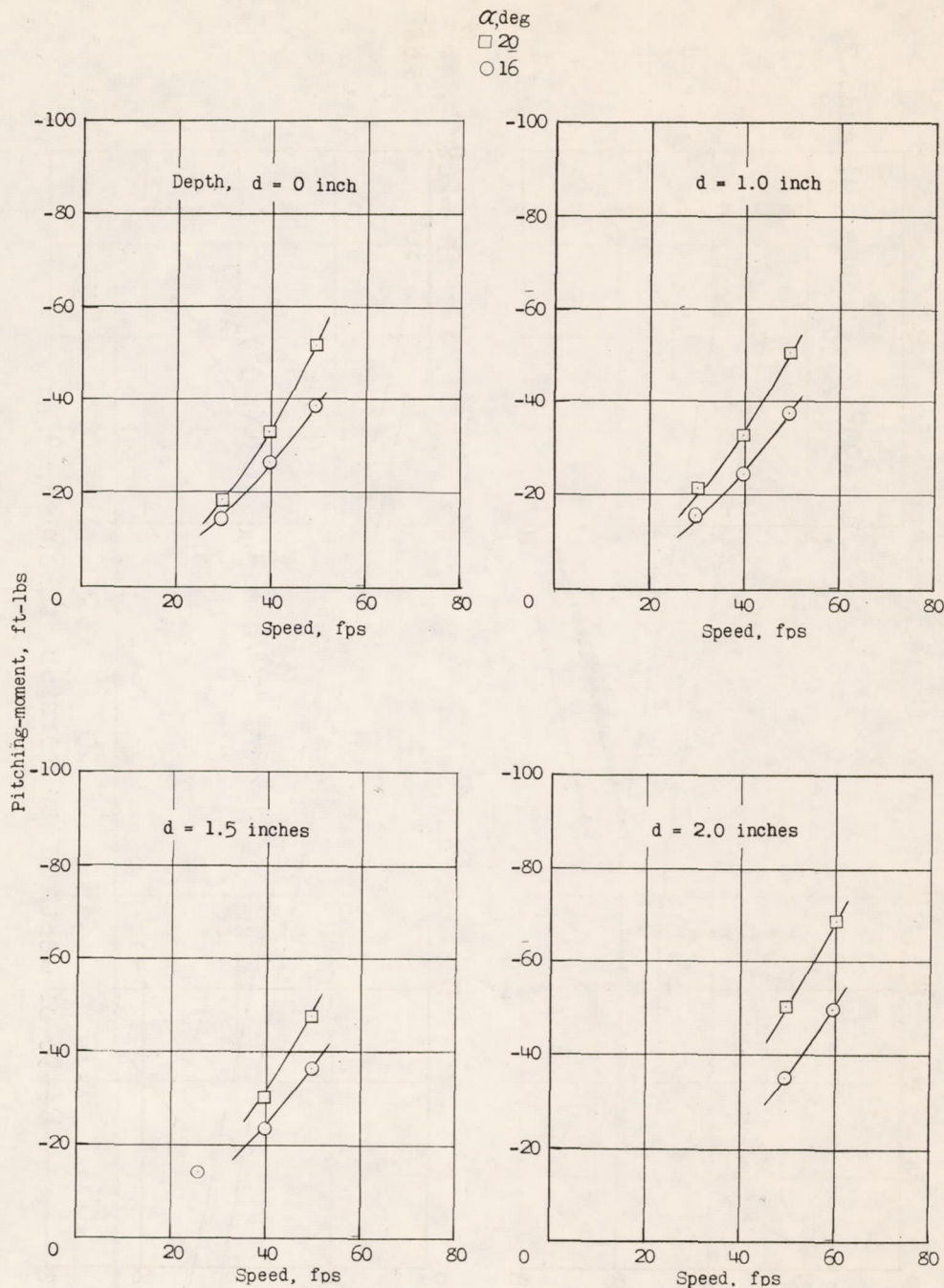
(a) Lift.

Figure 24.- Characteristics of ventilated flat plate at $\alpha = 16^\circ$ and 20° for depths of submersion of 0, 1.0, 1.5, and 2.0 inches.



(b) Drag.

Figure 24.- Continued.



(c) Pitching moment about leading edge.

Figure 24.- Concluded.

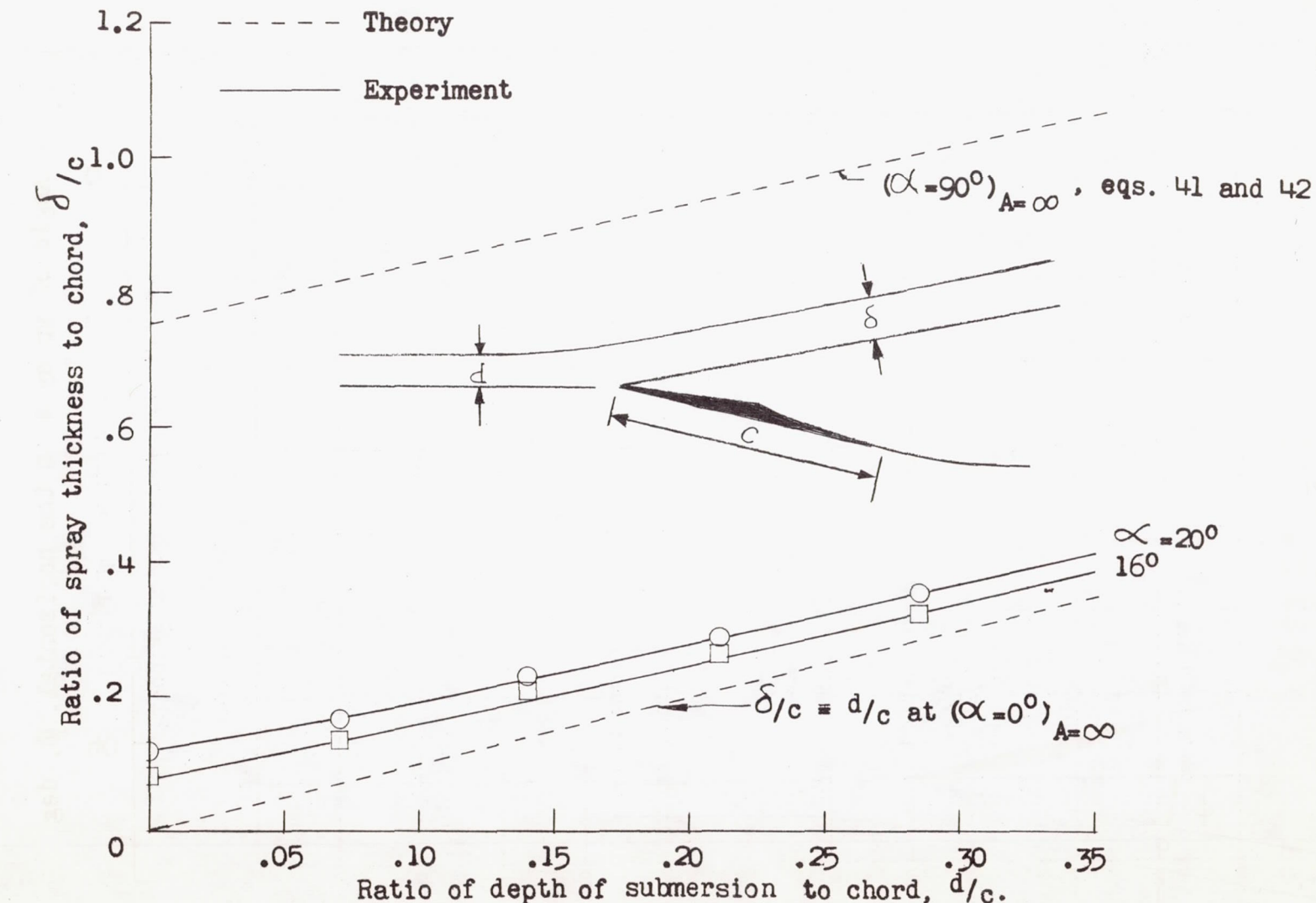


Figure 25.- Effect of depth of submersion on flat lifting surface spray thickness with aspect ratio of 1.

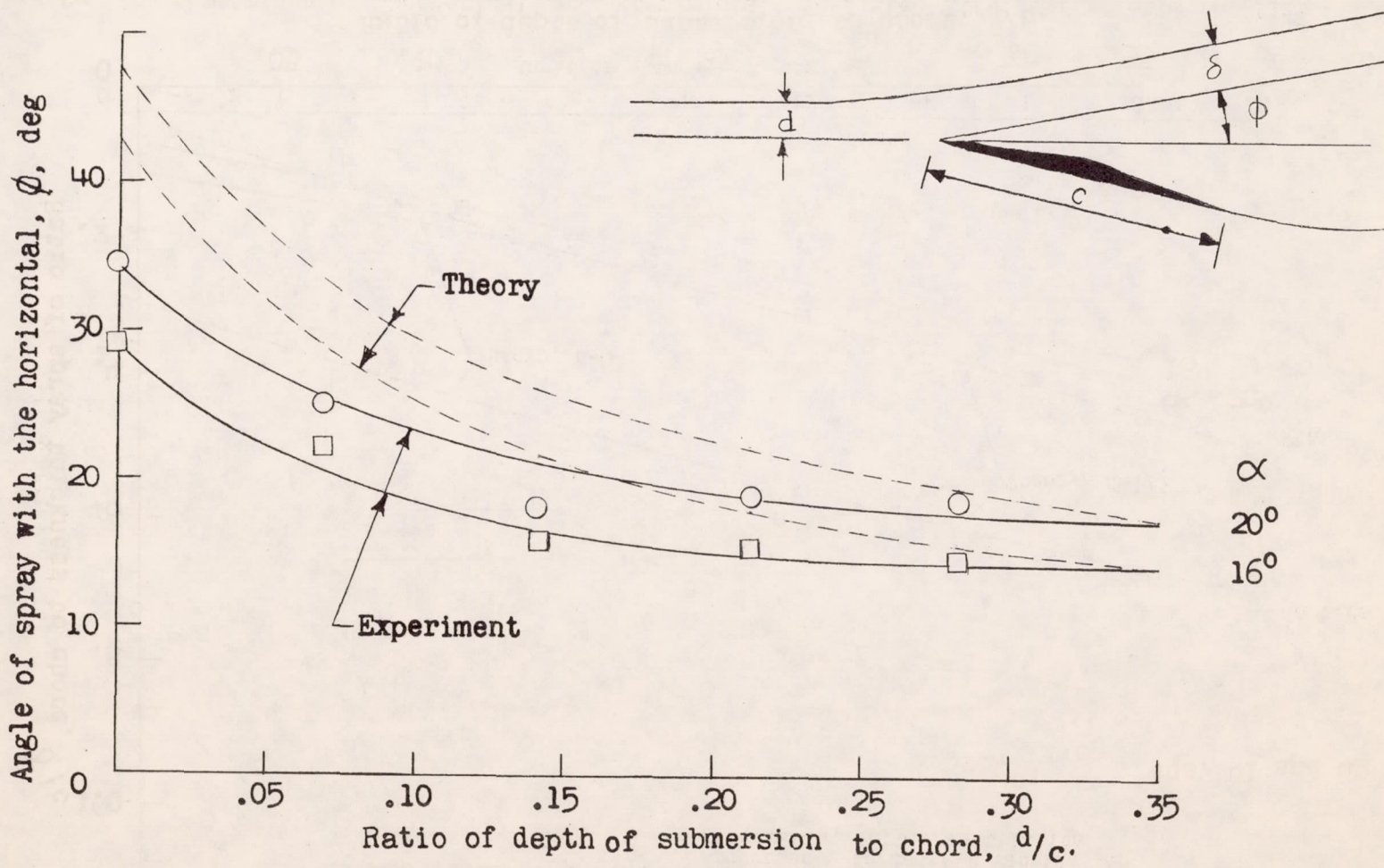


Figure 26.- Effect of depth of submersion on flat lifting surface spray angle with aspect ratio of 1.

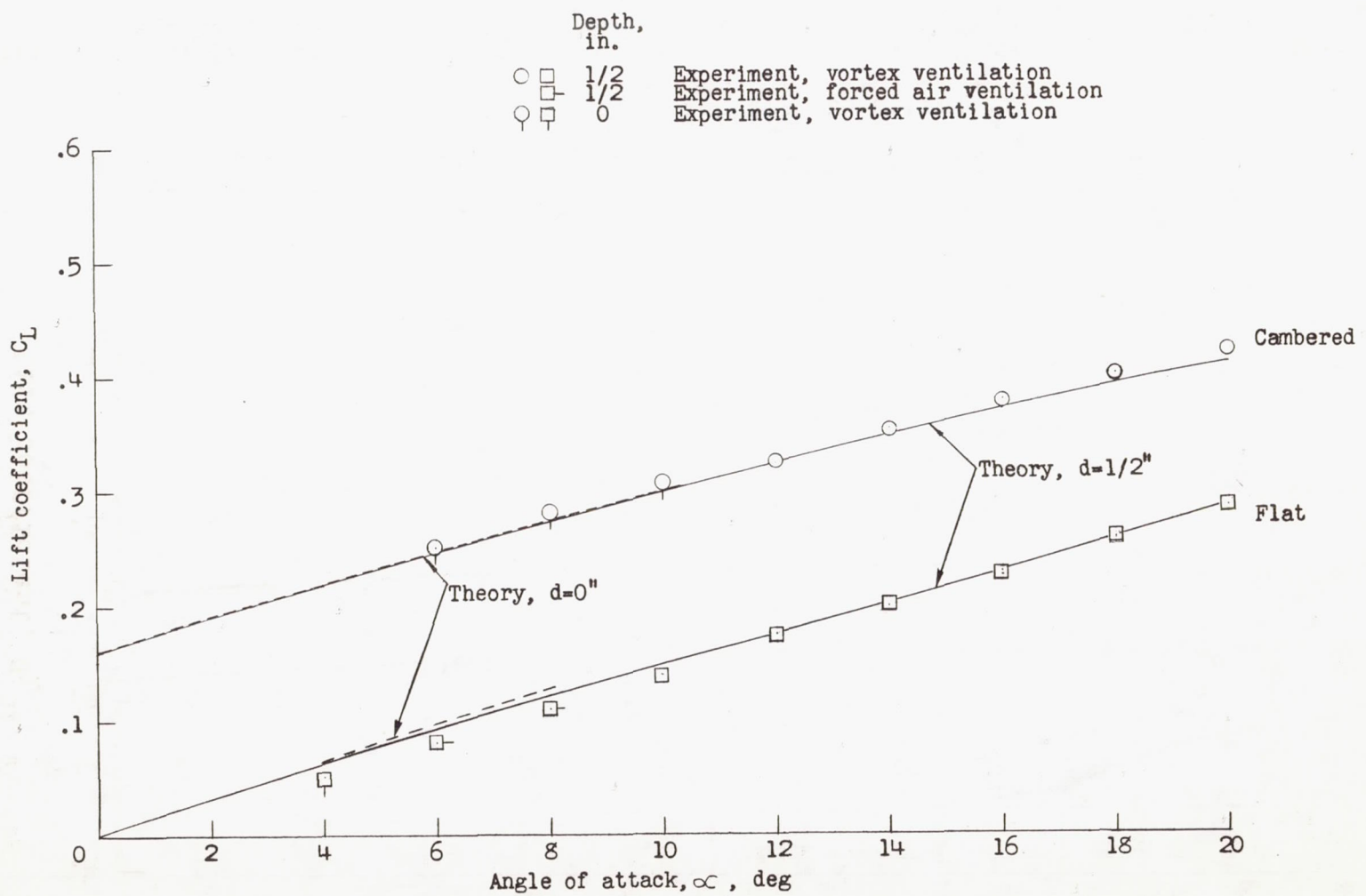


Figure 27.- Comparison of theoretical and experimental ventilated lift coefficients for flat and cambered lifting surfaces with aspect ratio of 1.

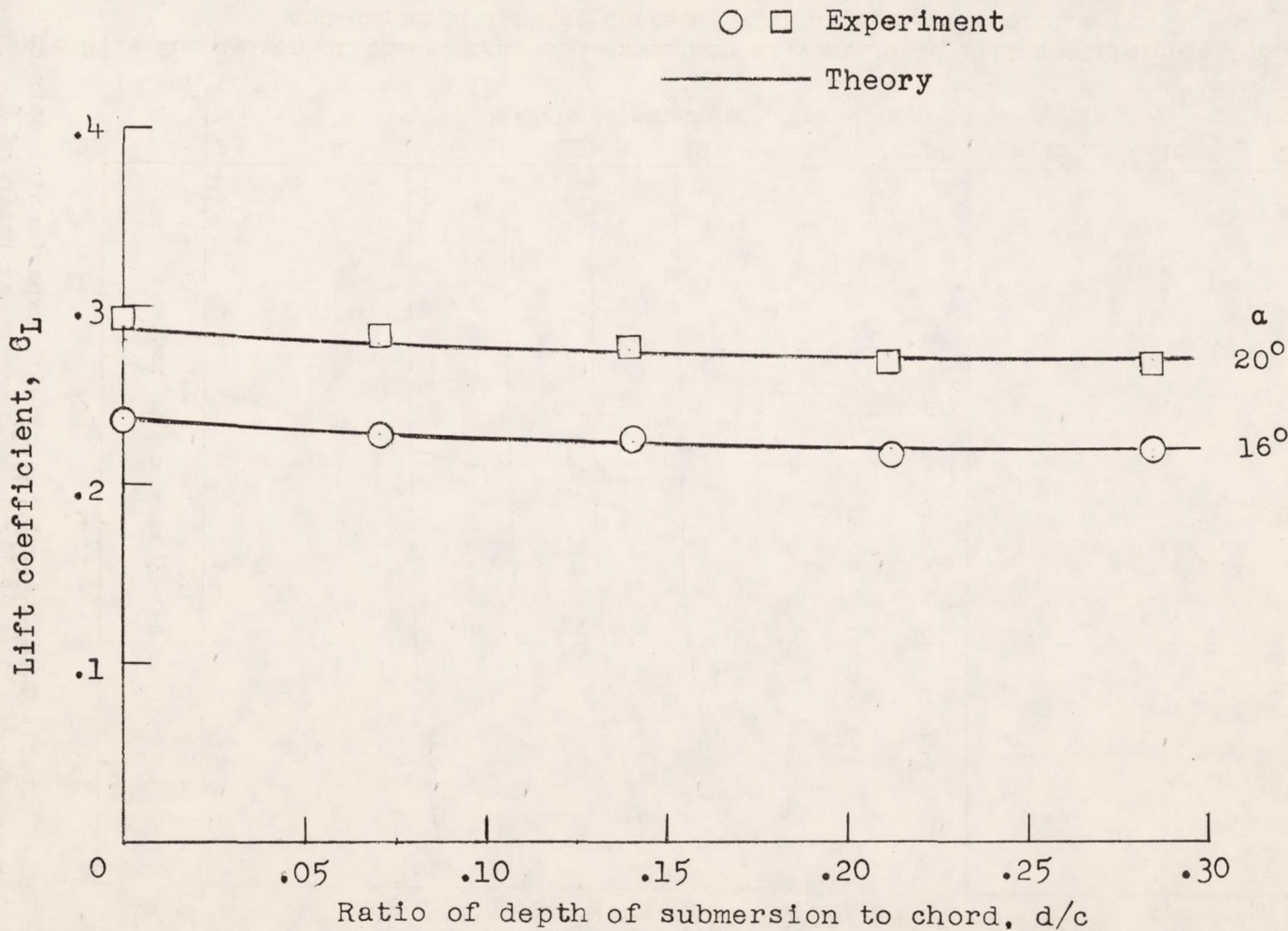
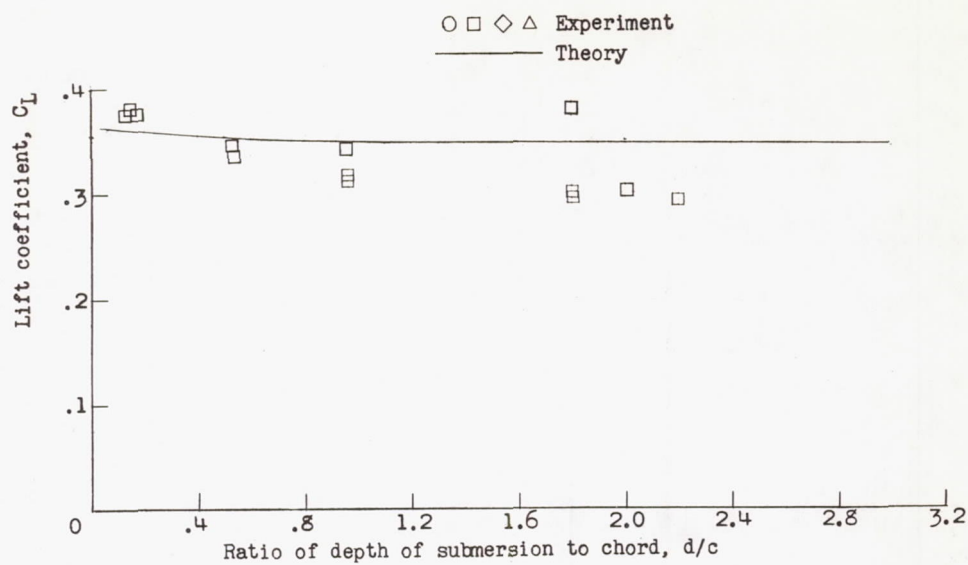
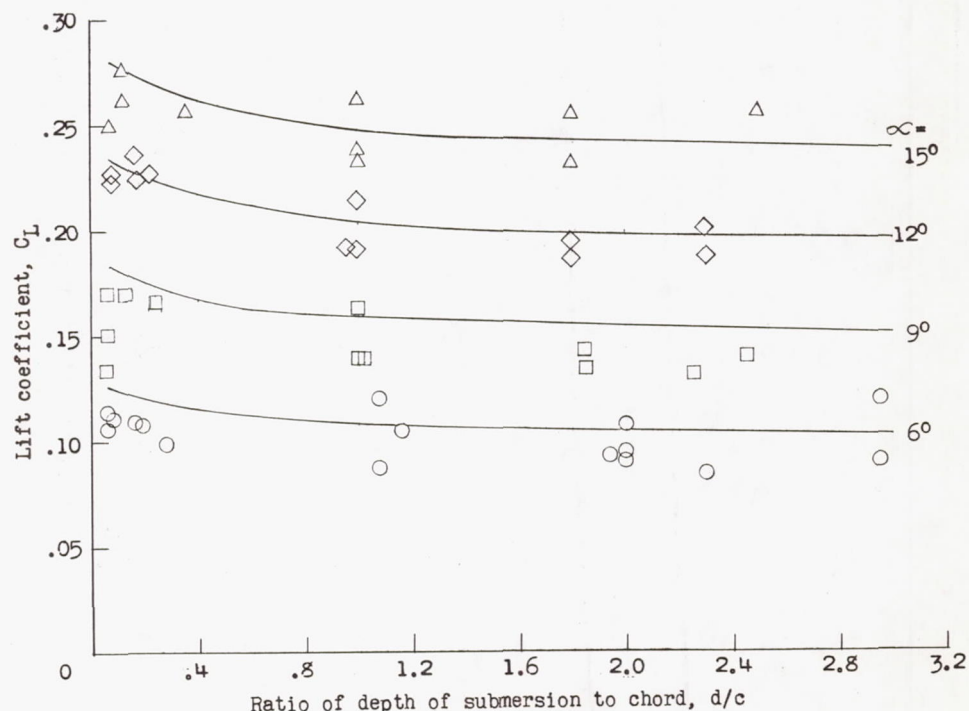


Figure 28.- Comparison of theoretical and experimental lift coefficients for flat lifting surface as affected by depth of submersion. $\alpha = 16^\circ$ and 20° ; aspect ratio of 1.

(a) Cambered section, $\alpha = 9^\circ$.

(b) Flat plate.

Figure 29.- Comparison of present theory with experimental data of Fuller obtained on hydrofoils having an aspect ratio of 2.

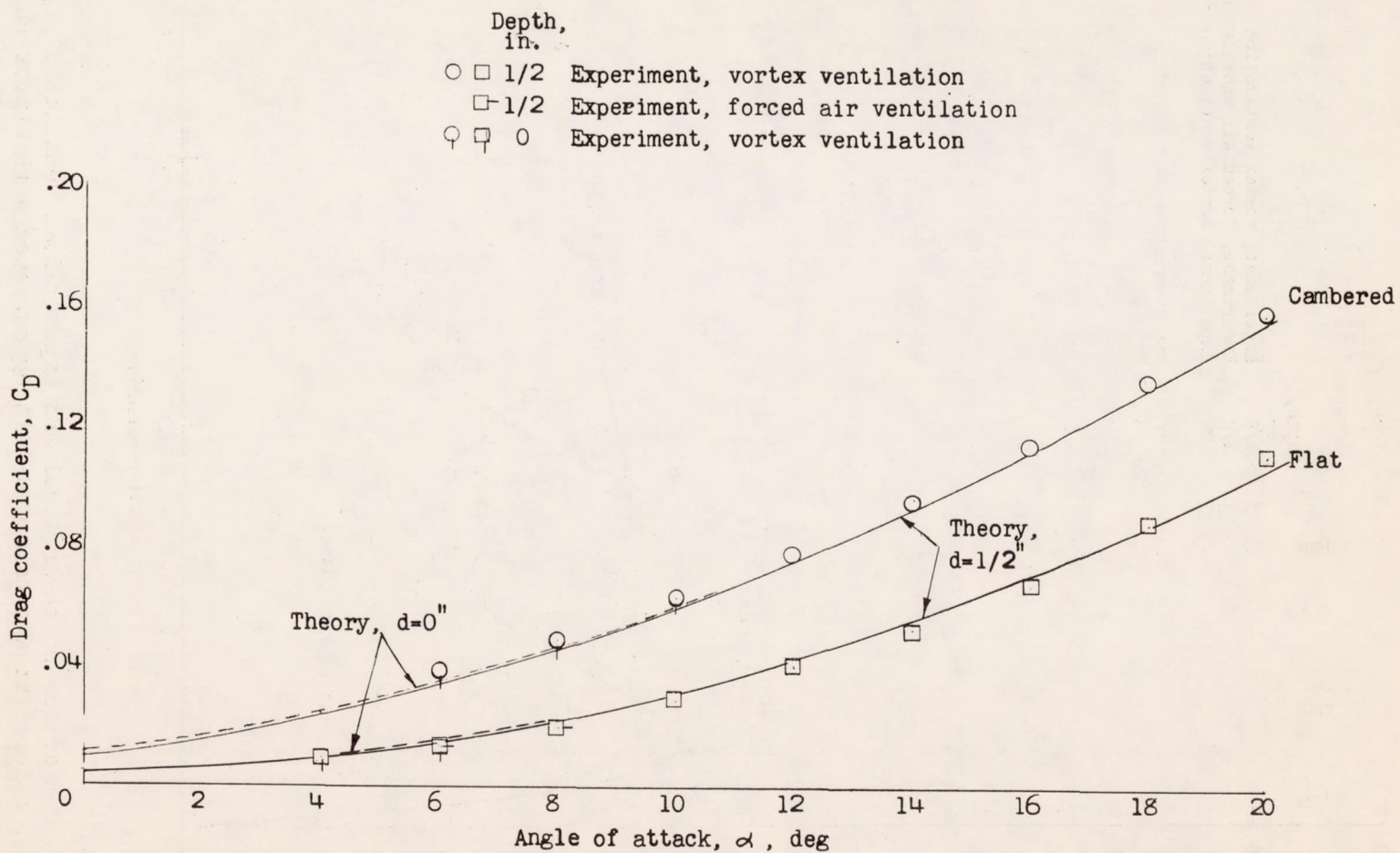


Figure 30.- Comparison of theoretical and experimental ventilated drag coefficients for flat and cambered lifting surfaces with aspect ratio of 1.

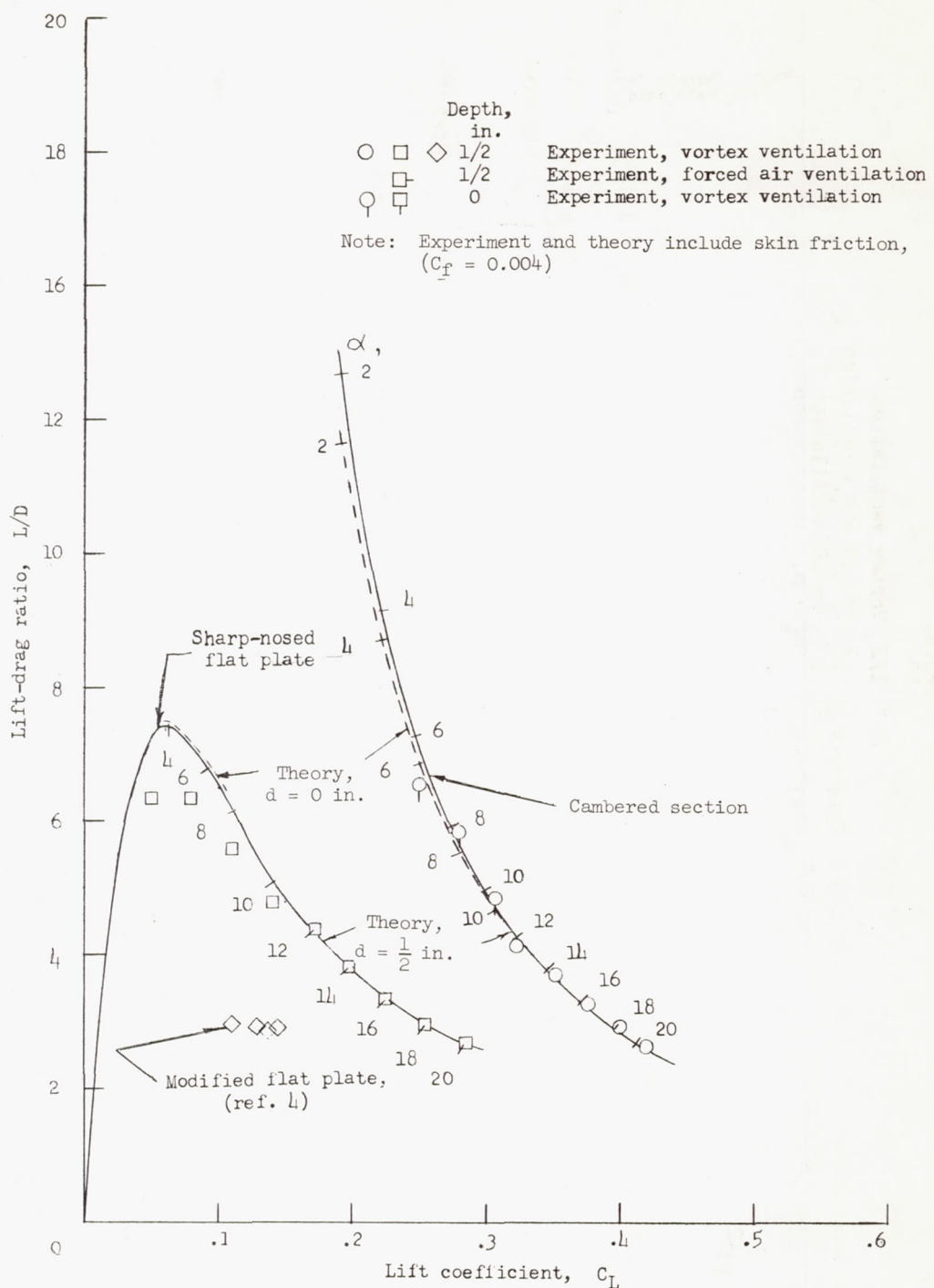


Figure 31.- Comparison of theoretical and experimental ventilated lift-drag ratios for flat and cambered lifting surfaces with aspect ratio of 1.

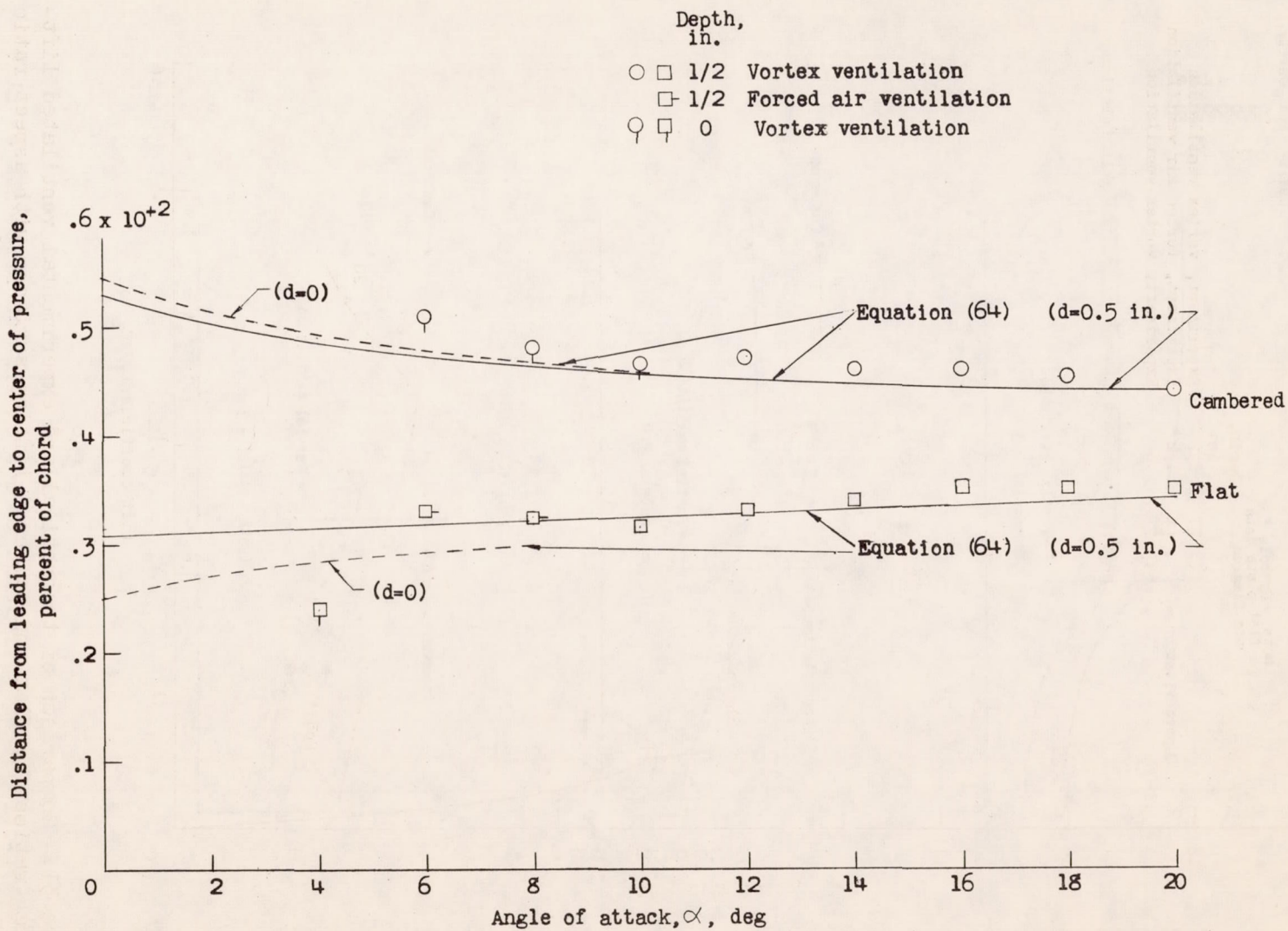


Figure 32.- Location of center of pressure of flat and cambered lifting surfaces with aspect ratio of 1.

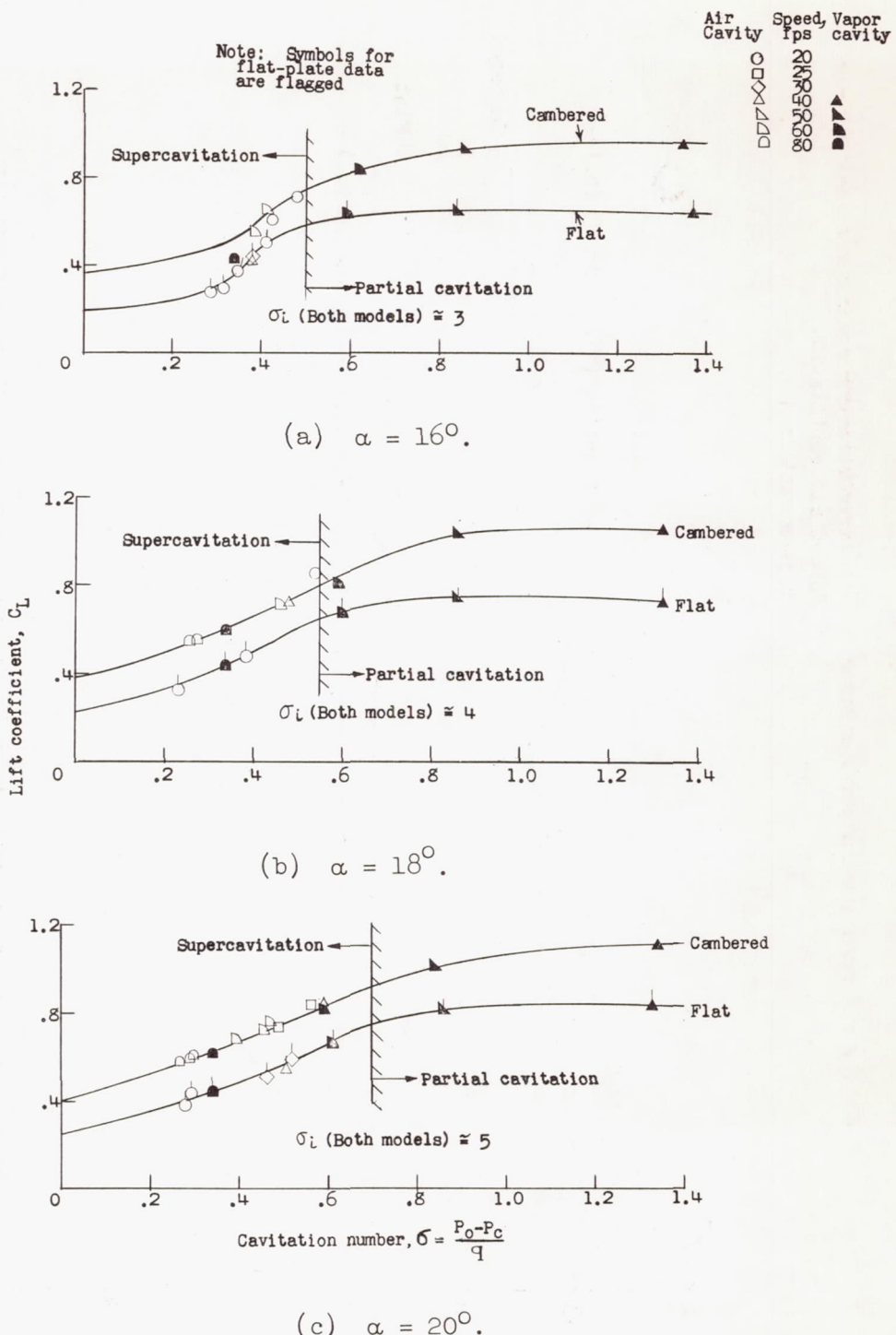


Figure 33.- Effect of cavitation number on lift coefficients of flat and cambered lifting surfaces. Depth of submersion is 6 inches; aspect ratio of 1.

C

NACA RM L57I16

CONFIDENTIAL

93



Air, $\sigma = 0.39$, $V = 20$ fps



Vapor, $\sigma = 0.33$, $V = 80$ fps

(a) Flat plate.

L-57-2743

Figure 34.- Comparison of air- and vapor-filled cavities for depth of submersion of 6 inches and α of 20° .

CONFIDENTIAL



Air, $\sigma = 0.48$, $V = 20$ fps



Vapor, $\sigma = 0.33$, $V = 80$ fps

(b) Cambered section.

L-57-2744

Figure 34.- Concluded.